



Juliana da Silva Padilha

**Development of analytical methods based on the
photoluminescence of an Eu(III) β -diketonate complex,
new silver-modified nitrogen-doped graphene quantum
dots and a benzothiadiazole derivative**

Tese de Doutorado

Thesis presented to the Programa de Pós-Graduação em Química of PUC-Rio in partial fulfillment of the requirements for the degree of Doutor em Química.

Advisor: Ricardo Queiroz Aucélio
Co-Advisor: Anna De Falco

Rio de Janeiro

May 2022



Juliana da Silva Padilha

**Development of analytical methods based on the
photoluminescence of an Eu(III) β -diketonate complex,
new silver-modified nitrogen-doped graphene quantum
dots and a benzothiadiazole derivative**

Thesis presented to the Programa de Pós-graduação em
Química of PUC-Rio in partial fulfillment of the
requirements for the degree of Doutor em Química.
Approved by the Examination Committee:

Ricardo Queiroz Aucélio

Advisor
Departamento de Química - PUC-Rio

Arnaldo Alves Cardoso

UNESP

Maria Luiza Bragança Tristão

Pesquisadora de Projeto P&D – PUC-Rio

Andrea Rosane da Silva

CEFET/RJ – Campus Valença

Jones Limberger

Departamento de Química - PUC-Rio

Rio de Janeiro, May 27th 2022

All rights reserved

Juliana da Silva Padilha

Doctorate candidate in Chemistry of the Pontifical Catholic University of Rio de Janeiro (PUC-Rio). She holds a Master's degree in Chemistry from the Pontifical Catholic University of Rio de Janeiro (2017) and a degree in Industrial Chemistry from the Rural Federal University of Rio de Janeiro (2014). She has experience in the fields of Inorganic Chemistry and Instrumental Analytical Chemistry.

Bibliographic data

Padilha, Juliana da Silva

Development of analytical methods based on the photoluminescence of an Eu(III) β -diketonate complex, new silver-modified nitrogen-doped graphene quantum dots and a benzothiadiazole derivative / Juliana da Silva Padilha ; advisor: Ricardo Queiroz Aucélio ; co-advisor: Anna De Falco. – 2022.

177 f. : il. color. ; 30 cm

Tese (doutorado)–Pontifícia Universidade Católica do Rio de Janeiro, Departamento de Química, 2022.

Inclui bibliografia

1. Química – Teses. 2. Sondas fotoluminescentes. 3. Complexo de európio. 4. Pontos quânticos modificados. 5. Derivado de benzotiadiazola. 6. Sensores de temperatura. I. Aucélio, Ricardo Queiroz. II. Falco, Anna De. III. Pontifícia Universidade Católica do Rio de Janeiro. Departamento de Química. IV. Título.

CDD: 540

To my parents, Jair and Tânia,
For all the support and encouragement.

Acknowledgements

To God, for always being faithful to His promises and for giving me the strength and courage to achieve this goal.

To my family, my parents Jair and Tânia, my brothers Thiago and Diego and my partner João Víctor, for all the unconditional love and support and for never measuring efforts to make my dreams come true. Thank you for everything.

To my advisor, Dr. Ricardo Queiroz Aucélio, for the valuable lessons, guidance, motivation, trust and friendship. I will be forever grateful for everything you have done for me. Thanks also to my co-advisor, Anna De Falco, for all the help and friendship. Your friendship was a very pleasant surprise.

To the examining members, for their availability and for accepting the invitation.

To the LEEA group for all the help and moments of fun. The friendship in our Lab group made everything more beautiful and lighter. Also, I would like to thank my good friend Marcelo for always being there for me. Thank you for everything!

To the Chemistry Department of PUC-Rio and all the professors for the support and lessons.

To PUC-Rio and the Brazilian Agencies CNPq, CAPES and FAPERJ for grants and doctoral scholarship.

To all the people who, directly or indirectly, contributed to the accomplishment of this work but were not mentioned before.

This study was financed in part by the Coordenação de Aperfeiçoamento de Pessoal de Nível Superior - Brasil (CAPES) - Finance Code 001.

Abstract

Padilha, Juliana da Silva; Aucélio, Ricardo Queiroz (Advisor); Falco, Anna De (Co-advisor). **Development of analytical methods based on the photoluminescence of an Eu(III) β -diketonate complex, new silver-modified nitrogen-doped graphene quantum dots and a benzothiadiazole derivative.** Rio de Janeiro, 2022. 177p. Tese de Doutorado - Departamento de Química, Pontifícia Universidade Católica do Rio de Janeiro.

The present work aims the development of photoluminescence based analytical methods for the determination of toxic analytes (methylmercury and formaldehyde) and for temperature sensing. The probes and methods proposed allow, under adjusted conditions, selective determinations with competitive limits of detection and simple procedures when compared to those methods reported in literature. In terms of temperature sensing, probes performed with sensitivity and prompt reversibility in solutions, also showing good potential when immobilized in polymeric films. In the first part of this work the preparation, characterization and studies of spectroscopic properties of a trivalent rare earth β -diketonate complex $[\text{Eu}(\text{tta})_4](\text{Et}_3\text{NH}^+)$ is presented aiming to produce a method to enable the determination of methylmercury in produced water. The structural characteristic of the complex along with a liquid-liquid extraction procedure enable high selectivity towards the analyte and limit of detection (LOD) of $0.059 \mu\text{g L}^{-1}$. The second part of this work aimed to develop new nitrogen-doped silver modified graphene quantum dots (N-GQDs-Ag) that, after structural and optical characterization, was used as a probe to determine formaldehyde contamination in milk. Selectivity was achieved by probing formaldehyde in the vapor phase as the N-GQDs-Ag dispersion was used in a headspace single-drop microextraction procedure. Limit of detection in milk was $5.5 \times 10^{-3} \text{ g L}^{-1}$. Finally, $[\text{Eu}(\text{tta})_4](\text{Et}_3\text{NH}^+)$, N-GQDs-Ag and the recently reported benzothiadiazole derivative 4-(4-methoxyphenoxy)-7-styrylbenzo[c][1,2,5]thiadiazole (LASOC 460) were evaluated as probes for the sensing of temperature variation with better performance for the N-GQDs-Ag.

Keywords

Photoluminescent probes; europium complex; modified quantum dots; benzothiadiazole derivative; methylmercury; formaldehyde; temperature sensing.

Resumo

Padilha, Juliana da Silva; Aucélio, Ricardo Queiroz; Falco, Anna De. **Desenvolvimento de métodos analíticos baseados na fotoluminescência de um complexo β -dicetonato de Eu(III), de novos pontos quânticos de grafeno dopados com nitrogênio e modificados com prata e de um derivado de benzotiadiazola.** Rio de Janeiro, 2022. 177p. Tese de Doutorado - Departamento de Química, Pontifícia Universidade Católica do Rio de Janeiro.

O presente trabalho visa o desenvolvimento de métodos analíticos baseados em fotoluminescência para a determinação de analitos tóxicos (metilmercúrio e formaldeído) e para sensoriamento de temperatura. As sondas e métodos propostos permitem, sob condições ajustadas, determinações seletivas com limites de detecção competitivos e procedimentos simples quando comparados aos métodos reportados na literatura. Em termos de sensoriamento de temperatura, as sondas foram utilizadas com sensibilidade e rápida reversibilidade em solução, também apresentando bom potencial quando imobilizadas em filmes poliméricos. Na primeira parte deste trabalho é apresentada a preparação, caracterização e estudos das propriedades espectroscópicas de um complexo trivalente de β -dicetonato de terras raras $[\text{Eu}(\text{tta})_4](\text{Et}_3\text{NH}^+)$ com o objetivo de produzir um método que permita a determinação de metilmercúrio em água de produção. A característica estrutural do complexo juntamente com um procedimento de extração líquido-líquido permite alta seletividade em relação ao analito e limite de detecção (LOD) de $0,059 \mu\text{g L}^{-1}$. A segunda parte deste trabalho teve como objetivo desenvolver novos pontos quânticos de grafeno modificado com prata dopado com nitrogênio (N-GQDs-Ag) que, após caracterização estrutural e óptica, foram usados como sonda para determinar a contaminação por formaldeído em leite. A seletividade foi alcançada pela sondagem de formaldeído na fase de vapor, uma vez que a dispersão de N-GQDs-Ag foi usada em um procedimento de microextração de gota pendente no headspace. O limite de detecção no leite foi $5,5 \times 10^{-3} \text{ g L}^{-1}$. Finalmente, $[\text{Eu}(\text{tta})_4](\text{Et}_3\text{NH}^+)$, N-GQDs-Ag e o derivado de benzotiadiazola recentemente reportado 4-(4-metoxifenoxi)-7-estirilbenzo[c][1,2,5]tiadiazola (LASOC 460)

foram avaliados como sondas para o sensoriamento de variação de temperatura com melhor desempenho para o N-GQDs-Ag.

Palavras-chave

Sondas fotoluminescentes; complexo de európio; pontos quânticos modificados; derivado de benzotiadiazola; metilmercúrio; formaldeído; sensor de temperatura.

Table of contents

1 Introduction e Objectives	23
1.1. Contextualization of work	23
1.2. Thesis structure	24
1.3. Objectives	25
1.3.1. General objective	25
1.3.2. Specific objectives	25
2 Theoretical Fundaments	27
2.1. Chemical optical sensors	27
2.2. Luminescence	28
2.2.1. Photoluminescence of molecules	29
2.2.2. Photoluminescence of rare earth complexes	31
2.2.3. Photoluminescence of nanomaterials	32
2.3. Characteristics and properties of the luminophores used as probes in this work	36
2.3.1. Eu ³⁺ ions and their use as photoluminescent probes	36
2.3.2. Graphene quantum dots and their use as photoluminescent probes	38
2.3.3. Benzothiadiazoles and their use as fluorescent probes	42
2.4. Properties and characteristics of analytes and physical parameters evaluated in this work	45
2.4.1. Mercury	45
2.4.2. Formaldehyde	52
2.4.3. Temperature	57
3 Experimental	64
3.1. Instruments and apparatuses	64
3.2. Reagents and materials	66
3.3. Procedures concerning the lanthanide complex	67
3.3.1. Preliminary studies for the choice of the lanthanide complex	67

3.3.2. Synthesis of $[\text{Eu}(\text{tta})_4](\text{Et}_3\text{NH}^+)$ by a new synthetic route	68
3.3.3. Characterization of $[\text{Eu}(\text{tta})_4](\text{Et}_3\text{NH}^+)$	68
3.3.4. Solubility tests of $[\text{Eu}(\text{tta})_4](\text{Et}_3\text{NH}^+)$	69
3.3.5. Photoluminescence stability test of $[\text{Eu}(\text{tta})_4](\text{Et}_3\text{NH}^+)$ in solution or after dried on a solid substrate	69
3.3.6. Oxygen (O_2) influence test	70
3.3.7. Choice of acetone/water ratio	70
3.3.8. Preparation of working solutions	71
3.3.9. Tests of pH influence	71
3.3.10. Tests of temperature influence	72
3.3.11. Tests of mercury influence	72
3.3.12. Tests of different metal ions influence	72
3.3.13. Extraction and preconcentration of CH_3Hg^+	73
3.3.14. Tests with preconcentrated CH_3Hg^+ samples in water and PW	74
3.3.15. Photoluminescent measurements of $[\text{Eu}(\text{tta})_4](\text{Et}_3\text{NH}^+)$	74
3.3.16. Quantitative determination of mercury in water and in PW samples by Multipass-CV-AAS	74
3.4. Procedures concerning N-doped graphene quantum dots	75
3.4.1. Preliminary studies for the production of N-GQDs and the interaction with formaldehyde	75
3.4.2. Characterization procedures for N-GQDs-Ag	78
3.4.3. Preparation of standard solutions, sample solutions and working solutions	79
3.4.4. pH influence	80
3.4.5. Study of temperature influence	80
3.4.6. Influence of UV radiation	80
3.4.7. Analysis of formaldehyde using headspace single drop microextraction (HS-SDME)	81
3.4.8. Tests of hydrogen peroxide (H_2O_2) interference	81
3.4.9. Photoluminescence measurements	82
3.4.10. Comparative colorimetric method for the determination of formaldehyde in milk samples	82
3.4.11. Comparative chromatographic method for the determination of formaldehyde in milk samples	83

3.5. Procedures concerning temperature sensing	84
3.5.1. Sensing of temperature using luminophore solutions	84
3.5.2. Sensing of temperature using luminophore polymeric matrices	84
3.5.3. Photoluminescent measurements	85
3.5.4. Toxicity tests of N-GQDs-Ag	85
4 Characterization of luminophores	88
4.1. Characterization of $[\text{Eu}(\text{tta})_4](\text{Et}_3\text{NH}^+)$	88
4.1.1. Morphological analysis of the complex	88
4.1.2. Stoichiometric characterization	89
4.1.3. Analysis by absorption spectroscopy in the infrared region (FTIR)	90
4.1.4. Thermogravimetric analysis (TGA/DTG)	91
4.1.5. Optical properties of $[\text{Eu}(\text{tta})_4](\text{Et}_3\text{NH}^+)$ in solid state	92
4.1.6. Optical properties of $[\text{Eu}(\text{tta})_4](\text{Et}_3\text{NH}^+)$ in solution	93
4.2. Characterization of N-GQDs-Ag	95
4.2.1. Morphological and structural characterization of N-GQDs-Ag	95
4.2.2. Total carbon analysis	96
4.2.3. Dynamic light scattering and ζ -potential analysis	96
4.2.4. Scanning transmission electron microscopy analysis	99
4.2.5. X-ray photoelectron spectroscopy analysis	99
4.2.6. Absorption spectroscopy in the infrared region analysis	101
4.2.7. Optical properties	101
4.3. Characterization of LASOC 460	103
4.3.1. Optical properties	103
5 Use of selective quenching of a photoluminescent probe based on a Eu(III) β -diketonate complex for determination of methylmercury in produced water after liquid-liquid extraction	106
5.1. Analytical method using Eu(III) to determine methylmercury	106
5.2. Results and discussion	107
5.2.1. Preliminary studies for the choice of the lanthanide complex	107
5.2.2. Solubility test of $[\text{Eu}(\text{tta})_4](\text{Et}_3\text{NH}^+)$	107
5.2.3. Stability test of $[\text{Eu}(\text{tta})_4](\text{Et}_3\text{NH}^+)$ in solution	108
5.2.4. Stability test of $[\text{Eu}(\text{tta})_4](\text{Et}_3\text{NH}^+)$ in solid substrate	109

5.2.5. Influence of atmospheric oxygen (O ₂) on the solid complex placed in substrate	110
5.2.6. Choice of analyte	111
5.2.7. Choice of acetone/water ratio	112
5.2.8. Study of pH influence	113
5.2.9. Tests of temperature influence	114
5.2.10. Probe sensitivity towards mercurial species	115
5.2.11. Tests of different metal ions influence	119
5.2.12. Application in preconcentrated CH ₃ Hg ⁺ in water and in PW samples	121
5.2.13. Interaction of CH ₃ Hg ⁺ with probe	Erro! Indicador não definido. 122
5.3. Partial conclusions	124
6 Photoluminometric determination of formaldehyde in milk using microextraction on a single-drop of aqueous dispersion of silver-modified nitrogen doped graphene quantum dots	125
6.1. Analytical method to determine formaldehyde in milk	125
6.2. Results and discussion	126
6.2.1. Preliminary results concerning the production of GQDs and their interaction with formaldehyde	126
6.2.2. Factors influencing photoluminescence	128
6.2.3. N-GQDs photoluminescence quenching induced by formaldehyde	130
6.3. Partial conclusion	141
7 Preliminary evaluation of [Eu(tta) ₄](Et ₃ NH ⁺), N-GQDs-Ag and LASOC 460 as probes for temperature sensing	142
7.1. Analytical method for temperature sensing	142
7.2. Evaluation of the [Eu(tta) ₄](Et ₃ NH ⁺) complex as a temperature probe	143
7.3. Evaluation of the organic dye LASOC 460 as a temperature probe	146
7.4. Evaluation of the N-GQDs-Ag as a temperature probe	149
7.5. Toxicity tests of N-GQDs-Ag	152

7.6. Partial Conclusion	153
8 Conclusion	155
9 References	158
10 Attachments	177
10.1. Published papers	177

List of figures

Figure 2.1 – Modified Jablonski diagram adapted from [18].	29
Figure 2.2 - Structure of 2,1,3-benzothiadiazole.	42
Figure 2.3 - Synthesis of 4,7-dibromo-2,1,3-benzothiadiazole.	42
Figure 3.1 - Photochemical reactor built in LEEA-PUC-Rio.	66
Figure 4.1 - Image of $[\text{Eu}(\text{tta})_4](\text{Et}_3\text{NH}^+)$ complex under ambient light and under ultraviolet radiation.	88
Figure 4.2 - FTIR spectra of Htta and $[\text{Eu}(\text{tta})_4](\text{Et}_3\text{NH}^+)$.	90
Figure 4.3 - TGA and DTG curves of $[\text{Eu}(\text{tta})_4](\text{Et}_3\text{NH}^+)$.	91
Figure 4.4 - Proposed structure of $[\text{Eu}(\text{tta})_4](\text{Et}_3\text{NH}^+)$.	92
Figure 4.5 – Emission spectrum of $[\text{Eu}(\text{tta})_4](\text{Et}_3\text{NH}^+)$ in solid state under excitation at 393 nm.	93
Figure 4.6 – (A) Absorption spectrum and (B) calibration curve of $[\text{Eu}(\text{tta})_4](\text{Et}_3\text{NH}^+)$.	94
Figure 4.7 - Excitation (monitored at 616 nm) and emission (Ex = 343 nm) spectra of $[\text{Eu}(\text{tta})_4](\text{Et}_3\text{NH}^+)$ solution.	94
Figure 4.8 - N-GQDs-Ag dispersion at (A) day 1, (B) day 15, (C) day 30, (D) day 90 and (E) under UV radiation.	96
Figure 4.9 - ζ -potential of N-GQDs-Ag in function of pH 24 h after production (A) without exposure to UV-radiation and (B) under exposure to UV-radiation for 15 min.	98
Figure 4.10 - Size distribution of N-GQDs-Ag in aqueous dispersion in function of pH obtained by DLS (a) 24 h after preparation, (b) 24 h after preparation and 15 minutes exposure to UV and (c) 120 h after preparation.	98
Figure 4.11 - STEM image of size distribution of N-GQDs-Ag.	99
Figure 4.12 - (A) XPS general survey scan of N-GQDs-Ag,	

(B) deconvoluted C 1s peaks and (C) deconvoluted N 1s peaks.	100
Figure 4.13 - FT-IR spectra of N-GQDs-Ag.	101
Figure 4.14 - Absorption spectrum of N-GQDs-Ag.	102
Figure 4.15 - N-GQDs-Ag (a) excitation and (b) emission spectra.	103
Figure 4.16 – Structure of 4-(4-methoxyphenoxy)-7-styrylbenzo[c][1,2,5]thiadiazole (LASOC 460).	103
Figure 4.17 – (A) LASOC 460 (a) excitation and (b) emission spectra in the non-aggregated form and (B) LASOC 460 (a) excitation and (b) emission spectra in the aggregated form.	104
Figure 4.18 - Absorption spectrum of LASOC 460 in (A) non-aggregated form and (B) aggregated form.	105
Figure 5.1 – [Eu(tta) ₄](Et ₃ NH ⁺) emission intensity variation (A) under exposure to ambient light, (B) protected from light and (C) under exposure to UV radiation.	109
Figure 5.2 – (A) Photoluminescence emission spectra of [Eu(tta) ₄](Et ₃ NH ⁺) on filter paper substrate over a) 0, b) 5, c) 10, d) 15, e) 20, f) 30, g) 45 and h) 60 min and (B) variation of intensity over time (peak height).	110
Figure 5.3 – (A) Photoluminescence emission spectra of [Eu(tta) ₄](Et ₃ NH ⁺) on filter paper substrate protected with a quartz window over a) 0, b) 5, c) 10, d) 15, e) 20, f) 30, g) 45 and h) 60 min. and (B) variation of the emission over time (peak height).	111
Figure 5.4 - [Eu(tta) ₄](Et ₃ NH ⁺) photoluminescent intensity changes at different pHs.	114
Figure 5.5 – (A) [Eu(tta) ₄](Et ₃ NH ⁺) photoluminescent intensity changes at different temperatures and (B) linear relationship between photoluminescent intensity and temperature.	114
Figure 5.6 – (A) Emission spectra for the photoluminescence responses of [Eu(tta) ₄](Et ₃ NH ⁺) for concentrations of Hg ²⁺ at	

- a) 0, b) 40, c) 80, d) 120, e) 160 and f) 200 $\mu\text{g L}^{-1}$, (B) variation of emission intensities from 0 to 48 h for concentrations of Hg^{2+} at 40 b) 80, c) 120, d) 160 and e) 200 $\mu\text{g L}^{-1}$ and (C) relationship between normalized photoluminescent intensity and Hg^{2+} concentration. 116
- Figure 5.7 – (A) emission spectra with the photoluminescence responses of $[\text{Eu}(\text{tta})_4](\text{Et}_3\text{NH}^+)$ for concentrations of CH_3Hg^+ at a) 0, b) 40, c) 80, d) 120, e) 160 and f) 200 $\mu\text{g L}^{-1}$ and B) graph of the linear relationship between normalized photoluminescence and CH_3Hg^+ concentration. 117
- Figure 5.8 – (A) emission spectra with the photoluminescent responses of $[\text{Eu}(\text{tta})_4](\text{Et}_3\text{NH}^+)$ for concentrations of CH_3Hg^+ at 0, b) 0.2, c) 0.4, d) 0.6, e) 0.8, f) 1.0, g) 1.5 and h) 2.0 $\mu\text{g L}^{-1}$ and (B) graph of the linear relationship between normalized photoluminescent intensity and CH_3Hg^+ concentration. 119
- Figure 5.9 - Column graph of photoluminescent variation in the presence of different metal ions at A) 200 $\mu\text{g L}^{-1}$ and B) 1 mg L^{-1} ; error bars are the standard deviation of three replicates. 120
- Figure 5.10 - Ionic strength of the different salts in the probe solution. 121
- Figure 6.1 – Photoluminescent quenching of N-GQDs probe in the presence of formaldehyde solution at different concentrations over (a) 0, (b) 1, (c) 3 and (d) 24 h. 126
- Figure 6.2 – Photoluminescent quenching of N-GQDs probe in the presence of formaldehyde vapor when tests were made (A) in a sealed Petri dish with concentrations at (a) 0, (b) 12, (c) 24, (d) 47.5, (e) 95, (f) 190 and (g) 385 g L^{-1} ; (B) using the HS-SDME with concentrations at (a) 0, (b) 1.5, (c) 3.0 and (d) 6.0 g L^{-1} . 127
- Figure 6.3 - N-GQDs-Ag emission intensity changes at different temperatures. 129
- Figure 6.4 - N-GQDs-Ag emission intensity changes at

different pH. 130

Figure 6.5 - N-GQDs-Ag emission intensity changes at different times after contact with: (A) formaldehyde solution at concentration of $1.5 \times 10^{-4} \text{ g L}^{-1}$ after (a) 1 minute, (b) 10 minutes, (c) 20 minutes and (d) 30 minutes and (B) formaldehyde vapor from a 1.5 g L^{-1} solution after (a) 1 minute, (b) 10 minutes, (c) 20 minutes and (d) 30 minutes. 132

Figure 6.6 - Effects of temperature in N-GQDs-Ag photoluminescence intensity in the presence of formaldehyde at different concentrations in (A) solution at (a) 25, (b) 27.5, (c) 30 and (d) 32.5 °C; and (B) vapor at (a) 25, (b) 30, (c) 35 and (d) 40 °C. 134

Figure 6.7 - (A) N-GQDs-Ag response towards increasing concentrations of formaldehyde vapor: (a) 0, (b) 1.0×10^{-2} , (c) 2.5×10^{-2} , (d) 5.0×10^{-2} , (e) 7.5×10^{-2} and (f) $1.0 \times 10^{-1} \text{ g L}^{-1}$. (B) Linear relationship between normalized photoluminescent intensity and formaldehyde concentration. 135

Figure 6.8 - Color variation of chromotropic acid solution after contact with the distilled solutions of milk samples fortified with formaldehyde at concentrations of (a) 0, (b) 1.0×10^{-3} , (c) 1.0×10^{-2} , (d) 1.0×10^{-1} and (e) 1.0 g L^{-1} . 139

Figure 7.1 - (A) Fluorescence spectra of $[\text{Eu}(\text{tta})_4](\text{Et}_3\text{NH}^+)$ at the temperatures of (a) 20, (b) 22, (c) 24 and (d) 26, (e) 28 and (f) 30 °C. (B) Linear relationship between fluorescence intensity of $[\text{Eu}(\text{tta})_4](\text{Et}_3\text{NH}^+)$ and temperature. 143

Figure 7.2 – Red emission of the PCL-Eu(III) system under UV. 144

Figure 7.3 – (A) Fluorescence spectra of PCL-Eu(III) at the temperatures of (a) 25, (b) 30, (c) 35 and (d) 40 °C. (B) Linear relationship between fluorescence intensity of PCL-Eu(III) and temperature. 145

Figure 7.4 - Temperature optical sensing of PCL-EU(III)

in (A) three cycles of temperature from 25 to 40 °C and (B) in seven cycles of temperature from 25 to 30 °C.	145
Figure 7.5 – (A) Fluorescence spectra of LASOC 460, in tert-butyl alcohol, at different temperatures: (a) 25, (b) 30, (c) 35 and (d) 40 °C. (B) Linear relationship between fluorescence intensity of LASOC 460 in function of temperature.	147
Figure 7.6 – Green-yellow emission of the PMMA-LASOC 460 system under UV.	147
Figure 7.7 - Fluorescence spectra of PMMA-LASOC 460 at different temperatures: (a) 25, (b) 30, and (c) 40 °C.	148
Figure 7.8 - Temperature sensing of PMMA-LASOC 460 in seven cycles of temperature from 25 °C to 40 °C.	149
Figure 7.9 – (A) Photoluminescence spectra of N-GQDs-Ag aqueous dispersion at different temperatures: (a) 25, (b) 30, (c) 40 and (d) 50 °C. (B) Temperature sensing stability of N-GQDs-Ag aqueous dispersion in seven cycles of temperature switching at 25 to 50 °C.	150
Figure 7.10 – Blue emission from the PVA-N-GQDs-Ag system under UV.	150
Figure 7.11 – (A) Photoluminescence spectra of PVA-N-GQDs-Ag at different temperatures of (a) 25, (b) 30, (c) 35 and (d) 40 °C. (B) Linear relationship between photoluminescent intensity of PVA-N-GQDs-Ag and temperature.	151
Figure 7.12 - Temperature sensing stability of PVA-N-GQDs-Ag in seven cycles of temperature switching within 25 °C to 40 °C range.	152
Figure 7.13 – Toxicity of (A) N-GQDs-Ag and (B) N-GQDs to <i>S. cerevisiae</i> cells.	153

List of tables

Table 3.1 – Available lanthanide complexes.	67
Table 4.1 - CHN result for Eu^{3+} complex with tta^- ligand.	89
Table 4.2 – Vibrational frequencies characteristic of Htta and $[\text{Eu}(\text{tta})_4](\text{Et}_3\text{NH}^+)$.	91
Table 4.3 – Thermogravimetric data for the $[\text{Eu}(\text{tta})_4](\text{Et}_3\text{NH}^+)$ complex.	92
Table 5.1 - Experimental conditions for mercury determination.	115
Table 5.2 - Analysis results (CH_3Hg^+ recoveries) from fortified control water and PW samples using the proposed method (photoluminescent probe) and CV-AAS after extraction and pre-concentration.	123
Table 6.1 - Experimental conditions for formaldehyde determination.	131
Table 6.2 - Recovery results for formaldehyde in different types of milk using the N-GQDs-Ag photoluminescent probe.	140

List of Abbreviations

- AIEE – aggregation-induced enhanced emission
- BTD – benzothiadiazole
- CQDs – carbon quantum dots
- CV-AAS – cold vapor atomic absorption spectrometry
- DLS – dynamic light scattering
- DNPH – 2,4-dinitrophenylhydrazine
- FTIR – fourier transform infrared spectroscopy
- GQDs – graphene quantum dots
- HPLC – high performance liquid chromatography
- HS-SDME – headspace single-drop microextraction
- LOD – limit of detection
- LOQ – limit of quantification
- N-GQDs – nitrogen doped graphene quantum dots
- N-GQDs-Ag – nitrogen doped graphene quantum dots modified with silver
- PCL – polycaprolactone
- PMMA – polymethyl methacrylate
- PVA – polyvinyl alcohol
- PW – produced water
- QDs – quantum dots
- RSD – relative standard deviation
- STEM – scanning transmission electron microscopy
- UV-Vis – ultraviolet visible
- XPS – X-ray photoelectron spectroscopy
- YPD – yeast extract-peptone-dextrose

It's the time spent on your rose that makes your rose so important.

Antoine de Saint-Exupéry, *The Little Prince*

1 Introduction e Objectives

1.1. Contextualization of work

Peculiar properties of optically active materials have been explored in the development of analytical methods for the determination of various types of analytes in the most varied kind of samples. In the case of luminophores, the availability of different types of luminescent chemical species makes them very attractive and widely applied as luminescent probes. Among them, it is included lanthanide complexes, quantum dots, and organic dyes.

Among the ions of lanthanide elements, the ones that receive the most attention in terms of optical properties are Eu^{3+} and Tb^{3+} due to their intense and almost monochromatic emissions, respectively, in the red and green part of the visible spectrum. These atomic-like emissions are the result of an effective shielding that the $5s^2$ and $5p^6$ filled orbitals exerted upon electrons of incomplete 4f orbitals from where transitions result in narrow and well-defined spectral lines with long lifetime emissions.

Graphene quantum dots (GQDs) produce photoluminescence that can be adjusted by modifying their sizes, functionalizing them and/or modifying their immediate surroundings. The functionalization of the surface/edges of the GQDs can improve photoluminescence and provide some selectivity in terms of interaction with the target chemical species. In addition, these nanomaterials tend to be less toxic and more resilient to photo-bleaching when compared to inorganic semiconductor quantum dots (QDs). They also are easily stabilized in colloidal aqueous dispersions.

Derivatives of 2,1,3-benzothiadiazoles (BTDs) are a class of fluorophores that is very attractive as these can be used in various applications in the area of luminescent technology. Overall, the net result of a π extension at positions 4- and/or 7- of the BTD nucleus, accompanied by π -conjugated system, greatly favors fluorescence and photo-stability. Considering the possibility of selecting the

substituent groups in the BTD ring, it is possible to predict photophysical properties of the designed structures as the influence of these groups will be reflected on the overall optical behavior of BTD derivatives.

The development of analytical methods based on probes that present inherent luminescence can provide analytical detection advantages in terms of figures of merit, metrological performance, also simplifying analytical protocols, and improving safety as very low quantities of probe may be enough to produce analytical signal or the measurable variation of analytical signal. Thus, this work focuses on the development of photoluminescent analytical probes using coordination compounds containing lanthanide ions, benzothiadiazoles and graphene quantum dots.

1.2. Thesis structure

This thesis is structured into eight chapters. In Chapter 2, a general definition of chemical sensors is presented, as well as a brief explanation of the luminescence processes that occur in these types of sensors. It also presents the properties and applications of lanthanide coordination compounds, graphene quantum dots and organic compounds of the benzothiadiazole class as luminescent probes. Then, a brief presentation on the most commonly used thermometers, optical temperature sensors, and photoluminescent chemical compounds currently used as temperature probes was made. In addition, a brief introduction on the analytes (mercury/methylmercury and formaldehyde) was presented along with a concise literature review concerning the analytical methods for the determination of these analytes.

Chapter 3 contains information on instruments and materials used, the synthesis carried out and the general procedures involved in characterizations as well as in the proposed analytical methods.

In Chapter 4 are presented the results of studies involving the synthesis and characterization of the europium coordination compound. It also presents the results of studies on the preparation and characterization of the nitrogen doped graphene quantum dots modified with silver and the optical characterization of the benzothiadiazole derivative LASOC 460.

In Chapter 5 are presented the results of the studies to employ the europium coordination compound $[\text{Eu}(\text{tta})_4](\text{Et}_3\text{NH}^+)$ as a luminescent probe for the determination of methylmercury in produced water samples after liquid-liquid extraction.

In Chapter 6 are presented the studies concerning the development of the analytical method that rely on the use of the graphene quantum dots doped with nitrogen and modified with silver (N-GQDs-Ag) dispersions as probe, employing headspace single drop microextraction to allow a simple way to determine formaldehyde in milk samples.

Chapter 7 is dedicated to the studies concerning the use of three different luminophores ($[\text{Eu}(\text{tta})_4](\text{Et}_3\text{NH}^+)$, N-GQDs-Ag and one BTD derivative) as photoluminometric probes for temperature variation.

Finally, in Chapter 8, the general conclusion of this work is presented and suggestions for future developments are addressed.

1.3. Objectives

1.3.1. General objective

Develop spectrophotoluminometric analytical methods using a coordination compound containing europium, modified graphene quantum dots, and a new benzothiadiazole derivative as probes.

1.3.2. Specific objectives

- Develop an analytical method selective towards methylmercury using the $[\text{Eu}(\text{tta})_4](\text{Et}_3\text{NH}^+)$ as the analytical probe;
- Prepare new graphene quantum dots, in colloidal dispersion, that are sensitive to formaldehyde also providing proper characterization;
- Develop an analytical method selective towards formaldehyde using the N-GQDs-Ag dispersion as the analytical probe, also enabling the analysis of milk using headspace single-drop micro-extraction;

- Evaluate the photoluminescent responses, in function of temperature variation, of the $[\text{Eu}(\text{tta})_4](\text{Et}_3\text{NH}^+)$, the N-GQDs-Ag and the recently reported benzothiadiazole derivative (LASOC 460), either in solution or in polymeric films.

2 Theoretical Fundamentals

2.1. Chemical optical sensors

In chemistry, optical sensors are powerful analytical tools capable of providing information ideally about a particular analyte. In 1993, Czarnik [1] defined a chemical sensor or chemosensor as “*a micro or macroscopic device that reversibly interacts with a chemical analyte with signal transduction.*” Then, in 1994, Czarnik [2] defined that when there is a communication mechanism between a fluorophore and a compound that incorporates a binding site, the system is called a fluorescent chemosensor. If the binding site is an irreversible chemical reaction, the indicator is described as a fluorescent chemodosimeter. These two definitions and the term photoluminescent probe have been used interchangeably and ambiguously in recent decades. Therefore, the term used in this work to describe chemosensors will be luminescent probes.

The units of molecular recognition present in a photoluminescent probe interact with the target, providing information about their presence, concentration, and other physical properties of interest. When targets are molecules entering the system, the probes produce detectable changes in the signal that should be readily measured.

Different types of spectroscopic phenomena have been used in the sensing of chemical and biological species, including fluorescence [3-5], Raman scattering [6-7], and surface plasmon resonance (SPR) [8]. The choice of the optical response and probe must be made in the light of the desired performance indicators such as sensitivity, selectivity, and response time. These indicators are usually adequate in luminescence-based measurements, so luminophores have been widely used, mainly due to the sensitivity provided, good signal-to-noise relationship when compared, for instance, to Raman scattering [9], and better spectral resolution when compared to the detection of SPR [8].

In probes used in luminescence-based methods, units of molecular recognition have luminescent properties that change, generating detectable variation in optical signals. There are a variety of luminophores available for this use, including quantum dots [10], fluorescent proteins [11], organic dyes [12], and coordination compounds, where lanthanide coordination compounds [13] stand out. When new fluorophores are developed, besides sensitivity and high signal-to-noise ratio in chemical or biological environments, goals such as photostability, reproducibility of results, and reversibility of response need to be considered. When these goals are achieved, and luminophores are established as probes, it is then possible to evolve these probes to complete optical sensors, which are a broad class of devices for light intensity detection and can be either a simple component to notify when ambient light levels are above or below a prescribed level or a highly sensitive device to detect a single photon. The purpose of an optical sensor is to measure a physical amount of light and, depending on the type of sensor, translate it into a readable form by an integrated measuring device [14]. In simple terms, the operating principle of an optical sensor is based on the transmission and reception of light. Transmitted light can travel from the transmitter to the receiver over the air or through an optical fiber cable.

In this work we, do not aim to evolve the photoluminescent probes to optical sensors, but it is interesting to mention that this is a viable option that can be later explored.

2.2. Luminescence

The International Union of Pure and Applied Chemistry (IUPAC) defines the term luminescence as the “*spontaneous emission of radiation from an electronically or vibrationally excited species not in thermal equilibrium with its environment*” [15]. The nomenclature of the electronic luminescence phenomenon may vary depending on the nature of excitation of the matter. For example, photoluminescence occurs from direct photoexcitation of emitting matter. Some other types of luminescence are chemiluminescence, which is the emission of radiation resulting from a chemical reaction. Thermoluminescence is the

luminescence resulting from an increase in temperature. Triboluminescence is the emission of radiation resulting from the attrition of certain solids [15].

2.2.1. Photoluminescence of molecules

Photoluminescence, which was the type of luminescence measured in the present Ph.D. Dissertation, occurs when matter is excited with electromagnetic radiation at a specific wavelength (λ), producing the energy absorption from photons [16]. Considering molecules as fluorophores, when photons are absorbed, the population of molecules is excited, going from a lower energy electronic state to a higher energetic level [17]. Upon returning to the ground state, the population of molecules releases the absorbed energy in the form of emitted photons. The process of energy absorption and emission in photoluminescence can be understood through the modified Jablonski diagram (Figure 2.1).

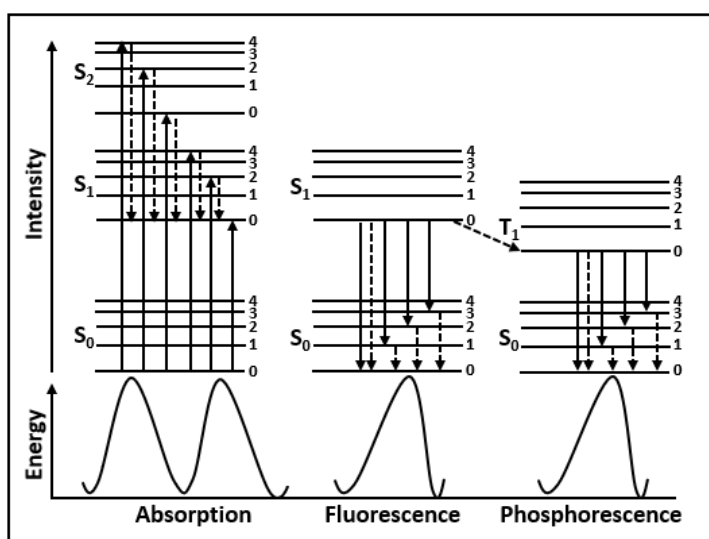


Figure 2.1 - Modified Jablonski diagram adapted from [18].

As a population of molecules absorbs the energy of incident electromagnetic radiation, they are promoted from the ground (usually singlet) state (S₀) to excited states of the same multiplicity (in general S₁, S₂) in a process of lifetime order of 10⁻¹⁵ s. At the excited states, the population of molecules goes through a fast vibrational relaxation process and decays (processes of a lifetime of about 10⁻¹² s). Non-radiative relaxation also occurs from higher energy excited singlet states (for

instance, S_2) to lower energy excited singlet states (for instance, S_1) without changing multiplicity ($\Delta S = 0$) in a process called internal conversion ($S_2 \rightarrow S_1$). As the population of molecules returns to the fundamental singlet state ($S_1 \rightarrow S_0$) by a radiative process, fluorescence occurs (time interval of $\sim 10^{-9}$ s). Due to relaxation and internal conversions (in solution also due to solvating processes), the emission band appears at longer wavelengths compared to the excitation band. In cases of high spin-orbital coupling, the intersystem crossing occurs, which is a non-radiative transition between two vibrational levels belonging to electronic states of different multiplicities ($S_1 \rightarrow T_1$), thus changing the multiplicity of the population. Following vibrational relaxation, the population of molecules returns from the first triplet excited state to the ground singlet state ($T_1 \rightarrow S_0$) in a radiative process that produces phosphorescence. Quantum-mechanics indicate such a process as prohibited (low probability) by the spin rule ($\Delta S \neq 0$). However, it occurs nonetheless because of the spin-orbit coupling that favors the intersystem crossing, causing the phenomenon of phosphorescence to be observed (lifetime of the order of 10^{-6} to 10^{-2} s), usually producing emission band at longer wavelengths (typical Stokes shift of hundreds of nm).

From the Jablonski diagram, it is possible to observe that some of the energy absorbed is dissipated as thermal energy, for example, instead of radiative energy. In this way, the energy that has been absorbed and later dissipated non-radiative way cannot be optically measured; thus, it becomes necessary to determine the quantum yield or quantum efficiency (that is identical to quantum yield for a primary photochemical process) of the emitting species. The quantum yield (Φ) can be defined as the ratio between the number of emitted photons in the photoluminescent process concerning the number of absorbed photons [15].

Another important spectroscopic property of emitting species is the attenuation coefficient (extinction coefficient) which can be expressed as the capacity of the emitting species to absorb light at a specific wavelength (light scatter is also considered when considering colloidal systems). This property is essential because it is also related to the photoluminescence emitted by the species of interest so that photoluminescent intensity is proportional to the product of the attenuation coefficient and the quantum yield [15].

Another relevant factor in photoluminescence is the Stokes shift, which is “the difference between the spectral positions of the band maxima of the absorption

and luminescence arising from the same electronic transition” [15]. Concerning the Stokes shift, usually when luminescence occurs at a wavelength that is longer than the one from absorption, the luminescence is stronger. When the opposite happens, the effect is known as anti-Stokes shift and occurs only in specific cases as some doped quantum dots.

2.2.2. Photoluminescence of rare earth complexes

According to IUPAC, the Rare Earth (RE) nomenclature is designated to scandium, yttrium, and the lanthanide elements (RE = Sc, Y, La – Lu). Although the Sc and Y elements present different electronic structures from the structures of the lanthanide elements, they have similar chemical properties and are therefore included in the RE group. The most common oxidation state for lanthanide elements is +3, which produces electronic configuration [Xe] 4f^N, where N varies from 0 to 14 (from La to Lu).

One of the most important characteristics of these elements is intrinsically contained in this configuration [Xe] 4f^N, where the electrons 4f^N, optically active, have a lower radial extension when compared to electrons in orbitals 5s² and 5p⁶. Electrons from 4f orbitals are shielded from the external environment by the filled 5s and 5p orbitals and therefore do not play a role in the chemical bonding between the lanthanide ion and any ligand. As a consequence, the influence of the matrix on optical transitions within layer 4f is small, resulting in narrow line emission spectra from either crystals or solutions [19-21]. In this way, 4f^N electrons interact weakly with neighboring atoms, and their electronic properties are only slightly affected by the chemical environment around the central metal ion because of the efficient shielding effect of the outermost sublayers 5s² and 5p⁶ [22]. These characteristics of RE³⁺ ions make them differ from other trivalent metal ions, for example, transition d metals, which are most strongly influenced by the chemical environment around them [23].

The intensities of the 4f-4f transitions in RE³⁺ ions depend on the chemical environment around these ions. As the Laporte rule quantum mechanically prohibits these transitions, RE³⁺ ions have low molar absorptivity values in the UV-vis spectral range, and the radiation intensity emitted by these ions is very low [24]. Weissman

[25] reported that when coordinating Eu^{3+} ions with organic ligands that presented great molar absorptivity in the ultraviolet region, the luminescence of the metallic ion increased considerably. This effect is known as the Antenna Effect, where ligands act as sensitizers of lanthanide ions through a light conversion process that occurs in a series of steps involving the absorption of energy by the ligand, the intramolecular energy transfer to the metallic ion, and the emission of energy by this ion. When these molecules (ligands) are coordinated to lanthanide ions, the energy from their triplet state can be transferred to the proper 4f energy levels of lanthanide ions that then decay to any of the sublevels in their ground energy levels, emitting photons.

Since rare earths are classified as hard acids, they better coordinate with hard bases, especially those containing nitrogen or oxygen. Thus, RE^{3+} ions can efficiently coordinate with ligands such as water, β -diketones, and bidentate aromatic amines, among others [26], and their coordination numbers can vary from 6 to 12, the most common being coordination numbers 8 and 9 [23]. The rare earth β -diketonate complexes are the most common rare earth complexes studied as they are easy to prepare, such ligands are of commercial availability, and because of the wide variety of reported applications of these complexes [27]. As the β -diketones bind to RE ions, they form chelate rings that give greater stability to these ions. Studies showed that the combination of molar absorptivity values of these types of ligands with their triplet energy states, somewhat above the emitting energy level of some RE^{3+} ions, charge distribution of the chelating ring, affecting hydrophobicity and spatial structure that influence the luminescent properties of RE^{3+} ions, many times improving them [28].

2.2.3. Photoluminescence of nanomaterials

In recent years, great attention has been paid to the various types of photoluminescent nanoparticles (NP) due to their chemical, physical and biological behavior and also to their different applications in various fields of science, especially in the areas of sensors [29], biosensors [30] and bioimaging [31].

Inorganic quantum dots are colloidal semiconductor nanocrystals that are usually composed of elements from groups II and VI, III and V and IV or VI of the

periodic table, where the most common types are QDs from groups II and VI, such as CdSe, CdTe, ZnS, ZnSe [32]. QDs were discovered in the 1980s by Alexei Ekimov [33] using glassy matrix and by Louis Brus [34] using colloidal dispersions, and since then QDs have been widely studied because of their unique properties. In terms of optical properties, QDs are photostable, making them resistant to photodegradation, they have large Stokes shifts, continuous and wide excitation spectra, and relatively narrow emission bands with high luminescence quantum yields.

The photophysical properties of inorganic QDs derive from the fact that their dimensions (typically 2 – 10 nm) are smaller than the distance between an electron in the conduction band and the hole in the valence band [35]. As the size of the QDs changes, so does the energy bandgap. Thus, the optical properties are directly related QDs size, and this effect is known as quantum confinement. The spatial confinement of the excitonic increases the energy bandgap between the valence band and the conduction band, producing its division at discrete energy levels [36-37].

QDs are theoretically described as zero-dimensional entities (three dimensions in the nanometric scale). Most of its properties depend on its size, shape, and composition and with different thermodynamic properties from macroscopic materials [35]. The quantum confinement effect is observed when the size of the material is small enough to be comparable to the wavelength associated with the moving electron. In this way, the energy levels are quantized, and the valence band and conduction band unfold into a set of discrete levels similar to atomic energy levels. Quantum confinement generally increases the bandgap as the QDs decrease in size. The bandgap in a material is the necessary energy to create an electron and a hole at rest, that is, with zero kinetic energy, at a considerable distance so that its Coulombic attraction is negligible. If one part approaches the other, they can form an electron/hole pair, that is, an excitonic whose energy is a little smaller than the bandgap. This excitonic behaves like a hydrogen atom, except that a hole, not a proton, forms the nucleus. The mass of a hole is much smaller than that of a proton, which affects the solutions to the Schrödinger wave equation [38].

The distance between the electron and the hole is the Bohr radius of the excitonic (r_B). If m_e and m_h are the effective masses of electrons and holes, respectively, the Bohr radius of the excitonic for a macroscopic semiconductor can

be expressed by Equation 2.1, where ϵ , \hbar , and e are the optical dielectric constant, reduced Planck constant and the charge of an electron, respectively [35].

$$r_B = \frac{\hbar^2 \epsilon}{e^2} \left(\frac{1}{m_e} + \frac{1}{m_h} \right) \quad (\text{Eq. 2.1})$$

If the radius (R) of a QD approaches r_B , that is, $R \approx r_B$, or $R < r_B$, the movement of electrons and holes is spatially confined to the dimension of the QD, which causes an increase in the energy transition of the excitonic and the observation of the blue shift in the QD bandgap and luminescence. The Bohr radius of the excitonic is a limit value, and the confinement effect becomes essential when the radius of the QD is smaller. For small QDs, the excitonic binding energy and the biexcitonic binding energy (excitonic-excitonic energy interaction) are much higher than for macroscopic materials [39]. For a material with a relatively high ϵ or smaller m_e and m_h , the r_B is larger.

A model known as EMA (Effective Mass Approximation) was developed by Brus in 1983 [40], and this approach is based on the particle-in-the-box model of quantum mechanics. The model assumes a particle in a potential well with an infinite potential barrier at the particle boundaries. For a free particle to assume any position in the box, the relationship between its energy (E) and the wave vector (k) is given by Equation 2.2.

$$E = \frac{\hbar^2 k^2}{2m^*} \quad (\text{Eq. 2.2})$$

In the EMA model, this relationship (Equation 2.2) is assumed to be valid for an electron or a hole in the semiconductor, so the energy band is parabolic near the edge of the band. The bandgap energy displacement (ΔE_g) due to excitonic confinement in a QD with a diameter R can be expressed as follows (Equation 2.3), where μ is the reduced mass of an electron-hole pair and E^*_{Ry} is the Rydberg energy.

$$\Delta E_g = \frac{\hbar^2 \pi^2}{2\mu R^2} - \frac{1.8e^2}{\epsilon R} = \frac{\hbar^2 \pi^2}{2\mu R^2} \left(\frac{1}{m_e} + \frac{1}{m_h} \right) - \frac{1.78e^2}{\epsilon R} - 0.248E_{Ry} \quad (\text{Eq. 2.3})$$

The first term of Equation 2.3 represents a relationship between the quantum location energy "particle in a box" or confinement energy and the radius of the QD (R), while the second term shows the Coulombic interaction energy with dependence on R^{-1} . The Rydberg energy term is size-independent and generally insignificant, except for semiconductors with a small dielectric constant [41]. Based on Equation 2.3, the first excitonic transition, or the bandgap, increases as the radius of the QD (R) decreases (the quantum location term shifts to higher energy with a lower value of R (R^{-2}), and the Coulombic term shifts the excited electronic state to a lower value).

Regarding the luminescent properties, after the QD is excited by external energy, such as photons, the electron and the hole have high energies due to the transition of electrons from the valence band to the conduction band. The energies associated with such optical absorptions are directly determined by the electronic structure of the material. As the excited electron and hole form an excitonic, the electron can then recombine with the hole and relax to a lower energy state, reaching the lower energy state again. The excess energy resulting from recombination and relaxation can be radiative (photon emission) or non-radiative (phonon or Auger electron emission).

Compared to inorganic nanocrystals (QDs), organic nanocrystals (CQDs - carbon quantum dots) are emerging as a new type of photoluminescent nanomaterial that offers similar attributes, such as small size under 10 nm, wavelength-dependent luminescence emission, resistance to photodegradation and the easiness of bioconjugation [42-43]. CQDs are alternative nanomaterials to traditional QDs as they employ low-cost and less exhaustive synthetic routes, long-term colloidal stability, elemental abundance, and low environmental and biological toxicity [42-44].

2.3. Characteristics and properties of the luminophores used as probes in this work

2.3.1. Eu³⁺ ions and their use as photoluminescent probes

One of the main advantages of studying systems containing Eu³⁺ is the easiness of interpretation of their spectra, based on the electronic structure of their energy levels since this ion has its main emitter state ⁵D₀ non-degenerate.

The spectroscopic properties of RE-containing materials have been widely studied based on the unfolding of the crystalline field of ^{2S+1}L_J sublevels from the 4F^N electronic configuration of the RE³⁺ ion [22, 45-46]. From the spectroscopy point of view, the trivalent europium ion has a high intensity of red monochromatic emission. It has also been considerably used as a luminescent probe due to the following requirements: i) the excited states ⁵D_J (J = 0, 1, 2 and 3) are well separated (12000 cm⁻¹) from the fundamental state ⁷F_J (J = 0, 1, 2, 3, 4, 5 and 6) and based on the number of bands observed in the unfolding maximum (2J+1) components of the transitions ⁵D₀→⁷F_J, the point symmetry of the chemical environment around the Eu³⁺ ion can be proposed; ii) the main emitting level ⁵D₀ and the fundamental state ⁷F₀ are non-degenerate, leading to a single ⁵D₀→⁷F₀ transition when the Eu³⁺ ion is located in a symmetry site of C_s, C_n or C_{nv} type. These spectroscopic properties facilitate the interpretation of spectral data that provide information on the possible existence of more than one site of symmetry in the chemical environment around the Eu³⁺ ion; (iii) the ⁵D₀→⁷F₁ transition, allowed by a magnetic dipole, is usually used as a reference transition because its intensity is practically insensitive to the disturbance of the crystalline field and, consequently, of the chemical environment; iv) long luminescent decay at ⁵D₀ level (up to the millisecond range) and v) large Richardson shift [47] — or pseudo-Stokes shift because the emission varies with the variation of the absorption bands — when emission spectra are obtained by direct excitation at ⁵L₆ level around 393 nm of Eu³⁺ ion or using higher energy excited states, belonging to ligands, inorganic or polymeric matrices.

The spectroscopic properties of Eu³⁺ have made it widely used for photoluminescent probing applications. A few examples of works that used Eu³⁺ as a probe are indicated below, only to show the variety of applications in this matter.

Li *et al.* [48] synthesized two different complexes using an amide-type β -diketone building block (N-(2-pyridinyl)benzoylacetamide or HPBA) and Eu and Tb (Eu-PBA and Tb-HPBA, respectively), and used them to design a paper-based lanthanide device for the detection of various acid-base vapors. Results showed that the photoluminescence of papers impregnated with Eu and Tb complexes after exposure to different acid vapors disappeared, and after exposure to alkaline vapors the photoluminescence was restored. These results permitted the devices to be used for the naked-eye detection of acid-base vapors with good response and reversibility and applied in anti-counterfeiting and logic operations.

Wang *et al.* [49] designed and synthesized a new “on-off-on” europium complex-based photoluminescent probe (BPED-BHHCT-Eu³⁺-BPT, where BPED is N,N-(2-pyridylmethyl)ethanediamine and BHHCT is 4,4'-bis(1'',1'',1'',2'',2'',3'',3''-heptafluoro-4'',6''-hexanedione-6''-yl)chlorosulfo-o-terphenyl and BPT is 2-(N,N-diethylanilin-4-yl)-4,6-bis(pyrazol-1-yl)-1,3,5-triazine), to allow visual detection of intracellular Cu²⁺ ions and H₂S. Results from the probe characterization and tests on these two species showed that the photoluminescence emission of the complex, at 611 nm, can be selectively quenched by Cu²⁺ due to its coordination with BPED moiety. The BPED group can then be released after contact with H₂S because Cu²⁺ and H₂S because of the great affinity in forming CuS, thus restoring the photoluminescence of the Eu³⁺ complex. The decrease in photoluminescence caused by Cu²⁺ and the enhancement caused by H₂S presented a good linear response in function of the concentration of either species. The LOD for Cu²⁺ was 0.038 $\mu\text{mol L}^{-1}$ and for H₂S was 0.22 $\mu\text{mol L}^{-1}$.

Huang and Pierre [50] presented a turn-on photoluminescent probe for CN⁻ detection in water containing Eu³⁺ (Eu^{III}-Lys-HOPO, where Lys is lysine and HOPO is 1,2-hydroxypyridonate). Results showed that the photoluminescence intensity of Eu^{III}-Lys-HOPO increased up to 9-fold in the presence of 100 equivalents of CN⁻ and that the mechanism of action of Eu^{III}-Lys-HOPO relied on direct coordination of CN⁻ to Eu³⁺ and the displacement of three inner-sphere water molecules. The turn-on response and the efficacy in water make the probe a promising candidate for environmental applications.

2.3.2. Graphene quantum dots and their use as photoluminescent probes

Carbon-based photoluminescent nanomaterials that are of great interest nowadays are CQDs [43], nanodiamonds [51], fragments of carbon nanotubes (CNTs), carbon nanotubes with functionalized-surface [52-53], graphene quantum dots (GQDs) [43], among others. These carbon-based materials have also been used as sensors as they present biocompatibility, low toxicity, and are easily produced from simple organic substances. As analytical probes, they are used in very low quantities due to their optical stability, high quantum yields, and intense luminescence [54].

GQDs are a type of CQDs that present themselves as flakes of graphene (isolated or stacked in low numbers) of nanometric sizes, connected to other chemical groups on the surface or at the edges, with high electron transport in the three spatial dimensions, which is basically due to small fragments available [55-57]. Unlike graphene, which does not luminesce [58-60], GQDs is a semiconductor, having suitable bandgaps for emissions in the visible range of the spectrum, extending to the near-infrared, due to their structural defects, elemental composition and surface groups present at the edges of the nanostructure [61-64].

Incorporating heteroatoms in GQDs has been an effective way to improve their optical properties [64-65]. The $\pi \rightarrow \pi^*$ transition of C=C bonds gives GQDs a strong absorption in the UV, extending to the visible range [43]. GQDs exhibit strong photoluminescence, with quantum confinement being one of the main reasons although, in many cases, there is no explicit dependency of the emission spectral position upon the nanomaterial size. However, it is believed that the photoluminescence of GQDs is a surface process and is not related to the sp^2 groups of the carbon structure. The general optical behavior of GQDs can be characterized by electron-hole recombination, by the contributions of the quantum confinement effect, doping elements, surface defects, and functional groups on the edges of GQDs [67].

The production of GQDs can be made in various ways affecting their sizes, color, and quantum yields. Li *et al.* described some combinations and variations of methods to prepare GQDs. The methods to prepare GQDs can be classified into two different groups: top-down and bottom-up. The top-down methods for synthesizing

GQDs include acidic oxidation, hydrothermal, microwave, ultrasonic chemistry, and electrochemistry, where carbonaceous materials such as graphene oxide, carbon black, and graphene are used as precursors. Bottom-up methods include photo-Fenton reactions, oxygen plasma etching, stepwise solution chemistry, precursor pyrolysis, and catalyzed cage-opening, where materials such as glucose, citric acid, C₆₀, and others are used as precursors. According to the method and precursor used, there will be a variation in the characteristics and properties of GQDs [68].

Since their discovery, GQDs have been proposed for applications in various fields of chemistry, physics, biology, and medicine, mainly due to their relevant photoluminescent characteristics. However, many questions are still to be answered concerning their synthetic methodology and photoluminescence mechanism that is not so clear. Therefore, many studies involving GQDs are concentrated on theoretical studies aiming to control the production of GQDs with high stability, controllable surface properties, and predictable and adjustable photoluminescence wavelength. In contrast, studies of analytical applications based on photoluminescence of GQDs are still secondary despite being very promising in some areas such as imaging and sensors. When used for analytical sensing, GQDs interact with analytes, resulting in either luminescence suppression or amplification, sometimes along with emission spectral shifts [68].

Masteri-Farahani and Askari [69] prepared and used GQDs as a luminescent nanosensor for the differentiation and determination of morphine and methamphetamine. The microstructure and optical properties of GQDs were investigated by various physical-chemical methods. X-ray diffraction (XRD) analysis indicated low crystalline nature, demonstrating the graphitic nature of GQDs. According to the Tauc graph, derived from the UV-Vis spectrum, the optical bandgap of the GQDs was determined at around 4.98 eV, attributed to $\pi - \pi^*$ transitions. Cyclic voltammetry analysis of GQDs determined the electrochemical bandgap of about 4.88 eV with HOMO and LUMO energies equal to -6.83 eV and -1.95 eV, respectively. Blue fluorescence of GQDs under excitation at 362 nm was suppressed in the presence of methamphetamine and amplified in morphine. The detection limits for methamphetamine and morphine were 1.48 and $0.5 \mu\text{g mL}^{-1}$, respectively. This low-cost sensor system has some advantages, such as short response time ($t < 1$ min) and low detection limit (LOD), as well as non-toxicity.

Achadu and Nyokong [70] described a functional hybrid of GQDs and pyrene-derivatized cobalt phthalocyanine (CoPc) as a sensitive nanoprobe for CN^- recognition. The luminescence of these hybrid GQDs was suppressed with the formation of non-covalent hybrids (π - π stacking) with CoPc through a possible energy transfer route. However, in the presence of CN^- ions, the interaction between GQDs and CoPc was disturbed so that the fluorescence of The GQDs, initially suppressed by the CoPc, was efficiently recovered in the presence of CN^- . Among many molecules and anions tested, only the CN^- ion-induced luminescence restoration of these hybrid GQDs, demonstrating the selectivity of the hybrid for CN^- . The restored luminescence signal was linearly modulated by different CN^- concentrations and was used for the quantitative CN^- assay with high sensitivity and rapid response time. The detection was linearly ranged from 1.0 to 50.0 nM with LOD of 0.5 nM. Analysis of enriched samples for CN^- recovery demonstrated the applicability of the hybrid for satisfactory detection of the analyte.

Qu *et al.* [71] synthesized new GQDs co-doped with nitrogen and sulfur (N,S/GQDs) by a simple green pyrolysis method with citric acid as a carbon source and D-penicillamine as the doping molecule. The N,S/GQDs showed good water compatibility, low cytotoxicity, and a high quantum yield of 56.4 %. N and S doping promoted efficient coordination between the residual group of N,S/GQDs and Hg^{2+} ; thus the luminescence of N,S/GQDs was drastically suppressed by Hg^{2+} . Under ideal conditions, the suppression effect of Hg^{2+} was proportional to concentration within the range of 0.9 to 30 nM, with a LOD of 0.69 nM. When HeLa cells were incubated in N,S/GQDs dispersions for 2 h, more than 85 % of the cells remained even at a nanomaterial concentration of $400 \mu\text{g mL}^{-1}$, suggesting good biocompatibility and low toxicity of the obtained N,S/GQDs. In addition, N,S/GQDs also showed good cellular permeability, showing a bright blue light. Thus, they were successfully applied as a luminescent nanosensor for imaging mercury ions in living cells.

In the Laboratory of Applied Spectro analytical and Electroanalytical (LEEA) at PUC-Rio, Toloza *et al.* [72] proposed the determination of captopril using GQDs produced by the pyrolysis of citric acid and glutathione (GSH-GQDs) which is supposed to be amino-functionalized GQDs. Captopril induced both suppression and red spectral shift in photoluminescence measured from aqueous dispersions of GSH-GQDs. By employing Fe^{3+} as a mediator (which allows the suppression of

luminescence), the presence of captopril restored the photoluminescence of GSH-GQDs. Under optimized experimental conditions, restoring the GSH-GQDs optical signal as a function of captopril concentration showed a linear response range covering three orders of magnitude (10^{-6} to 10^{-4} mol L⁻¹). The proposed approaches (based on luminescence quenching, spectral shifting, and restoration using Fe³⁺ as a mediator) were tested to determine captopril in simulated samples and commercial pharmaceutical formulations. Measurement of either the observed spectral shifting of the GSH-GQDs probe and the activation/deactivation of photoluminescence of GQDs-GSH-Fe³⁺ resulted in satisfactory captopril recoveries, showing potential for quantitative detection.

Tolozza *et al.* [73] also demonstrated the photoluminescence suppression effect caused by histamine on amino-functionalized graphene quantum dots (GQDs-GSH) with the mediation of Fe³⁺, Cu²⁺, and Eu³⁺. Results showed that the photoluminescence suppression (turn off) is stronger in the presence of Fe³⁺ and histamine recovered original luminescence from the turned-off GQDs-GSH with a linear response covering concentrations of histamine in the range of 4.3×10^{-7} mol L⁻¹ to 3.2×10^{-5} mol L⁻¹. This probe was used in the analysis of tuna fish samples. Tolozza *et al.* [74] also proposed indirect determination of kanamycin sulfate by measuring its effect on photoluminescence of amino-functionalized graphene quantum dots (GQDs-amino) associated with gold nanoparticles (AuNPs) in the presence of the surfactant CTAB. The dispersion of AuNPs-GQDs-amino-CTAB is sensitive to kanamycin, and the photoluminescence of the probe is increased as concentrations of the analyte becomes higher. The LOD was 6.0×10^{-8} mol L⁻¹, and the linear response was up to 1.0×10^{-5} mol L⁻¹.

De Falco *et al.* [75] investigated the toxicity of aqueous dispersions of GQDs with and without amino-functionalization, and *in vitro* tests were performed in *S. cerevisiae* and H9c2 cells. Cellular tests showed the low toxicity of the GQDs, indicating that when GQDs are amino-functionalized, they become less toxic. Microscopy results from cellular tests showed that GQDs interact with cellular membranes, presenting luminescence two times higher than the cells not treated with GQDs. These results suggest that the investigated GQDs have the potential to be used in cell marking in imaging techniques.

2.3.3. Benzothiadiazoles and their use as fluorescent probes

Benzothiadiazoles (BTDs) are a class of heterocyclic organic compounds containing a benzene ring fused with a thiadiazole ring in their nucleus. The simplest of the benzothiadiazoles is the 2,1,3-benzothiadiazole (the structure is illustrated in Figure 2.2).

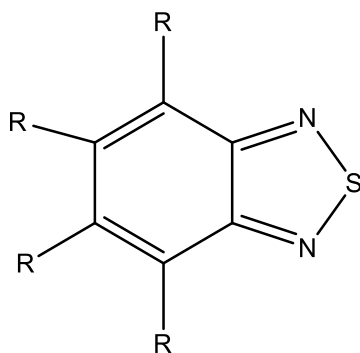


Figure 2.2 - Structure of 2,1,3-benzothiadiazole.

Overall, the net result of a π -extension at positions 4 and/or 7 of the BTD nucleus positively affects their photophysical properties, accompanying the new π -conjugated system [76-78]. By selecting proper substituent groups in the BTD ring [79-80], it is possible to adjust the photophysical properties of BTD derivatives [81] as they will reflect the effects inherent to the planned molecular architecture [82].

The 4,7-dibromo-2,1,3-benzothiadiazole is the most common intermediate used to synthesize of benzothiadiazoles containing π -extended fluorescent compounds. The intermediate can be easily prepared in two stages from ortho-phenylenediamine, as illustrated in Figure 2.3.

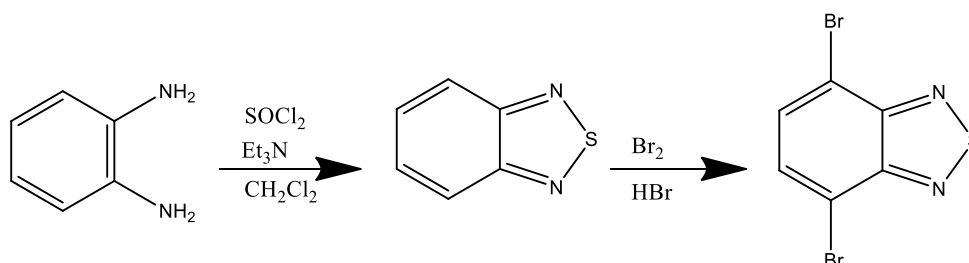


Figure 2.3 - Synthesis of 4,7-dibromo-2,1,3-benzothiadiazole.

In recent years, BTDs nuclei have become one of the most widely used fluorophores, being applied in the areas of luminescent technologies such as solar cells [83-85], probes for analytical [86] and biological [87] purposes, emitters in optical light devices [88-89], among others.

Regarding the chemical and photophysical properties that make BTDs so interesting, Neto *et al.* [90] gathered the most important reasons: (i) fluorescent derivatives of BTDs are usually stable and efficient fluorophores, even in excited states; (ii) the BTD ring has a strong electron-removing capacity and facilitates intramolecular charge transfer stabilization processes; (iii) BTDs have highly polarized properties that lead to intermolecular interactions, such as heteroatom contacts and π - π interactions, therefore usually with well-ordered crystalline structures; (iv) fluorescent BTDs usually exhibit large Stokes shifts and high quantum yields; (v) fluorescent emission of BTD-based bioprobes generally does not disappear even after long periods of irradiation; (vi) BTDs typically display bright emissions during the time periods of the cellular experience; (vii) the signal-to-noise ratio is usually very good for BTD bioprobes; (viii) BTDs are typically excited in the visible spectral range, facilitating acquisition of high quality images; (ix) theoretical calculations can be used as an important tool to predict the photophysical properties of fluorescent BTDs, thus allowing the synthesis of new structures guided by theoretical predictions.

BTDs are organic dyes with intense fluorescence in the solid state and in solutions. Although many organic dyes with strong emission in solution have been reported, in most cases, the fluorescence of these dyes is extinct in the solid state, mainly due to aggregation and intermolecular interaction. However, aggregation can also play an important role in the emission of these organic substances since the photophysical phenomena known as aggregation-induced emission (AIE) and aggregation-induced enhanced emission (AIEE) can induce non-emissive dyes to emit and low-emissive dyes to enhance their emissions, respectively. The aggregates of these molecules show stronger emissions than the solvated isolated species [119]. Even though organic dyes with intense fluorescence in both solid state and in solution have very interesting characteristics, their production is still limited. Therefore, the design and synthesis of luminescent materials that have luminescence in the solid state are also very attractive and of great importance,

especially in the sensing and imaging areas. Thus, some works that consider these characteristics are presented below, along with their applications.

Wu *et al.* [91] planned, synthesized and characterized two new derivatives of 2,1,3-benzothiadiazole, 7-(9-octyl-9H-carbazol-3-yl)-N-(4-nitrophenyl)-benzo[c][1,2,5]thiadiazol-4-amine (CBT-NH) and 7-(10-octyl-10H-phenothiazin-3-yl)-N-(4-nitrophenyl)-benzo[c][1,2,5]thiadiazol-4-amine (PBT-NH), for use as colorimetric and fluorescent sensors for fluoride, because these sensors contain hydrogen-bonded functional groups that act as interaction sites for this ion. When in solution in dimethylsulfoxide, both sensors exhibited a red color with binding studies showing that the compounds present colorimetric and fluorescent responses only for the F⁻ between eight tested anions, with LODs of 0.86 $\mu\text{mol L}^{-1}$ and 4.45 $\mu\text{mol L}^{-1}$ for CBT-NH and PBT-NH, respectively. Quantum yields were 0.034 for CBT-NH and 0.015 for PBT-NH. Both compounds can detect fluoride ions by a fast method that is also observable to the naked eye and showed a faster response of 5 s.

Alfonso *et al.* [92] developed two heteroditopic receptors derived from imidazo-benzothiadiazole, placing either a pyrrole unit or a triphenylamine unit in a specific position on the BTD structure. These compounds exhibit solvatochromism and selectively detect Hg²⁺, acetate, and nitroaromatic derivatives, with discrimination between p-nitrophenol and picric acid. To determine the ionic binding properties of the sensors, their absorption and fluorescent emission spectra when binding different cations and anions were compared, and significant changes in the spectra were only observed for Hg²⁺ and acetate. The stoichiometric relationship between the compound containing the pyrrole unit and acetate was 1:1, with an association constant (K_a) of $4.45 \times 10^5 \text{ M}^{-1}$ and LOD of $1.07 \mu\text{g mL}^{-1}$. The stoichiometric relationship between this compound and Hg²⁺ was 2:1, with $K_a = 1.98 \times 10^9 \text{ M}^{-2}$ and LOD of $0.13 \mu\text{g mL}^{-1}$. For the compound containing the triphenylamine unit, the stoichiometric relationship with Hg²⁺ was 2:1, with $K_a = 2.76 \times 10^8 \text{ M}^{-2}$. For acetate anion, this BTD did not show any significant difference compared to the one containing the pyrrole unit. Both compounds were shown to be sensitive to picric acid, and the stoichiometric ratio in both cases was 1:1, with $K_a = 8.2 \times 10^3 \text{ M}^{-1}$ and LOD = $159 \mu\text{g mL}^{-1}$ for the compound with pyrrole and $K_a = 4.49 \times 10^3 \text{ M}^{-1}$ and LOD = $317 \mu\text{g mL}^{-1}$ for the compound with triphenylamine.

Zou and Tian [93] synthesized two new luminescent probes based on 2,1,3-benzothiadiazole and their fluorescent behaviors towards various metal ions were investigated. One probe showed excellent optical properties and distinguished Hg^{2+} and CH_3Hg^+ from other ions in aqueous solutions. Although the second probe response towards Hg^{2+} and CH_3Hg^+ was slower than for the other probe, it was considered a promising fluorescent sensor for Hg^{2+} and CH_3Hg^+ due to the high selectivity. Evidence for the desulfurization mechanism was provided by UV-vis, fluorescence spectra, and especially ^1H NMR and high-resolution mass spectrometry (HRMS). The LOD values for Hg^{2+} (based on three times the standard deviation of background) were estimated to be in the 10^{-7} mol L^{-1} range, showing high sensitivity, and LOD values for CH_3Hg^+ were slightly higher. From spectral responses and HRMS analyses, a similar mechanism is proposed based on the formation of guanylation by the removal of CH_3HgSH induced by CH_3Hg^+ .

Recently, in collaboration with da Fiuza *et al.* [94], two polarity-sensitive ICT-based styryl-BTD derivatives were presented. One of these derivatives was more sensitive to environmental changes and was evaluated as a probe to chemosensing ethanol/water percentage in hydroalcoholic solutions. This BTD-based probe showed good linearity to variation of ethanol content in hydroethanolic solutions in the range from 40 % to 90 %, with fluorescence increasing with the increase in ethanol content. This probe was applied to discriminate ethanol content in different cleaning and sanitizing solutions.

2.4.

Properties and characteristics of analytes and physical parameters evaluated in this work

2.4.1.

Mercury

Discovered in ancient Greece, mercury is a metal of the transition series, block d, of group 12 and 6th period of the periodic table, presenting atomic number 80 and atomic mass 200.5 u. At room temperature, this metal is found in the liquid state and, for this reason, it received the name mercury, named after the Roman god who was the messenger of the gods, because of his fluidity. Also, for this reason, its chemical symbol is Hg, which comes from the Latinized Greek word hydrargyrum, which means liquid silver (“quicksilver”).

Mercury is a naturally occurring element found in water, soil, and air, and is distributed in the environment by natural or anthropogenic processes. The most important mineral where mercury is found, in the form of mercury sulfide (HgS), is cinnabar, and this ore can also come from volcanic deposits when sulfur is available. Mercury can also be found associated with gaseous and liquid hydrocarbons and coal deposits [95-96].

Mercury can also be found in several organic or inorganic forms, its most important forms being: (a) metallic or elemental mercury (Hg^0), which is volatile and is capable of producing odorless, colorless, and toxic vapors at room temperature. In the past, it was widely used in thermometers, barometers, manometers, mining activities, chloralkali industry, dental amalgams, fluorescent lamps, among others; (b) inorganic mercury (Hg^{2+} and Hg_2^{2+}) present in the salts obtained by combining mercury with other elements such as chlorine, oxygen, and sulfur. The most common salts are mercury sulfide (II), mercury chloride (I and II), and mercury acetate (II). In industry, inorganic mercury salts are used in batteries, biocides, paints and dyes, chemical reagents, among others; c) organic mercury present in compounds resulting from the combination of mercury and carbon chains, with methylmercury (CH_3Hg^+) being its most important form. Methylmercury can be obtained by biotransformation of inorganic mercury by sulfate-reducing microorganisms in rivers and seas. In the pharmaceutical industry, the use of thimerosal as an antiseptic or as a vaccine preservative may cause degradation, forming ethylmercury [97].

Another major source of anthropogenic mercury contamination is the use and production of fossil fuels, being the discharge of the water involved in petroleum production and processing, commonly known as produced water (PW), an important source of mercury. PW is a mixture of naturally occurring water and the water injected into the reservoir to increase oil recovery [98], being a by-product from the petroleum industry that is generated in large amounts [99] and also concentrating contaminants [100]. The determination of mercury in PW is not straightforward because of the high salinity of samples and dispersed hydrocarbons, requiring analytical methods that can be easily used in the production and processing sites.

Mercury is toxic in all its forms because it has an excellent affinity for thiol groups. Thiol is any organic compound that contains a univalent radical called

sulfhydryl and is represented by the symbol –SH. This class of compounds is present in several enzymes, hormones, and proteins of the human body. The interaction with mercury may cause the inactivation of these enzymes, structural proteins, or transport processes, or even alteration of cell membrane permeability by forming mercaptides. One enzyme in particular that mercury affects is glutathione peroxidase. This enzyme is very important because it helps to fight or neutralize certain substances, such as organic and inorganic peroxides, which, if not controlled, could destroy many of the cells in the human body [101].

The central nervous system is highly vulnerable to methylmercury toxicity, but the renal and the pulmonary systems are also susceptible because it is in these latter two that mercury is absorbed and spread to other parts of the body. At this point, we highlight the toxicity of methylmercury, fat-soluble, which facilitates its passage and absorption through body tissues [101].

The risks of mercury have become so worrying that since 2013 governments from several countries have been agreeing to the Minamata Convention on Mercury with the support of the United Nations (UN), which obliges these countries to take a number of actions to protect human health and the environment from the harmful effects of mercury.

2.4.1.1. Methylmercury

Methylmercury (CH_3Hg^+) is one of the most dangerous forms of mercury mainly due to its ability to be bioaccumulated and biomagnified through adsorption in surface bodies, in food intake (mainly fish), as well as due to their anthropic entry into the environment, up to a million times along the aquatic food chain [102].

There is a generic biogeochemical cycle in which Hg^0 , Hg^{2+} , and CH_3Hg^+ are interconverted into atmospheric, aquatic, and terrestrial systems. The exchange of inorganic species for methyl forms is the first step in aquatic bioaccumulation processes [97]. CH_3Hg^+ formation mechanism has not yet been fully elucidated, and although this compound is the predominant form of mercury in superior organisms, it represents only a small fraction of total mercury in aquatic and atmospheric ecosystems [97].

Once formed, methylmercury enters the food chain through rapid diffusion and strong binding with aquatic biota proteins, reaching its maximum concentration in fish tissues from the top of the aquatic food chain due to biomagnification [97]. Methylmercury is lipid-soluble and is known to be a neurotoxin that causes damage to the brain and nervous system, being particularly dangerous for pregnant women and infants as it can increase the risk of nervous system diseases and even babies born with deformities, even when the mother has no symptoms of poisoning [103-104]. Symptoms of methylmercury poisoning are of neurological origin and consist of visual disorders such as blurred vision and reduction of the visual field, ataxia, paresthesia, neurasthenia, hearing loss, and in cases of severe exposure, paralysis and death [102].

2.4.1.2.

Analytical approaches for mercury species determination

Mercury and mercurial compounds are the most targeted analytes in terms of the development of analytical methods, and through the years, a great variety of these methods have been developed to detect mercury species using different analytical techniques. For instance, in mercury, at ultra-trace concentrations, a limit of detection (LOD) of 0.26 ng L^{-1} has been determined in water using chemical vapor generation combined with atomic fluorescence spectrometry (AFS) [105]. Gas-chromatography coupled with AFS has also been extensively used for speciation allowing the determination of inorganic and organic mercurial species at the ng L^{-1} level [106-109]. Recently, nanoparticles have allowed kinetic control of Hg cold vapor formation from mercurial species, leading to speciation using atomic absorption spectrometry (AAS) with a multi-pass optical cell [110]. An extraction method using 2-mercaptoethanol to determine mercury species in biological samples was used previously to the determination by high-performance liquid chromatography coupled with inductively coupled plasma mass spectrometry (HPLC-ICP-MS), leading to LOD for methylmercury and inorganic mercury at $0.2 \mu\text{g L}^{-1}$ [111]. An electrochemical sensor for inorganic mercury, based on an ion-selective polyvinyl chloride membrane containing salicylaldehyde thiosemicarbazone, was developed and was capable of detecting $1 \mu\text{mol L}^{-1}$ ($200 \mu\text{g L}^{-1}$) [112]. The determination of CH_3Hg^+ was made in biological samples, after

solid-phase microextraction, by isotope dilution gas chromatography coupled to ICP-MS (LOD of 2.1 ng g^{-1}) [113].

A literature survey shows that, among the analytical methods, the ones based on spectroscopy techniques have received great attention. A review from 2013 [114] showed that more than 80 % of the reported methods for mercury and mercurial species are based on spectrometric techniques such as gas chromatography-cold vapor atomic fluorescence spectrometry (GC-CV-AFS), gas chromatography-cold vapor atomic absorption spectrometry (GC-CV-AAS), inductively coupled plasma atomic emission spectrometry (ICP-AES), inductively coupled plasma mass spectrometry (ICP-MS), spectrophotometry, and spectrofluorometry. More recently, another review [115] showed that researchers have been making efforts to expand the development of non-chromatographic methods for speciation of mercury, especially the ones based on the generation of cold vapor such as CV-AAS and CV-AFS, targeting organic mercury such as CH_3Hg^+ , aiming to simplify and reduce the cost of analysis.

Based on the advances of the studies found in the literature on the determination and speciation of mercury, the LEEA-PUC-Rio research group also sought to develop methods based on the CV-AAS technique using a dedicated mercury system. Miranda-Andrade *et al.* [116] developed a method for the indirect quantification of thiomersal with photodegradation assisted by GQDs. In this study, thiomersal was photo-oxidized and converted into ethylmercury, and then Hg^{2+} with the assist of GQDs and visible light, which was then converted to Hg through chemical reduction with SnCl_2 , and measurements were made with a portable atomic absorption spectrometer with an optical multipass cell. Results showed good linearity against the concentration of ethylmercury. The LOD is 6 ng L^{-1} , and LOQ is 20 ng L^{-1} . The method was efficiently applied to urine samples with recoveries of ~98 % and pharmaceutical industry effluent samples with recoveries of ~96 %. Miranda-Andrade *et al.* [117] also proposed a new method for mercury speciation in PW samples by measuring original mercury reduced with SnCl_2 and total mercury after photochemical treatment with UV radiation so that photo-reduction was not promoted in the original inorganic mercury sample. Determination of mercury was made on a portable CV-AAS system, and interference of salt and oil in samples was also studied. Results showed that the method reached an ultra-trace capability with LOQ of 12 ng L^{-1} . It also presented linear responses against mercury

concentration and good recoveries for all mercury species. Miranda-Andrade *et al.* [118] used a nanocomposite consisting of GQDs and TiO₂ nanoparticles to mediate photodegradation of mercury species in urine samples for measurements with CV-AAS. Mercury solutions samples in the presence of formic acid and GQDs/TiO₂ passed through a photochemical treatment in the reactor that was adapted to the spectrometer, and quantitative speciation was achieved due to the different kinetics in photocatalytic reactions. Limits of detection of 10 ng L⁻¹ for CH₃CH₂Hg and 7 ng L⁻¹ for Hg²⁺ and CH₃Hg⁺ were achieved.

Miranda-Andrade *et al.* [106] also developed a method for mercury speciation in PW samples using extraction and distillation before propylation followed by determination with GC-CV-AFS. In this study, extraction assisted with ultrasound in the presence of a surfactant helped recoveries in the distillation process to separate mercury species in the PW samples. After treatment with the propylation agent, measurements were made in a GC-CV-AFS system. Results showed that the LODs for Hg²⁺, CH₃Hg⁺, and CH₃CH₂Hg⁺ were 5 pg L⁻¹, 8 pg L⁻¹, and 11 pg L⁻¹, respectively, with recoveries of 92 %, 87 %, and 86 %, respectively.

Even though these methods have been efficiently used, in most cases, it is necessary chemical derivatization (usually propylation) or UV photoderivatization (to convert the organic mercury into inorganic mercury allowing speciation by differentiation of measured quantities before and after UV treatment) [106, 120-121]. Therefore, it is still important to develop simpler methods for on-site analysis, focusing on the detection of the more toxic mercury species, more specifically CH₃Hg⁺.

2.4.1.3.

Lanthanides as photoluminescent probes for mercury species determination

Lanthanide materials have been widely used as analytical sensors in recent decades [122-126]. Fluorescent probes based on materials containing lanthanide(III) ions for the detection of mercury species have received considerable attention [127-130] due to the diversity of complexes that may lead to some degree of selectivity and sensitivity related to their unique optical properties, including well-defined narrow emission bands, high quantum yields, high Stoke shifts and longer lifetimes.

For inorganic mercury, a lanthanide coordination polymer probe based on Tb(III) coordinated with ciprofloxacin and adenosine monophosphate (AMP) was developed. The Hg^{2+} interaction with AMP causes the fluorescence quenching of the complex. The probe showed great selectivity and sensitivity towards Hg^{2+} with a LOD of 0.16 nmol L^{-1} (32 ng L^{-1}), enabling its use in analyzing water and human urine samples [127].

A Tb(III) chelate was used to detect Hg^{2+} in environmental water and biological samples. The lanthanide chelate, consisting of a quinolone-based dye molecule and a polyaminocarboxylate-based chelator binding to Tb^{3+} , interacts with Hg^{2+} producing fluorescence quenching within the linear range between 4 to 600 nmol L^{-1} (0.8 to $1200 \text{ } \mu\text{g L}^{-1}$) [128].

Another Tb(III) complex, produced using a pyridine derivative, was used for time-gated luminescence detection of Hg^{2+} with LOD of 17 nmol L^{-1} ($3.4 \text{ } \mu\text{g L}^{-1}$) [129].

A dual-emission fluorescent probe, combining two lanthanide chelates, was developed for the determination of Hg^{2+} in milk samples. The Tb(III) chelate was embedded into SiO_2 nanoparticles while the Eu(III) chelate was covalently linked to the surface of the silica shell. In the presence of Hg^{2+} , the characteristic Eu(III) fluorescence is quenched while the Tb(III) fluorescence remained the same, allowing a robust ratiometric measurement with LOD of 7 nmol L^{-1} ($1.4 \text{ } \mu\text{g L}^{-1}$) [30].

When it comes to methylmercury determination through lanthanide photoluminescence, only a few works have been reported. A dinuclear Eu cluster was developed to sense of CH_3Hg^+ in water samples. The linear response was in the range of 1.4 to $3.8 \text{ } \mu\text{g L}^{-1}$ with a LOD of $0.8 \text{ } \mu\text{g L}^{-1}$ [131].

A dinuclear Tb(III) complex was used as a bifunctional sensor for the detection of both SO_4^{2-} and CH_3Hg^+ in water samples, with LOD of $2.8 \times 10^{-9} \text{ mol L}^{-1}$ ($0.62 \text{ } \mu\text{g L}^{-1}$) for CH_3Hg^+ [132]. A cyanine dye, modified with lanthanide-containing nanophosphors, was proposed for the monitoring of CH_3Hg^+ , *ex vivo* and *in vivo*, by up-conversion luminescence bioimaging. The LOD for this nanoprobe was $0.18 \text{ } \mu\text{g L}^{-1}$ [133]. More recently, a dual-signal probe, based on a boric acid-functionalized lanthanide metal-organic framework, was used to detect both Hg^{2+} and CH_3Hg^+ in water samples with “turn-on” signal output [134]. The

LOD for Hg^{2+} and CH_3Hg^+ were 220 nmol L^{-1} ($47.3 \text{ } \mu\text{g L}^{-1}$) and 440 nmol L^{-1} ($94.6 \text{ } \mu\text{g L}^{-1}$), respectively.

However, in terms of real applicability, most of the probes reported in the literature have limitations, such as restricted conditions for sensing, complicated and/or time-consuming synthetic routes for the probes, instability of response, and slow response to the analyte.

2.4.2. Formaldehyde

Formaldehyde is a naturally occurring aldehyde that, at room temperature, is a colorless and flammable gas with a suffocating odor, being easily soluble in polar solvents, in which formalin (36.5 – 38 % w/v in H_2O) is its most common and known solution. It is extensively used in the manufacture of resins and polymers, fabrics and, pressed wood products, also employed in pharmaceutical and cosmetic industries because of its preservative and antibacterial properties [135] and as a conservative in some foodstuffs [136]. Acute human exposure to formaldehyde can cause several health problems, such as allergies, asthma, neurological damage, and even cancer [135-139].

Dairy products are notable perishable food as they are highly susceptible to bacteria and mold. Pasteurization and similar treatments at high temperatures are effective and safe to prevent dairy deterioration. However, many fraudulent practices are employed to distort milk and its derivatives quality, including the addition of formaldehyde because of its antiseptic and preservative properties that improve appearance and smell, especially when dairy products are not handled hygienically [140-141]. Such practice is of concern as it exposes humans to formaldehyde. Therefore, strict quality control of dairy products, especially milk, is required. In Brazil, the Ministry of Agriculture, Livestock, and Supply (MAPA) determines that formaldehyde analysis in milk is carried out according to the official method 931.08 of AOAC International [142-143], where formaldehyde is separated from milk by distillation after addition of phosphoric acid. An aliquot of the distillate is added to an aqueous solution containing chromotropic and sulfuric acids, and the resulting mixture is heated. If formaldehyde is present in the mixture, a violet compound is formed.

2.4.2.1.

Analytical approaches for the determination of formaldehyde

A wide variety of methods based on conventional analytical techniques are available to determine formaldehyde in milk and its derivatives. Because of the complexity of dairy matrices, they usually involve some degree of sample treatment, as they often determine formaldehyde directly in the sample. Methods based on high-performance liquid chromatography (HPLC) are the most commonly used, requiring extraction and chemical derivatization of the analyte (usually with 2,4-dinitrophenylhydrazine, DNPH). For instance, to analyze bovine milk, a liquid-liquid extraction with low temperature partitioning was used along with precipitation of sample proteins and fat before introduction into HPLC system. The limit of detection (LOD) was $3.0 \mu\text{g L}^{-1}$, and recoveries were $102.2 \pm 1.3 \%$ using photometric detection after derivatization with DNPH [144]. Another method based on HPLC to determine formaldehyde in dairy products, including milk, used precipitation of proteins with trichloroacetic acid before DNPH derivatization leading to LOD of 0.4 mg L^{-1} and recovery above 94% [145]. Alternatively, dairy products samples have been treated with a warm organic solvent, in the presence of DNPH, to extract and derivatize formaldehyde before HPLC analysis, enabling LOD of 0.01 mg kg^{-1} and recovery between 89 and 96% [146]. Gas chromatography with detection by mass spectrometry (GC-MS) has been used, combined with solid phase micro-extraction, to determine formaldehyde in different foods and beverages, including milk. Derivatization with O-(2,3,4,5,6-pentafluoro-benzyl)-hydroxylamine hydrochloride was used, and LOD in milk was 12.20 ng g^{-1} [147].

Spectrophotometric methods require the use of chromophores to enable near UV-visible range detection. An absorption spectrophotometric method to determine formaldehyde in milk employed the Hantzsch reaction for the derivatization of formaldehyde, and the product was extracted with trihexyltetradecylphosphonium chloride solution. LOD was $100 \mu\text{g L}^{-1}$, and recoveries in different milks ranged from 91% to 106% [140]. Automation was proposed to determine formaldehyde in milk after adding trichloroacetic acid to remove proteins and continuous dialysis prior to the injection into the carrier stream of a flow analysis system. The method was based on the reaction of formaldehyde with fuchsine-sulphur dioxide

(absorbance at 556 nm) with a linear response between 0.1 and 1.4 mg L⁻¹ of formaldehyde [148]. A two-photon fluorescent probe was reported to quantitatively detect residual formaldehyde in milk. The probe was obtained by reacting 6-bromo-1H-benzo[de]isoquinoline-1,3(2H)-dione with hydrazine hydrate. After incubation with the analyte, a strong fluorescence enhancement of the probe led to a LOD of 1.62 μmol L⁻¹ (about 50 μg L⁻¹) [149].

Electroanalyses are usually plagued by poisoning of electrodes due to other species from the complex matrices, even after sample treatment. A voltammetric electronic tongue was proposed to discriminate adulterated milk (with formaldehyde and other contaminants) from unadulterated milk. Three different working electrodes were used (gold, copper, and platinum) and inserted directly in samples, without any pre-treatment, for measurements with a reported LOD of 10.0 mmol L⁻¹ (0.3 g L⁻¹) for formaldehyde [150]. An electrochemical sensor, based on a glassy carbon electrode modified with gold nanoparticles and polypyrrole, was used to detect formaldehyde in milk after extracting formaldehyde with steam distillation (reported LOD of 0.4 mmol L⁻¹ or 12 mg L⁻¹) [151]. Other methods based on infrared spectrometry (IR) [152-155], time-domain nuclear magnetic resonance (TD-NMR) [156], and electrical impedance [157] have also been reported for the determination of formaldehyde in milk and derivatives.

However, despite these methods being highly sensitive and selective, they usually have complicated experimental manipulations, high cost, and long detection times, as is the case of the chromatographic techniques or the electroanalysis methods, where the poisoning of electrodes can occur or even on the spectrophotometric methods where toxic and expensive chromophores are often used.

Aiming the development of practical methods that rely on minimum sample preparation and production of low quantities of toxic residues, in addition to appropriate figures of merit and adequate metrological features, optical sensors for the detection of formaldehyde have received wider attention recently. Among these optical sensors, luminescence-based ones present advantages in terms of easiness of operation and sensitivity.

Martínez-Aquino *et al.* [158] proposed the detection of formaldehyde by using a probe prepared by dipping a silica-gel plate into solutions of dopamine,

glycine, and sucrose. Colorimetric or fluorescence changes produced by formaldehyde in solution allowed LOD of 0.24 mmol L^{-1} (7.2 mg L^{-1}).

Li *et al.* detected formaldehyde in aqueous solutions using chitosan-based fluorescent polymers functionalized with hydrazino-naphthalimide (HN-chitosan) in which formaldehyde reacts with grafted hydrazino-naphthalimide groups, increasing measured fluorescence and leading to quantification within the linear range of $1 - 100 \text{ mg L}^{-1}$ in aqueous solutions besides response time of less than 1 min and photostability [159].

Recently, Ding *et al.* constructed a resonance energy transfer ratiometric sensor by conjugating a two-photon donor (π -push-pull-structure) with a formaldehyde off-on acceptor (functioned with hydrazide moiety). The absorption is red-shifted when the sensor is in the presence of formaldehyde, also causing photoluminescence to increase with emission color changing from blue to yellow. The LOD of 8 nmol L^{-1} ($0.24 \text{ } \mu\text{g L}^{-1}$) was obtained by monitoring the ratio of signals at 550 nm and 426 nm [160].

Veríssimo *et al.* used an optical fiber, tip-coated with a polyoxometalate salt, as a sensor for formaldehyde in milk, previously cleaned up through centrifugation with trichloroacetic acid. Absorbance changed in the presence of formaldehyde as one of the bands decreased, leading to a LOD of 0.2 mg L^{-1} [161].

2.4.2.2.

GQDs as photoluminescent analytical probes for the determination of formaldehyde

The use of GQDs as luminescent probes to determine formaldehyde has been previously reported. Zhang *et al.* [162], using graphene quantum dots doped with nitrogen from ammonia (N-GQDs) and melamine, produced a photoluminescence sensor for quantitation of formaldehyde in aqueous solutions (within $0.3 - 30 \text{ } \mu\text{mol L}^{-1}$ or $9.0 - 900 \text{ } \mu\text{g L}^{-1}$) as measured photoluminescence from the water dispersed N-GQDs/melamine decreased as analyte concentration increased.

Li *et al.* [163] used a different type of N-GQDs as probes for formaldehyde in an aqueous solution. N-GQDs were produced, mixing citric acid and urea through the hydrothermal route, then encapsulating the nanomaterial using organic species (O-NGQDs) that caused color changing when exposed to atmospheric oxygen as redox reactions affect photoluminescence measured from the nanomaterial

dispersion. Formaldehyde interacted with O-NGQDs, linearly causing photoluminescence quenching with a LOD of $0.15 \mu\text{mol L}^{-1}$ ($4.5 \mu\text{g L}^{-1}$).

Zhang *et al.* [164] proposed a probe to detect formaldehyde, in aqueous solutions and food extracts, based on the use of GQDs, obtained by heating citric acid in an oil bath and then dispersing the resultant liquid into NaOH solution. Formaldehyde interacts with GQDs causing photoluminescence quenching that correlated linearly between $0.05 \mu\text{g}$ and $1 \mu\text{g mL}^{-1}$.

Although these probes presented good responses towards formaldehyde, they are still limited to simple aqueous matrices, in some cases requiring long periods (2 h, 8 h) to allow effective interaction between the analyte and these GQDs.

2.4.2.3.

Headspace single-drop microextraction (HS-SDME) technique

In the case of volatile analytes such as formaldehyde, headspace single-drop microextraction (HS-SDME) allows sampling, extraction, and analyte pre-concentration on a single micro-drop of an extracting agent exposed to the headspace above the sample. Such a procedure eliminates interferences imposed by non-volatile or less volatile components of the sample matrix as the analyte is separated due to controlled volatilization and diffusion into the extracting solvent that composes the hanging drop. Taking advantage of formaldehyde volatility and considering the advantages provided by both HS-SDME [187-188] and GQDs as analytical probes [158-161], analytical sensing of formaldehyde in milk samples was successfully achieved in a simple way. The GQDs proposed in the second part of this work were doped with nitrogen and modified with silver (N-GQD-Ag) and were produced by a hydrothermal route utilizing citric acid, urea and Tollen's reagent. There are no reports in the literature on the use of N-GQDs modified with Ag (using the Tollen's reagent) to determine formaldehyde. Tollen's reagent, composed of $[\text{Ag}(\text{NH}_3)_2]^+$, differentiate aldehyde from ketone functional groups as the former is readily oxidized along with the reduction of Ag^+ (in alkaline medium) [165]. Aiming high selectivity and virtually no sample preparation, a nanomaterial aqueous dispersion drop was hung onto the headspace above the milk sample, letting formaldehyde vapor be absorbed and interact with the N-GQD-Ag, that was then transferred to a quartz cuvette for photoluminescence measurement.

2.4.3. Temperature

2.4.3.1. Temperature sensors

Temperature (T) is one of the most important physical parameters, and therefore there is a need for its control and measurement in simple and fast ways. There is a wide variety of types of thermometers and temperature sensors available where one of the most common are the analog mercury thermometers based on the phenomenon of thermal expansion of liquids. However, because of the error associated involving expansion measurements and concerns about the environment and human health, due to the toxic nature of mercury (in cases of broken thermometers), there is now a necessity to replace these types of thermometers with others that are easier to operate, non-toxic and environmentally friendly [166]. In this way, digital thermometers began to be used, and, like the analog ones, they need to be in contact with the body so that there can be thermal balance and thus have the response of the temperature value [166].

Thermocouple thermometers work through the potential difference generated by two different metals at different temperatures. The advantages of using thermocouple thermometers are their non-toxic nature, robustness, and low cost, besides being accurate and useful within a wide temperature range [167]. Even though digital and thermocouples thermometers have good advantages compared to mercury ones, they also have some disadvantages such as the fact that they need an electronic display to obtain the temperature. Thermocouple thermometers also have other limitations because they require an electrical link to the sensor and can be sensitive to corrosive environments and the presence of electromagnetic fields [166]. Thus, other temperature sensors have been explored to circumvent these limitations.

Optical sensors for temperature have been widely used instead of those based on mercury and thermocouple. Infrared thermometers based on black body radiation were one of the first optical sensors for temperature and are used when direct contact with the matter has to be avoided. However, infrared thermometers can only be used for temperature measurement on surfaces, and they constantly require a very precise calibration [166].

Nowadays, in substitution to the infrared thermometers, one of the most used optical sensors for temperature are the ones that use optical fibers, and they can be based on different physical principles, including reflection, absorption, scattering, and luminescence. The different types and their principles have been reviewed [168], but they all operate in converting optical signals to the temperatures measured. Also, they have advantages such as the use in wide temperature ranges, are not sensitive to electromagnetic interference, and do not need electrical cables, which is important for application at high voltages [166].

Among the optical sensors for temperature, luminescence-based ones have attracted great attention. They are, for the most part, constituted of luminescent organic and inorganic luminophores or nanoparticles that can be embedded in the studied matrices or deposited in their surfaces. After receiving electromagnetic radiation, luminescence is detected by its intensity or lifetime profile, T-dependent [166]. These devices also allow the temperature measurement of small objects, making these probes applicable for different purposes.

Theoretically, all luminescent materials have their emissions dependent upon temperature, and this dependence is a function of the specific electronic bands of the material that allows non-radiative decays, that is, the higher the non-radiative decay, the greater the decay in the emission intensity that is known as the phenomenon of thermal quenching [166]. Luminescence lifetime is also reduced as temperature increases affecting decay of population in excited state.

2.4.3.2.

Lanthanide complexes as photoluminescent probes for temperature

The use of lanthanide complexes as luminescent probes for temperature has been reported in the literature. Getz *et al.* [169] prepared thin films of $\text{YVO}_4:\text{Ln}^{3+}$ (where Ln = Nd, Sm, Eu, Dy, Ho, Er, Tm, Yb) using the atomic layer deposition (ALD) technique with films thickness between 100 and 150 nm. They investigated how the emission of single and dual films is affected by temperature in the range of 300 to 850 K. They also showed how ALD technique could be used to prepare films containing different Ln ions in order to provide sensitivity in a broad temperature range. Results showed sensitivities reaching 1.2 % K^{-1} for $\text{YVO}_4:\text{Er}^{3+}$ at 300 K and 0.6 % K^{-1} for Eu^{3+} at 575 K. For $\text{YVO}_4:\text{Eu}^{3+}/\text{YVO}_4:\text{Dy}^{3+}$ and

YVO₄:Tm³⁺/YVO₄:Eu³⁺, the dual-layered materials exhibit maximum sensitivity of 3.6 % K⁻¹ at 640 K, significantly improved in the range of 500 to 775 K when compared to the single-layer YVO₄: Eu³⁺ thin film, and also compared to any other previously investigated materials in this range. These films were deposited in silicon, iron, quartz, steel, glass, and aluminum substrates showing that they can be applied to most industrial surfaces.

Runowski *et al.* [170] used YVO₄:Yb³⁺-Tm³⁺ nanoparticles as a sensitive and accurate way to monitor temperature values up to 1000 K. Results showed that the size of nanoparticles is less than 100 nm, and it exhibits up-conversion luminescence of Tm³⁺ and intense emission of Yb³⁺. Using thermally coupled levels (TCLs) of Tm³⁺ (700/800 nm) and non-TCLs of Yb³⁺/Tm³⁺ (940/800 nm), results showed that these bands are very intense even in higher temperatures and that their intensity ratio changes significantly with high sensitivity of 2.1 % K⁻¹ and thermal resolution of 1.4 K, which allows accurate sensing of temperature.

Guimarães *et al.* [171] prepared, characterized, and applied new Tb³⁺/Eu³⁺ tetrakis(benzoyltrifluoroacetone) complexes with imidazolic counterions as a highly sensitive and precise optical sensor for temperature. The complex formula was confirmed as being [C₄mim][Tb_{1-x}Eu_x(btfa)₄]. Results of thermal tests showed relative thermal sensitivity around 7.6 % at 20 K and a minimum temperature uncertainty below 0.03 K. Excitation at the ligand (360 nm) allows shifting in the operating range of the thermometer with maximum sensitivity > 1 % in the interval of 20 to 200 K and for excitation at Tb³⁺ ion (489 nm) the interval is 150 to 225 K. Combination of both excitations shows that the luminescent thermometer can be used for an extended temperature range. They can also be used with excitations in the blue and UV spectral regions with low minimal temperature uncertainty. Results suggest that the films can be applied as photonic temperature sensors.

Salas-Juárez *et al.* [172] designed a new transparent film based on Tb/Eu-TPTZ (where TPTZ is 2,4,6-Tris(2-pyridyl)-1,3,5-triazine) incorporated in polymethyl methacrylate (PMMA), and its use as a photoluminescent thermometer and visual temperature sensor was evaluated. Results showed temperature dependence in the range of 25 to 120 °C for the transitions ⁵D₄→⁷F₅ of Tb³⁺ and ⁵D₀→⁷F₂ of Eu³⁺ with decays of 94 % and 76 %, respectively. At 100 °C, absolute sensitivity is 1.3 % C⁻¹, and relative sensitivity is 2.98 % C⁻¹ with temperature resolution better than 0.05 °C and linear behavior in the range of 25 to 100 °C with

$R^2 = 0.997$. A color change was observed from greenish-yellow to red as the temperature increased. These results and characteristics suggest that the film can be considered a good luminescent thermometer and visual temperature sensor.

2.4.3.3.

GQDs as photoluminescent probes for temperature

In recent years, luminescent GQDs have received considerable attention as temperature probes. Park *et al.* [173] developed a colorimetric sensor using block copolymer-integrated GQDs (bcp-GQDs) for simultaneous sensing of pH, temperature, and metal ions. Results indicated that bcp-GQDs were temperature-sensitive in the range of 25 to 40 °C, with the intensity of the blue-emission peak at 410 nm decreasing and the emission in the peak at 505 nm increasing, showing a color change to green. The fluorescent lifetime of bcp-GQDs showed a similar behavior where it decreased at the temperature above the lower critical solution temperature (LCST). These results and those of pH and metal ions tests, suggest that bcp-GQDs can be used in various sensor systems.

Kumawat *et al.* [174] reported the fabrication of GQDs by a one-pot microwave-assisted green synthesis route using mango leaves (*Mangifera indica*) as the precursor and their use as a temperature-sensing probe. GQDs prepared from mango leaves extracts showed good stability, lifetime and red emission. Temperature tests with GQDs dispersions made in the range of 10 to 80 °C showed that their fluorescent intensities decreased about 58 % with the increase in temperature. Tests with L929 cells pre-incubated with GQDs showed a decrease in the fluorescent intensity up to 95 % when the temperature increased from 25 to 45 °C, which indicates that it can be used to detect the minute temperature variation in the cellular environment.

Nguyen and Kim [175] presented a hydrothermal method to produce blue-luminescent GQDs by intercalating graphite nanoparticles with subsequent exfoliation and their use as a sensing material for temperature measurement where the temperature sensor was constructed using a resistor structure based on a glass substrate and GQDs films. Results showed that GQDs have average diameters of 3-4 nm and have a quantum yield of 22.3 %. The response to temperature changes was studied by measuring the current-voltage of devices in the range of 30 to 80 °C,

and results showed that the current increased when temperature increased, and this behavior was explained by the charge transport mechanisms inside the GQDs network film. The sensitivity of GQDs is about 0.62 %, which is greater than sensors based on gold or PIN diodes.

Gao *et al.* [176] prepared two structures-defined water-soluble GQDs with different oxidation degrees using a bottom-up synthetic route and the reduction method using NaBH_4 . The GQDs were then applied as temperature-responsive fluorescence probes in the HeLa cell line. Results from the temperature tests in the physiological range from 0 to 60 °C in aqueous solutions showed that reduced GQDs (R-GQDs) have a linear relationship with temperature with $R^2 > 0.999$, while the linearity of oxide GQDs (O-GQDs) only covers the range of 0 to 40 °C, also with $R^2 > 0.999$. Also, R-GQDs showed a higher quantum yield of 3.4 %, while O-GQDs showed a quantum yield of 1.4 %. These results showed that R-GQDs can be used as temperature luminescence nanosensors with wide application fields. Tests with HeLa cells showed that the fluorescent intensity of R-GQDs decreased with the temperature increase, confirming that they can be applied as a nanothermometer for intracellular temperature imaging.

Lee *et al.* [177] synthesized graphene quantum dots through the top-down method with UV-assisted chemical oxidation/exfoliation of reduced graphene oxide (RGQDs) and through the bottom-up method using microwave-assisted hydrothermal treatment where glucosamine was the precursor (N-GQDs) and applied them as luminescent nanothermometers for HeLa cells. Results showed that both GQDs have a linear temperature-dependency of 25 to 49 °C for visible emissions with $R^2 = 0.995$ and quenching of 19.3 % for N-GQDs and $R^2 = 0.967$ and quenching of 16.8 % for RGQDs. For near-infrared emission, RGQDs presented $R^2 = 0.995$ and quenching of 6.74 %. Tests *in vitro* in HeLa cells in the range of 25 to 45 °C showed a quenching response of over 40 %, suggesting that the GQDS can be used for temperature sensing in microscopic sub-cellular biological environments.

2.4.3.4. BTDs as fluorescent probes for temperature

BTDs have been widely used for different purposes, still they have not been extensively used as temperature sensors, even though temperature is one of the parameters that can affect the fluorescence of these molecules (both in non-aggregated and aggregated forms). The enhancement of temperature can cause restrictions of intramolecular rotations and/or vibrations in these molecules, producing decrease of fluorescence [119]. Some studies in the literature indicating that BTDs can be explored as thermosensors are described. Uchiyama *et al.* [178] developed two intramolecular charger-transfer-type environment-sensitive fluorophores and created a molecular nanogel thermometer as an intracellular sensor. Results showed that disubstituted benzothiadiazole and benzoselenadiazole molecules (DBThD-IA and DBSeD-IA, respectively) were obtained, and photophysical studies in different solvents showed that in less polar or less protic solvents, the fluorophores have longer lifetimes and higher quantum yields. Results from photostability tests showed that the quantum yields for photodecomposition were $1.6 - 5.9 \times 10^{-4}$ for DBThD-IA and $0.8 - 12 \times 10^{-3}$ for DBSeD-IA which suggests that DBThD-IA is more stable under photo-irradiation and, because of these results, DBThD-IA was used in the development of a fluorescent nanogel thermometer. Tests towards temperature change in COS7 cells showed that the fluorescent intensity of DBThD-IA nanogels increased when temperature increased from 23 to 35 °C, and the fluorescent lifetime was extended when temperature increased from 0 to 32 °C, proving that the nanogels can be applied as a nanothermometer for intracellular studies.

Echeverri *et al.* [179] synthesized a new rod-shaped benzothiadiazole fluorophore (4,7-di-(4-nonylphenyl)benzo[c][1,2,5]thiadiazole) and its photophysical properties were studied. The molecule was then blended with polymeric matrices that were thermally investigated, and the results showed that fluorescence emission is solvent-dependent with quantum yield in CH₂Cl₂ of 0.52. Tests with polymers showed that by heating the polymeric films containing the BTD molecule up to 75 °C, there is a color change from blue to green which is due to conversion from what authors called polymorph A to polymorph B. These results expand the applicability of the material to the thermal sensing area, among others.

Zhao *et al.* [180] designed a tetracarboxylic acid ligand containing a benzothiadiazole moiety and used it to construct the porous MOF ZJU-21, which can absorb the luminescent dye DMASM into the pores and sensitize it forming the composite ZJU-21-DMASM that was used as a luminescent thermometer. Results from tests with this composite showed that its luminescence color could be tuned from green to red when the amounts of DMASM are adjusted in the pores of the host framework. Temperature tests showed that when the temperature increases from 20 to 80 °C, the emission intensity of the composites also increased, where it is believed that energy is transferred from DMASM to the linker when temperature increases which causes the enhancement of the emission intensity from the linker within the composite. These results provide a new perspective for the design of MOF-dyes ratiometric temperature sensors.

3 Experimental

3.1. Instruments and apparatuses

Photoluminescence measurements were made on a model LS 55 luminescence spectrometer (Perkin-Elmer, UK) using a 1000 nm min⁻¹ scan rate and 10,0 nm spectral emission and excitation bandpasses. Solutions and dispersions were placed in a 1 cm optical path length quartz cuvettes. A thermostatic system with stirring (PTP-1 Fluorescence Peltier System with a PCB1500 Water Peltier System, Perkin-Elmer) was used to keep the dispersions in the cuvette at specific constant temperatures during photoluminescence measurements. A pHmeter model mPA 210 from Tecnocon (Brazil), with a glass membrane electrode combined with a reference Ag/AgCl_(KCl sat) was employed. Absorption spectra in the UV-visible range were acquired on a Varian (USA) double beam spectrophotometer model Cary 100, using 600 nm min⁻¹ scan rate, 10 nm spectral bandpass, in the range of 800 to 200 nm and aqueous solutions/dispersions were placed on 1 cm optical path length quartz cuvettes. Fourier transform infrared (FTIR) spectra were obtained on a Perkin-Elmer Spectrum Two spectrophotometer coupled with a universal attenuated total reflectance (ATR) accessory in the range of 4000 to 400 cm⁻¹ and accumulation of 10 scans. Elemental analyses (CNHS) were performed on a Flash EA elemental analyzer, model 1112 (Thermo Electron Corporation, USA). The amounts of C, H, N and S in the complex [Eu(tta)₄](Et₃NH⁺) were obtained under He atmosphere (140 mL min⁻¹) using a thermal conductivity detector, oven temperature at 900 °C, column temperature of 60°C and tin capsules were used to introduce samples. The thermogravimetric decomposition curve of [Eu(tta)₄](Et₃NH⁺) was obtained in a thermal analyzer model TGA-60 (Shimadzu, Japan) with an initial sample mass of approximately 5 mg. The sample was heated in a temperature range between 25 and 500 °C in an aluminum oxide crucible at a rate of 10 °C min⁻¹ under a dynamic atmosphere of N₂ at 20 mL min⁻¹. The comparative measurements of mercury/methylmercury were made on a multipass

mercury-dedicated cold vapor atomic absorption spectrometer (multipass-CV-AAS) model RA-915 (LUMEX, Russia), equipped with Zeeman background correction and connected to a RP-92 chemical reduction accessory for aqueous solutions. The photochemical reactor used to evaluate the degradation of samples upon exposition of either UV radiation or visible light was built in LEEA-PUC-Rio (Figure 3.1) and consists of six mercury vapor lamps (6 W each) or six UV lamps (main line at 365 nm) of 6 W each. Each lamp was supported by a 9 W lamp reactor (ECP, Brazil) placed at the bottom of the structure, along with a 3010 RPM notebook fan (Nylon, China). The lamps were placed on the inside of a PVC tube section, 0.22 m in internal diameter, 0.30 m wide, which served as the reactor housing. The set up was made so that two, four or six lamps could be activated independently according to the experiment to be carried out. Quartz tubes were used to place the solution inside the reactor and the airflow, established by the notebook fan, kept the solutions at temperature close to 25 °C. X-ray diffraction measurements were made on a D8 Venture diffractometer (Bruker, Germany) at room temperature and using Mo-K α radiation. Nanoparticle images were obtained with a field emission scanning electron microscope model JSM-7800F (JEOL, Japan), operated in the scanning transmission electron microscopy (STEM) mode at 30 kV. Dynamic light scattering (DLS) and ζ -potential measurements were performed using a SZ-100 Nanopartica series (Horiba, Japan), equipped with a 10 mW laser at 532 nm. The ζ -potential measurements were made using an acrylic electrochemical cell containing a flat carbon electrode (6 mm thickness) and DLS measurements were obtained using a polystyrene cuvette with four optically clear sides and pathlength of 1.0 cm. Total carbon measurements were made on a carbon analyzer model TOC-VCPN (Shimadzu, Japan). X-ray photoelectron spectroscopy (XPS) experiments were made under ultrahigh vacuum ($\sim 10^{-9}$ mbar) using a surface analysis chamber, equipped with a VG Thermo Alpha 110 hemispherical analyzer, and using non-monochromatized Al-K α line as X-ray excitation source. Chromatographic analyses were performed on a high-performance liquid chromatographic system (1200 series, Agilent, USA) equipped with a G1315C model diode array absorption photometric detector. Chromatographic column model Eclipse XDB-C18 (250 \times 4.6 mm length, 5 μ m average particle size) from Agilent was used. A heating plate (IKA, Germany), with magnetic stirring capability, was used for temperature and homogenization control in performing

extraction. For cell growth, an incubator (Qualxtron, Brazil) without shaker and an incubator (TE-421, TECNAL, Brazil) with shaking capability were used.

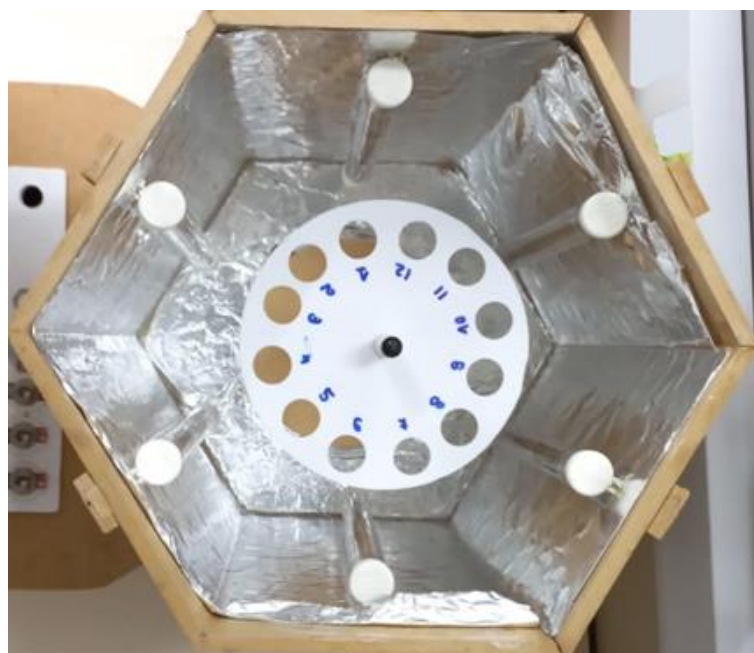


Figure 3.1 - Photochemical reactor built in LEEA-PUC-Rio.

3.2. Reagents and materials

Ultrapure water (18.2 MΩ cm) was obtained from the Milli-Q gradient A10 ultra-purifier (Millipore, USA). Citric acid, urea, sodium citrate, silver nitrate, copper sulfate (pentahydrate), boric acid, sodium hydroxide, absolute ethanol, Triton X-100, sodium oxalate, potassium permanganate, acetonitrile (HPLC grade), 2,4-dinitrophenylhydrazine (DNPH), chromotropic acid, polyvinyl alcohol (PVA), polymethyl methacrylate (PMMA) and, polycaprolactone (PCL) were purchased from Merck (Germany). Formaline (Formaldehyde aqueous solution at 36.5–38.0 % w/v), ammonium hydroxide, acetone, ethanol 95 %, tert-butyl alcohol, chloroform, dichloromethane, hydrogen peroxide 30 % v/v, hydrochloric acid, acetic acid, sulfuric acid, phosphoric acid and nitric acid were from Vetec (Brazil). Whatman® quantitative filter paper grade 41, europium oxide, 2-thenoyltrifluoroacetone, triethylamine and methylmercury chloride were from Sigma Aldrich (USA). Quinine sulfate were purchased from Fluka (Germany). Peptone, glucose and yeast extract were from Isofar (Brazil). Standard solutions (at

1000 mg L⁻¹) of metal ions (Mn²⁺, Ca²⁺, Li⁺, Mg²⁺, Al³⁺, Sn²⁺, Hg²⁺, K⁺, Ni²⁺, Na⁺, Zn²⁺, Co²⁺, Cr³⁺, Cd²⁺, Pb²⁺, Ba²⁺ and Cu²⁺) were from Merck. Milk samples, different brands, were purchased in local supermarkets in the city of Rio de Janeiro, Brazil. Commercial baking yeast was also locally purchased. Filters and syringe filters (45 µm) were from (Sigma Aldrich, USA). A 25 µL manual chromatography syringe (Hamilton, USA) was used for headspace single-drop microextraction (HS-SDME). Crude oil, used to simulate the PW samples, were obtained from Petrobras (the Brazilian Energy Company) and they were previously tested to ensure no detectable quantities of CH₃Hg⁺.

3.3. Procedures concerning the lanthanide complex

3.3.1. Preliminary studies for the choice of the lanthanide complex

At the beginning of this work, the lanthanide complexes presented in Table 3.1 were available. In order to select the complex that would be used as analytical probe, stability tests of the photoluminescent emission of these complexes in solutions were made before and after exposure to visible and UV radiation using the photochemical reactor. Aliquots of these exposed solutions were transferred to quartz cuvettes to obtain spectrum and measure its intensity (peak intensity).

Table 3.1 – Available lanthanide complexes.

Lanthanide complex
[Eu(tta) ₃ Phen]
[Tm(DBM) ₃ Phen]
[Eu(DBM) ₃ (TPPO) ₂]
[Eu(tta) ₄](Et ₃ NH ⁺)
[Tb(sal) ₃ (H ₂ O) _x]
[Tb(acac) ₃ Phen]

3.3.2.

Synthesis of $[\text{Eu}(\text{tta})_4](\text{Et}_3\text{NH}^+)$ by a new synthetic route

A simpler synthetic route, compared to the one previously reported in literature [181], was developed to produce the Eu(III) β -diketonate complex or $[\text{Eu}(\text{tta})_4](\text{Et}_3\text{NH}^+)$. It was prepared by adding, dropwise, 5.6 mL of triethylamine (Et_3N ; 0.04 mol) to a mixture of 8.88 g of 2-thenoyltrifluoroacetone (Htta ; 0.04 mol) and 200 mL of acetone. The reaction mixture was maintained under magnetic stirring for 30 min before adding, in small aliquots and under vigorous stirring, a solution of $\text{EuCl}_3 \cdot 6\text{H}_2\text{O}$ (3.66 g or 0.01 mol in 100 mL of acetone). $\text{EuCl}_3 \cdot 6\text{H}_2\text{O}$ was prepared by dissolving proper amounts of europium oxide in hydrochloric acid. After 2 h, the mixture was heated to 60 °C in order to evaporate the organic solvent, allowing precipitation of a reddish-orange powder. The precipitate was filtered, recrystallized with acetone, then dried and stored under reduced pressure in a desiccator.

3.3.3.

Characterization of $[\text{Eu}(\text{tta})_4](\text{Et}_3\text{NH}^+)$

$[\text{Eu}(\text{tta})_4](\text{Et}_3\text{NH}^+)$ was characterized using different techniques. Elemental analysis (CHNS) was performed with $[\text{Eu}(\text{tta})_4](\text{Et}_3\text{NH}^+)$ solid. Analysis was made using methionine (9.39 % N; 40.25 % C; 7.43 % H; 21.49 % S) as a verification standard. The calibration of the equipment was performed using the standards 2,5-Bis(5-tert-butyl-2-benzoxazolyl)tiophene (BBTO) (6.51 % N; 75.52 % C; 6.09 % H; 7.44 % S), sulfanilamide (16.26 % N; 41.85 % C; 4.68 % H; 18.62 % S), cystine (11.66 % N; 29.99 % C; 13.43 % H; 3.42 % S) and a standard lubricating oil (1.29 % N; 81.00 % C; 13.43 % H; 3.42 % S). For FTIR analysis, the $[\text{Eu}(\text{tta})_4](\text{Et}_3\text{NH}^+)$ solid sample, without any further preparation, was placed in the equipment and, with the aid of the ATR accessory, the infrared spectrum was obtained. Thermogravimetric analysis was made by placing the solid sample in the aluminum oxide crucible that was then placed in the instrument and measurement was made obtaining the decomposition curve. Photoluminescence analysis ($\lambda_{\text{em}} / \lambda_{\text{exc}} = 393 / 616$ nm) of the solid was made by placing the sample in the powder sample holder, that was then secured with a quartz window and placed in the front surface accessory of the spectrofluorometer for measurements. Photoluminescence analysis

($\lambda_{em}/\lambda_{exc} = 343 / 616$ nm) and absorption spectrophotometric analysis (UV-vis) of the complex in solution were made by placing about 3 mL of a 5.0×10^{-6} mol L⁻¹ solution in the quartz cuvette to perform measurements. Blank measurements were made using only the solvent. Crystals of [Eu(tta)₄](Et₃NH⁺) complex were obtained by dissolving the powder in warm ethanol followed by slow evaporation of the solvent at room temperature for approximately two months. For XRD analysis, single crystals were cut from poly crystals and fixed to the sample holder that was then placed in the equipment for measurements.

3.3.4. Solubility tests of [Eu(tta)₄](Et₃NH⁺)

In order to identify the best solvent for the complex [Eu(tta)₄](Et₃NH⁺) a solubility test was performed. A small amount of the solid compound (approximately 5.0 mg) was placed in 10 mL beakers where small volumes of a different solvents were added (acetone, ethanol, methanol, chloroform, hexane and tetrahydrofuran). The test best solvent was the one that readily dissolved the complex.

3.3.5. Photoluminescence stability test of [Eu(tta)₄](Et₃NH⁺) in solution or after dried on a solid substrate

Aiming to verify the photoluminescence stability of the [Eu(tta)₄](Et₃NH⁺) complex in solution, a test was made with concentration 5.0×10^{-6} mol L⁻¹ in a mixture of solvents containing 70 % of acetone and 30 % water, in volume. The transition ⁵D₀ → ⁷F₂ (616 nm) was monitored over 3 h, performing measurements every 15 min in the first hour, then measuring every 30 min up to the end of the experiment. For the purpose of this test, the solution was exposed only to ambient light. A second test was made where the solution was kept protected from light and measurements were made every hour for 5 h.

Regarding UV radiation, it is not possible to protect the [Eu(tta)₄](Et₃NH⁺) solution from this radiation during photoluminescence measurements because the solution is excited in the ultraviolet region, therefore a kinetic study was carried out to calculate the decay rate of the photoluminescent emission signal of the [Eu(tta)₄](Et₃NH⁺) solution. Photoluminescent emission intensity in the transition

$^5D_0 \rightarrow ^7F_2$ was continuously recorded for a period of time of 6 min with excitation at 343 nm and then plotting emission intensity against time in order to calculate the decay rate of the photoluminescence of $[\text{Eu}(\text{tta})_4](\text{Et}_3\text{NH}^+)$ in solution.

In order to test the photoluminescence stability of the $[\text{Eu}(\text{tta})_4](\text{Et}_3\text{NH}^+)$ complex in solid state onto a substrate, a circle of Whatman® quantitative filter paper grade 41 (17 mm in diameter) was used. Into the center of the paper circle, 10 μL of $[\text{Eu}(\text{tta})_4](\text{Et}_3\text{NH}^+)$ 1.0×10^{-4} mol L^{-1} (1 nmol) solution was added and, after solvent evaporation (approximately 30 s), the paper circle, manipulated with tweezers, was placed in the solid sample holder that was then inserted in the front surface accessory of the spectrofluorometer. Photoluminescence measurements were made every 5, min in a time interval of 60 min.

3.3.6. Oxygen (O_2) influence test

In order to verify the influence of the atmosphere oxygen on the photoluminescence stability of $[\text{Eu}(\text{tta})_4](\text{Et}_3\text{NH}^+)$ complex on paper substrate, tests were carried out with and without q quartz window, placed to protect the paper substrate, containing the complex, from the air. A circle of filter paper containing 0.1 nmol of $[\text{Eu}(\text{tta})_4](\text{Et}_3\text{NH}^+)$ was used in this study. The paper previously embedded with the sample was placed in the solid sample holder with the quartz window protecting the complex from the influence of O_2 in the air and photoluminescent measurements were made within a 60-min time interval, where measurements were performed every 5 min.

3.3.7. Choice of acetone/water ratio

As mercury is soluble in water and insoluble in acetone (the probe solvent), it became necessary to make a mixture of these two solvents to prepare the solutions of $[\text{Eu}(\text{tta})_4](\text{Et}_3\text{NH}^+)$ and only then the mercury solution was added to the medium. In this way, the photoluminescence stability study of the $[\text{Eu}(\text{tta})_4](\text{Et}_3\text{NH}^+)$ complex with different proportions of water in acetone was made. Three solutions of the $[\text{Eu}(\text{tta})_4](\text{Et}_3\text{NH}^+)$ complex with concentration of 5.0×10^{-6} mol L^{-1} have been prepared. The proportions of acetone/water were 50/50 % v/v, 70/30 % v/v

and 80/20 % v/v were used. The photoluminescence of these three solutions was verified for 72 h, being the first measurement made immediately after the preparation of the solutions and the other measurements made every 24 h.

3.3.8.

Preparation of working solutions

3.3.8.1.

Preparation of [Eu(tta)₄](Et₃NH⁺) solutions

The [Eu(tta)₄](Et₃NH⁺) standard stock solution (at 1.0×10^{-3} mol L⁻¹) was prepared by dissolving the complex salt (0.0057 g) in 5.0 mL of an acetone/water (70/30 % v/v) mixture. This standard stock solution was used to prepare working solution (analytical probes) at 5.0×10^{-6} mol L⁻¹. Solutions were left to rest at room temperature, protected from ambient light, for 1 h before use.

3.3.8.2.

Preparation of mercurial solutions

Methylmercury chloride standard stock solution, at 1000 mg L⁻¹, was prepared by dissolving 0.01 g of the salt (about 4.0×10^{-5} mol) in the smallest amount of methanol as possible before the volume was completed to 10.00 mL with acidified ultrapure water (HCl 0.2 % and CH₃COOH 0.5 %). This standard stock solution was used to prepare working solutions at concentrations varying from 0.1 to 2.0 µg mL⁻¹. The solutions were stored in glass flasks under 4 °C refrigeration.

Mercury chloride solution (Hg²⁺) was prepared by dilution of a standard stock solution at concentration of 1000 mg L⁻¹. This solution was used to prepare solutions from 0.1 to 2.0 mg L⁻¹.

3.3.9.

Tests of pH influence

The effect of the hydrogenionic concentration on the photoluminescence stability of the [Eu(tta)₄](Et₃NH⁺) complex solution was made using 0.01 mol L⁻¹ solutions of both NaOH and HNO₃ to acidify or basify the solution, respectively. To 10 mL aliquots of the [Eu(tta)₄](Et₃NH⁺) 5.0×10^{-6} mol L⁻¹ solution, NaOH or HNO₃ solutions have been added to vary the measured pH of the resultant solution.

The pH of these aliquots ranged from 3.0 to 9.0 and was verified using a pHmeter before photoluminescence measurements were made. Measurements with an original complex solution without pH adjustment was also made for comparison.

3.3.10. Tests of temperature influence

The effect of temperature on the photoluminescence of the $[\text{Eu}(\text{tta})_4](\text{Et}_3\text{NH}^+)$ work solution was made using the thermostatic system and varying the solution temperature in the range from 20 to 30 °C (with temperature interval of 2 °C). After adjusting each temperature, a 5 min equilibrium time was established before photoluminescence was measured.

3.3.11. Tests of mercury influence

In order to verify the effect of mercury species on the $[\text{Eu}(\text{tta})_4](\text{Et}_3\text{NH}^+)$ solution, tests were carried out using additions of organic and inorganic mercury solutions to the probe. Solutions of the Eu(III) complex used as analytical probes were prepared by placing 4.50 mL of the $[\text{Eu}(\text{tta})_4](\text{Et}_3\text{NH}^+)$ working solution into a 5.00 mL volumetric flask. Then, appropriate volumes of CH_3Hg^+ standard solution were added before adjusting the final volume with acetone/water (70/30 % v/v) solution leading to final complex concentration of $5.0 \times 10^{-6} \text{ mol L}^{-1}$. The experiment was repeated using Hg^{2+} working solutions.

3.3.12. Tests of different metal ions influence

The evaluation of the influence of the presence of other metal ions nearby the probe, $[\text{Eu}(\text{tta})_4](\text{Et}_3\text{NH}^+)$, was made and compared to the effect imposed by CH_3Hg^+ and Hg^{2+} on the measured photoluminescence. The analysis procedure was the same as the mercury tests: 4.50 mL of $[\text{Eu}(\text{tta})_4](\text{Et}_3\text{NH}^+)$ working solution were transferred to 5.0 mL volumetric flasks and appropriate volumes of Fe^{3+} , Mn^{2+} , Ca^{2+} , Li^+ , Mg^{2+} , Al^{3+} , Sn^{2+} , K^+ , Cr^{3+} , Ni^{2+} , Cd^{2+} , Na^+ , Pb^{2+} , Zn^{2+} , Ba^{2+} , Cu^{2+} or Co^{2+} solutions were added to the flasks with final concentration of $200 \mu\text{g L}^{-1}$, before adjusting the final volume to 5.00 mL with acetone/water 70/30 % v/v. Blank

solutions had their final volume adjusted only with acetone/water 70/30 % v/v. This test was repeated using different concentrations for the ions.

3.3.13.

Extraction and preconcentration of CH_3Hg^+

The extraction and pre-concentration of CH_3Hg^+ was carried out in three control water samples and three simulated PW samples. The natural water and the PW samples were fortified with both Hg^{2+} and CH_3Hg^+ at equal concentrations in three levels: 15, 30 e 45 ng L^{-1} . PW samples (labeled PW1, PW2 and PW3 according to the increasing in analyte concentrations) were simulated by dispersing 20 mg L^{-1} of crude oil and dissolving 20 g L^{-1} of NaCl. The extraction and pre-concentration of the analyte from samples were performed based on a procedure adapted from literature [182], where dichloromethane was used as the extraction solvent instead of benzene. Based on availability and evaporation capacity, dichloromethane was chosen as the extract solvent. Briefly, 50.00 mL of sample was transferred to a separation funnel (125 mL capacity) along with 4 mL of concentrated HCl. An aliquot of 5.0 mL of dichloromethane was added followed by a vigorous mechanical agitation (10 min). After resting, to allow phase separation, the organic phase was collected. The remainder aqueous phase was subjected to two more extractions with 5.0 mL of dichloromethane (three extractions in total). The collected organic phases were mixed and transferred to a 25 mL separation funnel along with 5 mL of aqueous solution containing L-cysteine (1 % w/v) prepared in sodium acetate (0.8 % w/v). After vigorous agitation (10 min) and separation of phases, the organic phase was collected in a glass vial (20 mL capacity) and capped. The remaining aqueous phase was mixed with 0.8 mL of HCl and 1 mL of dichloromethane and subjected to agitation (10 min). The organic phase was collected and combined with the one previously collected. Then, 1 mL of ultrapure water was added and forced mixed with the organic phase of each sample. After phase separation, the organic phase, at the top of the vial, was gently evaporated to obtain the CH_3Hg^+ incorporated into the aqueous phase.

3.3.14.**Tests with preconcentrated CH₃Hg⁺ samples in water and PW**

To test the influence of the water and PW samples containing preconcentrated CH₃Hg⁺ ions in the photoluminescence emission of the [Eu(tta)₄](Et₃NH⁺) probe, tests were carried out using additions of these samples to the probe solution.

For tests with samples, 500 μL of the aqueous samples were added to 3.0 mL of acetone followed by the addition of 500 μL of the [Eu(tta)₄](Et₃NH⁺) solution (5.0×10^{-5} mol L⁻¹), then adjusting final volume with ultrapure water in order to obtain the final acetone/water 70/30 % v/v proportion and final concentration of the complex at 5.0×10^{-6} mol L⁻¹. Blank solutions were the [Eu(tta)₄](Et₃NH⁺) solution (5.0×10^{-6} mol L⁻¹) in acetone/water (70/30 % v/v) only.

3.3.15.**Photoluminescent measurements of [Eu(tta)₄](Et₃NH⁺)**

Photoluminescence scanning was made using 1000 nm min⁻¹ scan rate. Steady state quantitative measurements with excitation at 343 nm and measuring luminescence at the characteristic Eu(III) peak at 616 nm. Photoluminescence measured from probe solutions containing CH₃Hg⁺ (I) were normalized by the blank signal (I₀) in order to establish an increasing relationship between normalized signal (I₀/I) and the concentration of CH₃Hg⁺, with K_s (the quenching constant) as the sensitivity (Eq. 3.1).

$$I_0/I = 1 + K_s [\text{CH}_3\text{Hg}^+] \quad (\text{Eq. 3.1})$$

3.3.16.**Quantitative determination of mercury in water and in PW samples by Multipass-CV-AAS**

Reference analytical results were obtained by performing analyses with CV-AAS method, using a multipass cell [117]. The determination of mercury (both inorganic mercury and total mercury comprising Hg²⁺ and CH₃Hg⁺) was made adding 1.0 mL of ultrapure water into the vial containing the extracted material from samples in dichloromethane. The organic solvent was gently evaporated

(under argon flow) until about 1.0 mL of the solution (the aqueous part) remained. This solution was diluted with ultrapure water in order to obtain a final volume of 10 mL and then placed into the CV–AAS spectrometer bubbler, which contained 3 mL of SnCl_2 (20 % w/v) to allow the fast reduction of Hg^{2+} and transfer of the formed Hg^0 to the multipass CV-AAS spectrometer cell (operating in continuous acquisition mode). When determining total mercury (in order to proceed the indirect determination of CH_3Hg^+ by difference), the volume, of about 1.0 mL, remaining after dichloromethane evaporation was transferred to a 10 mL volumetric flask followed by the dropwise addition of a H_2SO_4 0.1 mol L^{-1} solution (until pH 3) and H_2O_2 30 % v/v (to get final concentration of 1 %). Then, the final volume was adjusted with water and the resulting solution was placed in a 15 mL quartz tube, capped and then exposed to UV radiation for 15 min. Then the solution was transferred to the glass reaction cell to perform the reduction (using SnCl_2) of both the original Hg^{2+} and the photo-produced Hg^2 into detectable Hg^0 vapor. Prior to use, all of the reagent solutions were placed into washing bottles and purged with a flow of argon and the remaining trace levels of mercury in solutions were determined to be accounted in the final calculations.

3.4.

Procedures concerning N-doped graphene quantum dots

3.4.1.

Preliminary studies for the production of N-GQDs and the interaction with formaldehyde

In the preliminary studies, the aim was the development of nanoparticles by different routes to find a type that is stable and sensitive towards formaldehyde.

3.4.1.1.

Preparation of N-GQDs by pyrolysis and tests with formaldehyde

The preparation was carried out according to the procedure previously described [183] that is currently used at LEEA-PUC-Rio with minor modifications and variation of precursors used as doping agents. In summary, a mix of 0.5 g (2.4 mmol) of citric acid and 0.15 g (2.5 mmol) of urea was transferred to a beaker and heated to 270 °C with the help of a heating plate. After the melting of the reagents

(with color change from colorless to yellow to brown) within a period of approximately 2 min, the content was added to 10 mL of ultrapure water at room temperature and kept under magnetic stirring for 20 min for the phase of hydroexfoliation. The resulting dispersion was then stored in a glass flask properly closed. To monitor the photoluminescent stability of the nanoparticles, the intensity of their emission signal was recorded over time using the excitation/emission pair of 324/431 nm.

Tests to verify the interaction of nanoparticles with formaldehyde were performed as follow: a) in solution, increasing volumes (10 to 100 μL) of different formaldehyde solutions 1.5 to 385 g L^{-1} (0.15 to 38.5 % w/v) were added to the cuvette containing 3.0 mL of N-GQDs dispersion and the photoluminescence measurements were made at 324/431 nm. The resulting spectra were corrected by the dilution factor; b) in vapor, in one Petri dish, a drop of N-GQDs dispersion used as control was placed and the dish was then sealed. In another Petri dish, a drop of N-GQDs dispersion was placed and then a drop containing formaldehyde 38.5 % w/v was placed 2 centimeters away from the GQDs drop and the dish was sealed. Then, both dishes were placed in a heating oven at 37°C to accelerate formaldehyde evaporation and interaction with N-GQDs. After 15 min, the drops of N-GQDs were collected, with the help of a micropipette, and dispersed in a cuvette containing 3.0 mL of ultrapure water and photoluminescence measurements were made at 324/431 nm; c) in headspace single drop micro-extraction (HS-SDME), 1.00 mL of formaldehyde solutions in different concentrations (1.5 to 380 g L^{-1} w/v) were placed in a 5.0 mL vials that were sealed. The vial was placed in a heating plate and the solution was kept under magnetic stirring and temperature of 30°C. Then, a micro-syringe containing 5 μL of the concentrated N-GQDs dispersion was inserted through the seal and placed above the formaldehyde solution. A drop was formed in the tip of the micro-syringe and exposed to the headspace for 5 min. After this period of time, the drop was retracted back into the micro-syringe and then dispersed in 3.0 mL of water in a cuvette and photoluminescent measurements were made at 324/431 nm.

3.4.1.2.

Preparation of N-GQDs with Ag or Cu by pyrolysis and tests with formaldehyde

The N-GQDs dispersions were also prepared by using Ag and Cu as modifying agents. Tollen's reagent was prepared by dissolving appropriate amount of silver nitrate in ammonia solution (pH 9.0) [165] and Benedict's reagent was prepared by dissolving appropriate amounts of sodium citrate and copper sulfate pentahydrate in a sodium carbonate solution [165]. The procedure for the production of N-GQDs doped with Ag or Cu is similar to the one previously described, with the pyrolysis of citric acid and urea, then poring the molten mixtures into aqueous solutions, at room temperature, of Tollen's reagent ($1.0 \times 10^{-3} \text{ mol L}^{-1}$), for the incorporation of silver ions in the structure of N-GQDs, or Benedict's reagent ($1.0 \times 10^{-2} \text{ mol L}^{-1}$), for the incorporation of copper ions in the structure of N-GQDs. The resulting materials were kept under magnetic stirring, for 20 min, and then stored inside glass flasks. The photoluminescent stability of the dispersion modified with silver was monitored over time at 348/434 nm and the photoluminescent stability of the dispersion modified with copper was monitored at 360/431 nm. Tests with formaldehyde solutions were carried out with by adding a fixed volume of 30 μL of different concentrations of formaldehyde solutions (1.5 to 380 g L^{-1}) to the cuvette containing 3 mL of the N-GQDs dispersions modified with silver or copper and the photoluminescence measurements were made in the corresponding excitation/emission pair.

3.4.1.3.

Preparation of silver-modified N-GQDs by a hydrothermal route

The N-GQDs-Ag were produced through a hydrothermal refluxing based on the procedure described in the literature [163] with modifications. Typically, 0.84 g (4 mmol) of citric acid, 0.48 g (8 mmol) of urea (with final citric acid:urea ratio of 1:2) and 200 μL of the Tollen's reagent (at $1.0 \times 10^{-1} \text{ mol L}^{-1}$) were mixed in 20 mL of water in a round-bottom flask that was adjusted in a condensation system. The flask was placed into a heating mantle and heated to 180 $^{\circ}\text{C}$ during 8 h. Then, the resultant aqueous dispersion (called stock N-GQDs-Ag dispersion) was let to cool to room-temperature and stored away from light. N-GQDs-Ag were also

prepared with different urea proportions obtaining citric acid:urea ratios of 1:1, 1:3 and 1:4. Photoluminescent stability of these dispersions was monitored at excitation/emission wavelength of 349/441 nm over time and tests with formaldehyde vapor in different concentrations (1.0×10^{-3} to 1.0×10^{-1} g L⁻¹) were carried out using the HS-SDME.

3.4.2. Characterization procedures for N-GQDs-Ag

For the characterization of N-GQDs-Ag dispersion (citric acid:urea ratio of 1:2), different techniques were applied. UV-Vis and photoluminescent spectra were obtained by placing 3.0 mL of the diluted dispersion (1000 dilution factor) in proper quartz cuvettes and measurements were made. For DLS analysis, samples with and without UV radiation exposure were used for DLS measurements. 2.5 mL of the samples were placed in a polystyrene cuvette and measurements were made after 24h and 120h after the preparation of nanoparticles. For ζ -potential analysis, samples with pH variation from 3.0 to 10.0 were placed in an acrylic electrochemical cell and measurements were made. For TOC analysis, 10.0 mL of a 1000x diluted dispersion were used for each measurement. STEM analysis was made by placing a few microliters of the stock dispersion in carbon grids and, after the samples were dried at room temperature, measurements were made.

Dried samples of N-GQDs-Ag were obtained through addition of excess ethanol and subsequent evaporation where a gel was the final product of evaporation and were used for FTIR and XPS measurements. For FTIR analysis, the dried samples were placed in the FTIR instrument and, with the help of the ATR accessory, measurements were made. For XPS analysis, dried samples were placed in the instrument with no further preparation and measurements were made.

Photoluminescence quantum yield measurement of N-GQDs-Ag was made by using the comparative method [184], where the Φ value was obtained by comparing the photoluminescent intensity of NGQDs to a reference material. For this experiment, five standard solutions of the reference material quinine sulfate at different concentrations were prepared in sulfuric acid (0.5 mol L⁻¹) while another five different dispersions of N-GQDs-Ag were prepared by diluting the original dispersion in ultrapure water. Absorbance values of both samples (quinine sulfate

and N-GQDs-Ag) were determined using the spectrophotometer at the excitation wavelength of 347 nm. Absorbance values were between 0.01 and 0.1 to avoid auto-absorption effects that can skew the results for quantum yield [185]. Photoluminescence emission spectra were recorded by exciting both samples at 347 nm and the integrated photoluminescence intensities were calculated. These results were used to plot calibration curves of integrated fluorescence intensity against absorbance of the N-GQDs-Ag and quinine sulfate samples. The slopes of both curves were calculated and were used to obtain the Φ of N-GQDs-Ag by using Equation 3.2:

$$Q_s = Q_r \left(\frac{m_s}{m_r}\right) \left(\frac{\eta_s}{\eta_r}\right)^2 \quad (\text{Eq. 3.2})$$

Where Q, m and η refer, respectively, to fluorescent quantum yield, gradient of the plot integrated fluorescent intensity against absorbance and refractive index of solvents. The subscripts s and r refer to sample and reference material, respectively. In this experiment, water, which has $\eta = 1.33$, was the solvent for both N-GQDs-Ag dispersions and quinine sulfate solutions, thus the value of $(\eta_s/\eta_r)^2$ is 1. Q_r value is 0.546 and was obtained from the literature [186].

3.4.3.

Preparation of standard solutions, sample solutions and working solutions

When the stock dispersion could not be used without dilution, working dispersions of N-GQDs-Ag were prepared by diluting the standard stock dispersion in ultrapure water (1000 dilution factor) in a volumetric flask.

Stock nanoparticle dispersions were, in general, previously diluted with water before some of the characterizations and before using them as analytical probe. Formaldehyde diluted solutions (down to 1.5 g L^{-1} and even down to $1.0 \times 10^{-3} \text{ g L}^{-1}$) were prepared by diluting (sequential dilutions when necessary) appropriate amounts of commercial formaldehyde 36.5-38.0 % w/v in water. Before dilutions, the actual formaldehyde concentration (typically 38.5 % w/v, equivalent concentration of 385 g L^{-1}) was verified by titration, using 100.00 mL of solutions containing 4.0 g of the commercial formaldehyde solution diluted in Na_2SO_3 (1.00

mol L⁻¹). Titrations (three replicates) were made using H₂SO₄ 1.00 mol L⁻¹ and thymolphthalein as indicator.

Milk samples were fortified with formaldehyde to simulate adulterations. This was made by adding formaldehyde to the milk sample (previously diluted when necessary) in order to reach final concentration from 1.0×10^{-3} to 1.0×10^{-1} g L⁻¹. Milk samples were not submitted to any specific treatment but dilution with water: 2-fold dilution was used for whole milk and 0 % lactose whole milk while 1-fold dilution was used for semi-skimmed milk. Skimmed milk was not diluted previous to analysis.

3.4.4. pH influence

To test the effect of the hydrogenionic concentration on the photoluminescence stability of the N-GQDs-Ag dispersion, a study was made where the pH of a diluted dispersion of N-GQDs-Ag (1000 dilution factor) was varied from 3.0 to 10.0 using NaOH or HNO₃ to acidify or basify the dispersion, respectively, by increasing or decreasing its pH. The pH variation was verified with the pH meter and then photoluminescent measurements were made. Measurements with a dispersion without pH change was also made for comparison.

3.4.5. Study of temperature influence

To test the influence of temperature on the photoluminescence stability of the N-GQDs-Ag working dispersion, a study was made where the thermostatic system was used to vary the dispersion temperature in the range of 20 to 40 °C (with temperature interval of 2, 2.5 or 5 °C). After each temperature variation, and after 5 min of equilibrium time, photoluminescence was measured.

3.4.6. Influence of UV radiation

Regarding the effect of UV radiation on the photo-bleaching of the N-GQDs-Ag, a kinetic study was carried out to calculate the decay rate of the photoluminescent emission signal of the N-GQDs-Ag dispersion.

Photoluminescent emission was constantly measured by a time interval of 5 min with excitation at 349 nm in order to estimate the rate of degradation.

3.4.7.

Analysis of formaldehyde using headspace single drop microextraction (HS-SDME)

HS-SDME was performed using a 25 μL manual chromatography syringe and a heating plate with magnetic stirring capability for temperature and homogenization control. The procedure for the determination of formaldehyde using HS-SDME was based on literature description for metals in the form of hydrides [187-188]. Briefly, 1.00 mL of the aqueous formaldehyde solutions (from 1.0×10^{-3} to 1.0 g L^{-1}) or milk samples fortified with formaldehyde (with final concentration of formaldehyde from 1.0×10^{-3} to 1.0 g L^{-1}) was placed in a 5.0 mL vial that was then sealed with a rubber septum. Then, the vial was placed in a heating plate, at $25 \text{ }^\circ\text{C}$ (monitored with a thermocouple temperature meter) and kept under magnetic stirring. The needle of a microsyringe, containing 5 μL of the concentrated aqueous dispersion of N-GQDs-Ag, was inserted through the rubber septum and adjusted right above the surface of the solution. A drop of the N-GQDs-Ag dispersion was created at the tip of the syringe using the whole content in it (5 μL of the dispersion) and exposed to the headspace of the flask during 5 min while the samples were kept under gentle stirring. Then, the drop was retracted back into the microsyringe to be further inserted in a quartz cuvette containing 3.0 mL of water. After stirring for homogenization (30 s), photoluminescence was measured. A blank comprised of N-GQDs-Ag dispersion was made without exposure to the sampling head-space.

3.4.8.

Tests of hydrogen peroxide (H_2O_2) interference

The effect of the presence of H_2O_2 in sample was evaluated. First, a study was conducted to evaluate the influence of H_2O_2 on the photoluminescent emission of the N-GQDs-Ag dispersion. For this, samples of whole milk were prepared with fortification of H_2O_2 at different concentrations. The concentration of the H_2O_2 solution used to fortify the milk samples was previously verified through titration in triplicate of H_2O_2 solution acidified with H_2SO_4 using KMnO_4 0.02 mol L^{-1}

solution (standardized with $\text{Na}_2\text{C}_2\text{O}_4$) as titrant and indicator. A concentration value of 6.77 % was obtained. Then, the HS-SDME procedure was repeated for milk samples fortified with H_2O_2 and photoluminescent measurements were made. Next, the effect of H_2O_2 on the photoluminescent emission of the N-GQDs-Ag dispersion in the presence of formaldehyde was evaluated. Whole milk samples were fortified with H_2O_2 and formaldehyde, simultaneously, in different concentrations and the HS-SDME procedure was conducted and photoluminescent measurements were made.

3.4.9. Photoluminescence measurements

Steady-state intensity measurements (from aqueous formaldehyde standards or from samples) were made at excitation/emission wavelengths of 349/441 nm taking into consideration emission spectrum peak height. Photoluminescence signals measured from diluted N-GQDs-Ag dispersions that interacted with formaldehyde (I) were normalized in function of the respective blank signal (reference signal from the diluted N-GQDs-Ag dispersion without contact with formaldehyde - I_0). In this way, it was possible to establish an increasing relationship between normalized signal (I_0/I) and the concentration of formaldehyde, with K_s (quenching constant) as the sensitivity factor (Eq. 3.3).

$$I_0/I = 1 + K_s [\text{formaldehyde}] \quad (\text{Eq. 3.3})$$

3.4.10. Comparative colorimetric method for the determination of formaldehyde in milk samples

The comparative colorimetric study for the determination of formaldehyde in milk was made based on the AOAC official method 931.08 B [143], which is the method established by the Brazilian legislation [142]. Whole milk samples were fortified with 0, $1.0 \times 10^{-3} \text{ g L}^{-1}$, $1.0 \times 10^{-2} \text{ g L}^{-1}$, $1.0 \times 10^{-1} \text{ g L}^{-1}$ and 1.0 g L^{-1} of formaldehyde. For the test procedure, 100 mL of whole milk sample fortified with formaldehyde was diluted with 100 mL of water and acidified with 2 mL of concentrated phosphoric acid. The mixture was then gently distilled and about 50

mL of the distilled solution was collected. Then, 1 mL of the distilled solution was placed in a test tube containing 5 mL of 0.5 % (w/v) chromotropic acid solution prepared in sulfuric acid (72 % w/v) forming a final solution that had a slightly brown color. The test tube was then placed in a boiling water bath for 15 min and, after this period, the color was observed. The presence of formaldehyde was indicated by appearance of purple color (the higher the formaldehyde concentration, the deeper the purple color).

3.4.11.

Comparative chromatographic method for the determination of formaldehyde in milk samples

The comparative chromatographic method for the determination of formaldehyde in milk was based on the one reported by Rezende *et al.* [144], employing chemical derivatization with DNPH. Whole milk samples were fortified with $1.0 \times 10^{-3} \text{ g L}^{-1}$, $1.0 \times 10^{-2} \text{ g L}^{-1}$, $1.0 \times 10^{-1} \text{ g L}^{-1}$ and 1.0 g L^{-1} of formaldehyde. Aliquots of 2.5 mL of analyte fortified milk were placed in centrifuge tubes and pH was adjusted to about 4 by addition of 0.1 mol L^{-1} sulfuric acid solution. Then, 5.0 mL of 0.1 g L^{-1} DNPH solution (in acetonitrile) were added to the tubes, which were then vortex-mixed (1 min) and centrifuged (20 min) at 1000 RFC. The solutions were cooled overnight, at $-4 \text{ }^{\circ}\text{C}$, where the aqueous phases were frozen while the organic phases remained liquid. The organic phases were readily removed with an automatic micropipette, transferred to 5.00 mL volumetric flasks and the volume were reconstituted with acetonitrile. These solutions were filtered with $0.45 \text{ }\mu\text{m}$ syringe filters into HPLC vial flasks and measurements were made.

Formaldehyde-DNPH analytical curve was made with standard formaldehyde solutions (from 1.0×10^{-3} to $1.0 \times 10^{-1} \text{ g L}^{-1}$) prepared in 0.1 g L^{-1} DNPH solution in acetonitrile. These solutions were filtered with $0.45 \text{ }\mu\text{m}$ syringe filters into HPLC vial flasks.

Mobile phase consisted of acetonitrile (A) and ultrapure water (B) (filtered using $0.45 \text{ }\mu\text{m}$ membrane and degassed in ultrasonic bath) and gradient elution started with 65 % v/v of (A) for 6 min with a linear increase up to 90 % v/v until 8 min. The flow-rate was 1.0 mL min^{-1} , the column was kept at $30 \text{ }^{\circ}\text{C}$, the injection volume was $10 \text{ }\mu\text{L}$, the detection wavelength was 360 nm and the retention time for

the derived product was 4.6 min. Measurements were made in triplicate and peak areas were calculated.

3.5. Procedures concerning temperature sensing

3.5.1. Sensing of temperature using luminophore solutions

The potential of using luminophores $[\text{Eu}(\text{TTA})_4](\text{Et}_3\text{NH}^+)$, N-GQDs-Ag and LASOC 460 as temperature variation sensors was first studied in solution. For this, a $5.0 \times 10^{-6} \text{ mol L}^{-1}$ $[\text{Eu}(\text{TTA})_4](\text{Et}_3\text{NH}^+)$ solution (acetone/water 70 %/30 %), an N-GQDs-Ag dispersion with dilution factor of 1000, and a $5.0 \times 10^{-6} \text{ mol L}^{-1}$ LASOC 460 solution, in its aggregate form (ethanol/water 15 %/85 %), as well as a $5.0 \times 10^{-6} \text{ mol L}^{-1}$ LASOC 460 solution in tert-butyl alcohol were prepared.

The dependence of the photoluminescent emission of the solutions with temperature was evaluated in the range from 20 to 30 °C for $[\text{Eu}(\text{TTA})_4](\text{Et}_3\text{NH}^+)$ and 20 to 40 °C for N-GQDs-Ag and LASOC 460 with variations of 2 or 5 degrees. After each temperature variation, 5 min equilibrium time was allowed before photoluminescence was measured.

3.5.2. Sensing of temperature using luminophore polymeric matrices

The potential of the luminophores $[\text{Eu}(\text{TTA})_4](\text{Et}_3\text{NH}^+)$, N-GQDs-Ag and LASOC 460 as temperature variation sensors was also evaluated in polymeric matrices. For this, polymeric films containing the luminophores were prepared.

PCL films doped with $[\text{Eu}(\text{TTA})_4](\text{Et}_3\text{NH}^+)$ were prepared by solubilizing 0.1 g of PCL in 10 mL of chloroform in a 25 mL beaker under magnetic stirring at 60 °C. After complete solubilization of the polymer, a solution containing $1.0 \times 10^{-3} \text{ g}$ of $[\text{Eu}(\text{TTA})_4](\text{Et}_3\text{NH}^+)$, also in chloroform, was gently added to the solution containing the polymer, still under magnetic stirring at 60 °C. When the volume of the resulting solution was decreased to approximately 10 % of its initial volume, the magnetic bar was removed and the beaker was placed in an oven at 40 °C until complete evaporation of solvent and formation of the film.

PVA films doped with N-GQDs-Ag and PMMA films doped with LASOC 460 were prepared in a similar way but for the preparation of PVA-N-GQDs-Ag

films, water was used as solvent and 1 mL of N-GQDs-Ag stock dispersion was added to the polymer. For the preparation of PMMA-LASOC 460 films, acetone was used as solvent and 10 μL of a $5.0 \times 10^{-4} \text{ mol L}^{-1}$ LASOC 460 solution in ethanol was added to modify the polymer.

The dependence of the photoluminescence of the films upon temperature was evaluated by cutting a sample of the films and fixing them in a quartz cuvette containing approximately 3 mL of a solvent incompatible with the polymers (water for PCL-Eu and PMMA-LASOC 460 and heptyl alcohol for PVA-N-GQDs-Ag). Photoluminescent measurements were made in the range of 20 to 30 $^{\circ}\text{C}$ for PCL-Eu and 25 to 40 $^{\circ}\text{C}$ for PVA-N-GQDs-Ag and PMMA-LASOC 460 with variations of 2.5, 5 or 10 degrees. After each temperature variation, 5 min equilibrium time was allowed before photoluminescence was measured to ensure that the systems reached the desired temperatures.

3.5.3. Photoluminescent measurements

Steady-state intensity measurements with temperature variation were made at excitation/emission wavelengths of 343/616 nm for $[\text{Eu}(\text{TTA})_4](\text{Et}_3\text{NH}^+)$ and PCL-Eu, 349/441 nm for N-GQDs-Ag and PVA-N-GQDs-Ag and 420/575 nm for LASOC 460 and PMMA-LASOC 460, taking into consideration emission spectrum peak height.

3.5.4. Toxicity tests of N-GQDs-Ag

To test the toxicity of N-GQDs-Ag, a study was made with *S. cerevisiae* cells based in a procedure described in the literature [75].

3.5.4.1. Yeast preparation

To prepare yeast extract-peptone-dextrose (YPD) medium, peptone (1 %), glucose (2 %) and yeast extract (0.1 %) were dissolved in ultra-pure water and the pH of the medium was adjusted to 6.0 with 0.1 mol L^{-1} HCl solution. In order to

make a semi-solid medium, agar (3 % w/w) was added to the solution that was then sterilized in an autoclave for 15 min at 0.5 atm.

3.5.4.2.

Isolation and cultivation of *S. cerevisiae*

Saccharomyces cerevisiae (*S. cerevisiae*) cells strain were isolated from commercial baking yeast. The yeast was homogenized in ultrapure water and the resulting solution was diluted until no turbidity was visible. Cells were sampled by immersing a flame-sterilized metal loop into solution and then the material in the loop was transferred to a Petri dish containing semi-solid YPD culture medium. The dish was put in a cell growth incubator for 24 h at 30 °C. After this period, the formed cell colony was transferred to liquid medium and kept in an incubator for 12 h at 30 °C while shaking at 140 rpm. Then, the cells were sampled with the sterile metal loop and transferred to a Petri dish containing semisolid YPD culture medium and put in the cell growth incubator without shaking for 24 h at 30 °C. Finally, the dish was kept under 4 °C refrigeration and the cells were later used as pre-inoculum.

3.5.4.3.

Growth inhibition assay

In order to test the toxicity of N-GQDs-Ag, *S. cerevisiae* cells in liquid medium were exposed to them. The inoculum of *S. cerevisiae* was prepared by taking a sample of the cells from the refrigerated Petri dish and inserting it in YPD liquid culture medium (concentration twice as high as previously reported) and let to grow for 12 h at 30 °C and 140 rpm stirring. After this period, 100 µL of N-GQDs-Ag dispersion at ten different concentrations (from 0.01 to 2 % v/v) were added to the column wells of a 96-well microplate (5 replicates for each concentration). Then, 100 µL of the liquid medium containing the inoculum were added to all the wells containing N-GQDs-Ag. Control experiments were also made. For the positive control, the inoculum was added only to water (5 replicates) and for the negative control, the inoculum was added to hydrogen peroxide solution (10 % v/v) (5 replicates). Blanks were made with N-GQDs-Ag at different concentrations and YPD liquid medium without cells (3 replicates). The cells were let to grow for 24 h at 30 °C without shaking. After this period, the cells concentrations were assessed by absorption spectrometry at 570 nm. Cells grown

in the presence of N-GQDs-Ag were compared to cells grown without N-GQDs-Ag. For comparison purposes, this test was repeated with nitrogen-doped GQDs without silver (N-GQDs).

4 Characterization of luminophores

4.1. Characterization of $[\text{Eu}(\text{tta})_4](\text{Et}_3\text{NH}^+)$

The characterization of the Eu(III) complex was made to lead to its structure and to understand its optical properties. In this way, this complex was characterized through different techniques to obtain its structure based in the stoichiometry, vibrational spectra and thermogravimetric profile. In addition, the optical properties were obtained using absorption and photoluminescent spectroscopy.

4.1.1. Morphological analysis of the complex

The *tetrakis* europium β -diketonate complex presented the formula $[\text{RE}(\beta\text{-diketonate})_4](\text{Q})$ (where $\text{RE} = \text{Eu}^{3+}$, $\beta\text{-diketonate} = \text{tta}$ and $\text{Q} = \text{Et}_3\text{NH}^+$) and the calculated yield for the synthesis is 84 %. It was obtained as a reddish-orange powder (under ambient light). Under exposure to the UV, the complex has the europium characteristic red luminescence, as can be seen in Figure 4.1. The complex is stable at room temperature and does not present hygroscopicity. It is insoluble in water and highly soluble in methanol, acetone, chloroform and tetrahydrofuran.



Figure 4.1 - Image of $[\text{Eu}(\text{tta})_4](\text{Et}_3\text{NH}^+)$ complex under ambient light and under ultraviolet radiation.

4.1.2. Stoichiometric characterization

Table 4.1 presents the data obtained through the elemental analysis of carbon, hydrogen, nitrogen and sulfur (CHNS) for the synthesized complex. Results show that the calculated molecular formula is in accordance with the proposed stoichiometry, $[\text{RE}(\beta\text{-diketonate})_4](\text{Q})$, where it is evidenced the complex Eu/ligand molar ratio of 1/4, that is, the rare earth (RE) ion is in their trivalent state and coordinated to the ligands. Ligands are in the deprotonated form and the complex has a final negative charge, with (Q) being its counter-cation (Et_3NH^+).

The theoretical percentage of C, H, N and S in the complex is given through the formula:

$$\% \text{ element in sample} = \frac{\text{element mass in sample}}{\text{sample total mass}} \times 100 \quad (\text{Eq. 4.1})$$

And the percentage error of these elements is calculated using the formula:

$$\% \text{ error} = \frac{\% \text{ teoretical} - \% \text{ experimental}}{\% \text{ experimental}} \times 100 \quad (\text{Eq. 4.2})$$

The calculated percentage for the main group elements in this complex was: C (40.08 %); H (2.83 %); N (1.23 %); S (11.26 %).

In the case of a *tetrakis* complex like this one, where there is great steric hindrance because of the number of ligands and their sizes, the geometry of the complex will be determined exclusively by the characteristics of the β -diketone ligands.

Table 4.1 - CHN result for Eu^{3+} complex with tta⁻ ligand.

Complex	Elemental content (%)							
	C	E%	H	E%	N	E%	S	E%
$[\text{Eu}(\text{tta})_4](\text{Et}_3\text{NH}^+)$	39.98	0.25	2.9	2.4	1.23	0	11.3	0.35

4.1.3.

Analysis by absorption spectroscopy in the infrared region (FTIR)

In the vibrational spectra, obtained for the Htta ligand and for the Eu^{3+} complex (Figure 4.2), it is possible to identify the coordination of the ligands by the unfolding of the band centered at 1600 cm^{-1} present in the Htta spectrum. The ligands also showed overlap of the enolic $\text{C}=\text{C}$ stretching vibrations of the thenoyl ring with the stretching vibrations related to the chelate, $\text{C}=\text{C}$ and $\text{C}=\text{O}$ ($\nu_{\text{as}}\text{C}=\text{O}$), in addition to the overlap relative to the small difference in electronic density and, consequently, of the bonding strength between the carbonyl groups with the different R substitutes. The complex spectrum also presents overlap of the vibrational modes relative to the thenoyl group with the vibrational modes relating to the Eu-O bonds in the region from 400 to 600 cm^{-1} , which makes it difficult to correctly assign the vibrational frequencies. In the complex spectrum it is also observed the symmetrical stretching of the $=\text{C}-\text{H}$ aliphatic bonds between 2800 and 3100 cm^{-1} and the stretching of the $^+\text{N}-\text{H}$ bonds are observed with low intensity in the region from 2600 to 2700 cm^{-1} .

Some vibrational frequencies characteristic of the Htta ligand and the complex $[\text{Eu}(\text{tta})_4](\text{Et}_3\text{NH}^+)$ are shown in Table 4.2.

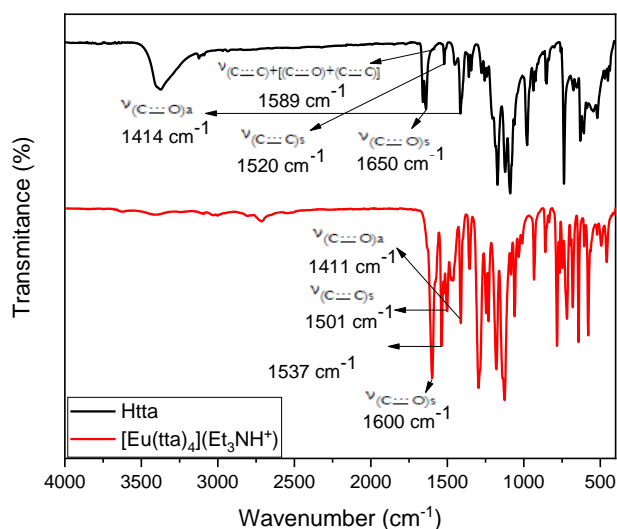


Figure 4.2 - FTIR spectra of Htta and $[\text{Eu}(\text{tta})_4](\text{Et}_3\text{NH}^+)$.

Table 4.2 – Vibrational frequencies characteristic of Htta and $[\text{Eu}(\text{tta})_4](\text{Et}_3\text{NH}^+)$.

Sample	Frequency (cm^{-1})			
	$\nu(\text{C} \cdots \text{O})_s$	$\nu(\text{C} \cdots \text{C}) + (\text{C} \cdots \text{O}) + (\text{C} \cdots \text{C})$	$\nu(\text{C} \cdots \text{C})_s$	$\nu(\text{C} \cdots \text{O})_a$
Htta	1650	1589	1520	1414
$[\text{Eu}(\text{tta})_4](\text{Et}_3\text{NH}^+)$	1600	1537	1501	1411

4.1.4. Thermogravimetric analysis (TGA/DTG)

Thermogravimetric analysis (with derivative thermogravimetry) results for the Eu(III) complex are shown in Figure 4.3. Within the temperature range from 30 to 105 °C no mass loss occurred, confirming that there are no coordinated water molecules in the complex. The first mass loss event occurred within the 105 - 120 °C range and refers to the decomposition of the non-coordinated counter-cation (Et_3NH^+). The decomposition of the complex occurred within the onset temperature of 130 °C and the maximum temperature of 340 °C where it is possible to observe minor mass loss events related to the partial decompositions of the 2-thenoyltrifluoroacetate ligands. Additional heating, up to 500 °C, suggests the formation of $\text{Eu}_2(\text{CO}_3)_3$ as the final product, obtained through calculation of the residual mass of the sample. The mass loss data of the complex are presented in Table 4.3.

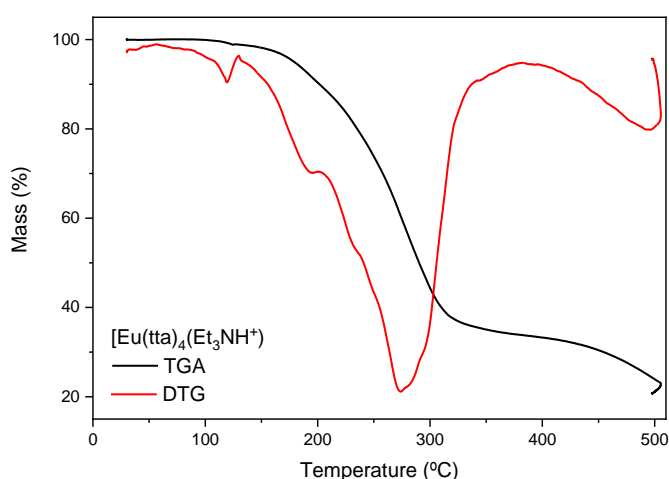
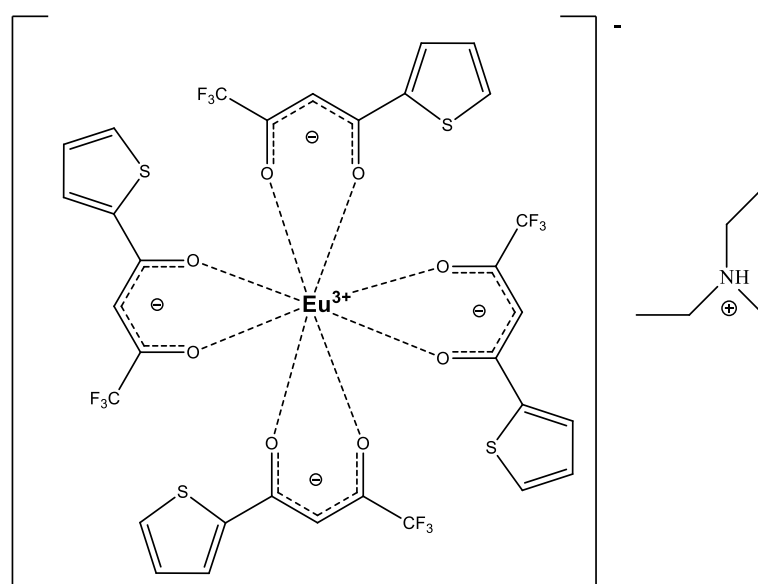
Figure 4.3 – TGA and DTG curves of $[\text{Eu}(\text{tta})_4](\text{Et}_3\text{NH}^+)$.

Table 4.3 – Thermogravimetric data for the $[\text{Eu}(\text{tta})_4](\text{Et}_3\text{NH}^+)$ complex.

Complex	Molar mass (g mol^{-1})	T_{onset} ($^{\circ}\text{C}$)	T_{max} ($^{\circ}\text{C}$)	Mass loss (%)	Residue (%)
$[\text{Eu}(\text{tta})_4](\text{Et}_3\text{NH}^+)$	1138.87	130	340	78.98	21.02

The calculated residual mass was in accordance with the experimental one, which corroborated to the stoichiometry proposed for the complex. With the characterization results for the complex, it was possible to propose its structure (Figure 4.4).

Figure 4.4 – Proposed structure of $[\text{Eu}(\text{tta})_4](\text{Et}_3\text{NH}^+)$.

4.1.5.

Optical properties of $[\text{Eu}(\text{tta})_4](\text{Et}_3\text{NH}^+)$ in solid state

Optical analysis of $[\text{Eu}(\text{tta})_4](\text{Et}_3\text{NH}^+)$, in solid state and at room-temperature, was made through photoluminescence spectroscopy. Emission spectrum of the complex $[\text{Eu}(\text{tta})_4](\text{Et}_3\text{NH}^+)$, within 500 to 850 nm (excitation at 393 nm which refers to transition ${}^7\text{F}_0 \rightarrow {}^5\text{L}_6$ of the Eu^{3+} ion), is shown in Figure 4.5. The first part of the spectrum displays the bands from the transitions ${}^5\text{D}_1 \rightarrow {}^7\text{F}_J$ ($J = 0$ to 2) of the lanthanide ion with its intensity magnified 50 times: ${}^5\text{D}_1 \rightarrow {}^7\text{F}_0$ (531 nm), ${}^5\text{D}_1 \rightarrow {}^7\text{F}_1$ (546 nm) and ${}^5\text{D}_1 \rightarrow {}^7\text{F}_2$ (560 nm). The second part of the spectrum displays the

bands from the transitions ${}^5D_0 \rightarrow {}^7F_J$ ($J = 0$ to 4) of the lanthanide ion: ${}^5D_0 \rightarrow {}^7F_0$ (577 nm), ${}^5D_0 \rightarrow {}^7F_1$ (591 nm), ${}^5D_0 \rightarrow {}^7F_2$ (616 nm), ${}^5D_0 \rightarrow {}^7F_3$ (652 nm) and ${}^5D_0 \rightarrow {}^7F_4$ (690 nm) that are in the visible region, and transitions ${}^5D_0 \rightarrow {}^7F_5$ (750 nm) and ${}^5D_0 \rightarrow {}^7F_6$ (815 nm) that are in the infrared region. It is possible to observe that the transition ${}^5D_0 \rightarrow {}^7F_2$ is predominant, causing the red emission when exposed to UV. These are characteristic bands of Eu^{3+} (narrow and well-defined). The absence of broad bands, referring to the organic part of the molecule, indicates that the ligand-metal energy transfer is very efficient.

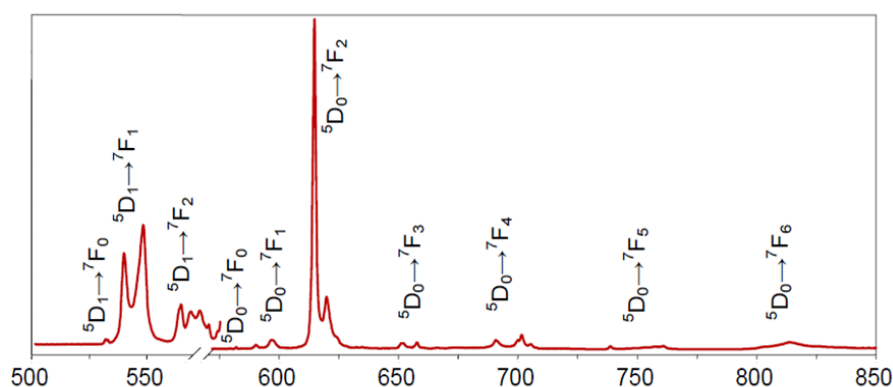


Figure 4.5 – Emission spectrum of $[\text{Eu}(\text{tta})_4](\text{Et}_3\text{NH}^+)$ in solid state under excitation at 393 nm.

4.1.6.

Optical properties of $[\text{Eu}(\text{tta})_4](\text{Et}_3\text{NH}^+)$ in solution

Optical analysis of $[\text{Eu}(\text{tta})_4](\text{Et}_3\text{NH}^+)$ in solution was first made through absorption spectroscopy in acetone/water (70/30 % v/v) at the concentration of $5.0 \times 10^{-6} \text{ mol L}^{-1}$. Figure 4.6A shows the UV-Vis absorption spectrum of the $[\text{Eu}(\text{tta})_4](\text{Et}_3\text{NH}^+)$ complex solution in acetone/water 70/30 % v/v at the concentration of $5.0 \times 10^{-6} \text{ mol L}^{-1}$. The spectrum was obtained in the spectral range of 200 to 800 nm, at room temperature, and the absorption band, centered at around 340 nm, is attributed to tta^- [190]. The molar absorption coefficient (ϵ) was calculated from the sensitivity of the analytical curve of $[\text{Eu}(\text{tta})_4](\text{Et}_3\text{NH}^+)$ and the calculated value was $1.99 \times 10^4 \text{ L mol}^{-1} \text{ cm}^{-1}$. (Figure 4.6B).

Photoluminescence of $[\text{Eu}(\text{tta})_4](\text{Et}_3\text{NH}^+)$ solution in acetone/water 70/30 % v/v at the concentration of $5 \times 10^{-6} \text{ mol L}^{-1}$ was measured at room temperature. In order to obtain the excitation spectrum, the emission was fixed at 616 nm (${}^5D_0 \rightarrow$

7F_2 transition). The excitation spectrum displays a broadband covering from 315 to 400 nm (Figure 4.7) with the best excitation at 343 nm. This result suggests that the complex is a material with broad wavelength excitation. The emission spectrum is obtained at the excitation of 343 nm and, similarly to the spectrum in solid state, it shows Eu^{3+} characteristic emission narrow lines at 590 and 616 nm (Figure 4.7). As mentioned before, these lines correspond to the ${}^5D_0 \rightarrow {}^7F_1$ and ${}^5D_0 \rightarrow {}^7F_2$ transitions, respectively, being the last one the hypersensitive transition of Eu^{3+} . The ${}^5D_0 \rightarrow {}^7F_3$ and ${}^5D_0 \rightarrow {}^7F_4$ transitions are not observed due to the overlap with the second harmonic of the lamp and the ${}^5D_0 \rightarrow {}^7F_5$ and ${}^5D_0 \rightarrow {}^7F_6$ transitions cannot be observed because they are located in the infrared region.

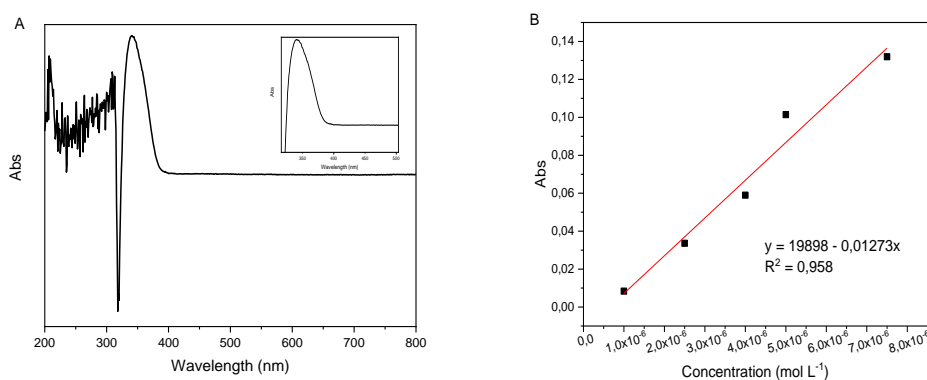


Figure 4.6 – (A) Absorption spectrum and (B) calibration curve of $[\text{Eu}(\text{tta})_4](\text{Et}_3\text{NH}^+)$

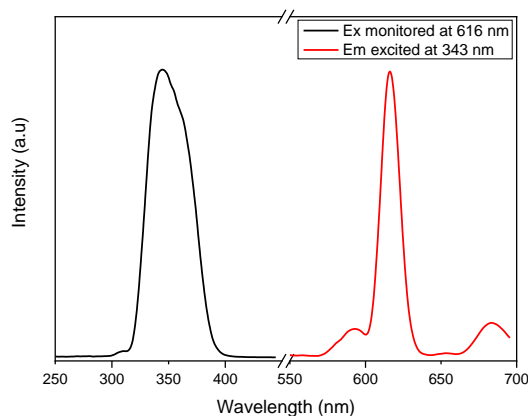


Figure 4.7 - Excitation (monitored at 616 nm) and emission (Ex = 343 nm) spectra of $[\text{Eu}(\text{tta})_4](\text{Et}_3\text{NH}^+)$ solution.

Crystals of $[\text{Eu}(\text{tta})_4](\text{Et}_3\text{NH}^+)$ complex were obtained but in the attempt of X-ray diffraction characterization they did not diffract properly and it was not

possible to collect data from the crystalline structure of the complex. Different attempts to obtain crystals were made, but none was successful.

4.2. Characterization of N-GQDs-Ag

In the development of nanoprobe, the characterization of the optical and/or electronic properties of the nanomaterials is essential. In this work, different techniques such as dynamic light scattering (DLS), ζ -potential, scanning transmission electron microscopy (STEM), X-ray photoelectron spectroscopy (XPS) and infrared spectroscopy (FT-IR) were employed and to characterize N-GQDs-Ag and evaluate their size distribution and structural characteristics. Absorption and photoluminescent spectroscopy were used to obtain N-GQDs-Ag optical profile.

4.2.1. Morphological and structural characterization of N-GQDs-Ag

The prepared N-GQDs-Ag dispersion is slightly yellow transparent and after 24 h it presented a slightly lilac transparent color (Figure 4.8A). When the dispersion was stored, in a transparent glass flask, its color gradually changed to lilac (about 15 days) as seen in Figure 4.8B and then to purple in a period of about 15 to 30 days (Figure 4.8C). After approximately 90 days, the dispersion turned brown with a visible dark particle suspension (Figure 4.8D) sometimes with formation of a silver film in the flask wall. When the dispersion was stored in amber glass flasks, the color changed to slightly brown after around 15 days and to a darker brown after around 30 days, remaining like that during about 60 days when a visible particle suspension starts to be formed. Dynamic light scattering (DLS) studies have shown the generation of nanoparticle aggregates associated with the changes in color. Under UV radiation the freshly prepared dispersion showed a visible blue color luminescence (Figure 4.8E). According to Li *et al.* [163] oxidation of graphene quantum dots dispersions prepared under autoclave conditions occurs when the content is exposed to atmospheric oxygen promoting similar color change.



Figure 4.8 - N-GQDs-Ag dispersion at (A) day 1, (B) day 15, (C) day 30, (D) day 90 and (E) day 1 under UV radiation.

4.2.2. Total carbon analysis

Analysis of the N-GQDs-Ag dispersion resulted in the concentration of about 20.9 g L^{-1} of total carbon (TC). From this stock dispersion, the working dispersions (after 1000 times dilution) were prepared with total carbon concentration of 21 mg L^{-1} .

4.2.3. Dynamic light scattering and ζ -potential analysis

Dynamic light scattering (DLS) and ζ -potential measurements were performed to obtain hydrodynamic size distributions and charge of N-GQDs-Ag, dispersed in aqueous solution, in function of pH. Measurements of ζ -potentials were made 24 h after the production of the N-GQDs-Ag before and after exposing them to UV radiation (15 min). A volume of 2.5 mL of each sample was placed in the cuvette and measurements were made in seven replicates, at temperature of 25°C and angles of 90° or 173° . The use of urea as the precursor of N during the production of GQDs can lead to the incorporation of nitrogen atoms into the graphitic matrix of GQDs in the form of pyridinic-N, graphitic-N and pyrrolic-N, which can contribute with electrons to the π -electron system [191]. In Figure 4.9A it is shown that the surface of the N-GQDs-Ag, at pH 3.0, is positively charged probably due to the protonation of nitrogen atoms (pyridinic-N and pyrrolic-N could be acceptors of protons [163]. At pH 4.0 and 5.0, ζ -potential values about 0.1 and -0.4 mV, respectively, were obtained because the more limited availability of H^+ ions. Negative surface charges of the N-GQDs-Ag is probably due to the

presence of carboxylic acid and hydroxyl groups which tend to be deprotonated depending on their characteristic pK_a value. As the pH increases, ζ -potential values close to zero were obtained because the material reaches the isoelectric point. The N-GQDs-Ag remained stable in alkaline environment, which can be attributed to the rich nitrogen containing organic groups on the surface. These results are in agreement with the ones reported by Li *et al.* [163].

When the N-GQDs-Ag are exposed to UV, a ζ -potential value close to zero or slightly negative is obtained for all pH values (Figure 4.9B) probably due to the fact that carbonyl groups increase notably, originated from photochemical oxidation [192].

At pH 3, low aggregation of the nanomaterial was evidenced by the measured hydrodynamic size obtained by DLS. At lower pH, smaller size of N-GQDs-Ag (after 24 h of production) was obtained with increasing in size as pH increased (Figure 4.10). From pH 3 to 6, nanoparticle sizes increase from 2.5 nm to 4.6 nm and as the pH reaches the range from 7 to 10, it is observed sizes from 7.5 to 9.9 nm. When the N-GQDs-Ag were exposed to UV, a larger size and a greater dispersion of the results were observed (Figure 4.10) as UV tends to promote aggregation of the nanomaterial [116]. The size of the nanomaterial after 120 h of production (without exposure to UV) was also measured (Figure 4.10) and a small increase in size (in respect to the size measured after 24 h of production) was observed mainly at pH greater than 7. The sizes of N-GQDs-Ag after 120 h are close to the ones exposed to UV after 24 h of production. Such increasing in the size of the nanomaterial can be justified due to the incorporation of functional groups, as a consequence of an oxidation reaction from atmospheric oxygen, which contribute to the aggregation of the N-GQDs-Ag as suggested by Li *et al.* [163].

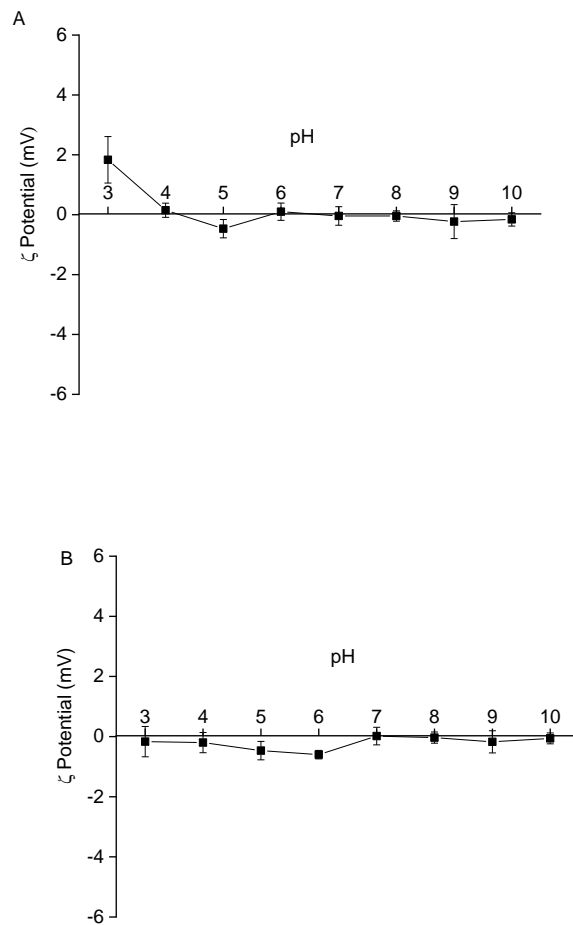


Figure 4.9 - ζ -potential of N-GQDs-Ag in function of pH 24 h after production (A) without exposure to UV-radiation and (B) under exposure to UV-radiation for 15 min.

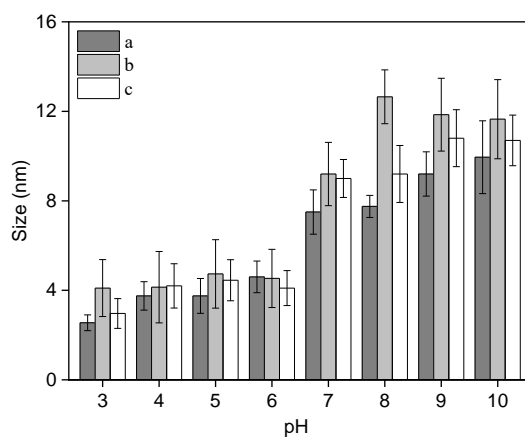


Figure 4.10 - Size distribution of N-GQDs-Ag in aqueous dispersion in function of pH obtained by DLS (a) 24 h after preparation, (b) 24 h after preparation and 15 minutes exposure to UV and (c) 120 h after preparation.

4.2.4. Scanning transmission electron microscopy analysis

Results from *scanning transmission electron microscopy* (Figure 4.11) corroborate with DLS results, showing that the produced N-GQDs-Ag had a size distribution in the range from 4 to 20 nm with an average diameter of 11.2 ± 2.7 nm, increasing to 40 nm as aggregation occurs due to pH increasing or by incidence of UV.

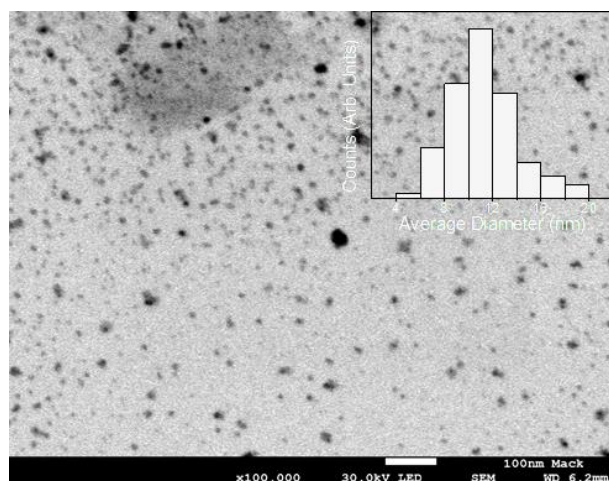


Figure 4.11 - STEM image of size distribution of N-GQDs-Ag.

4.2.5. X-ray photoelectron spectroscopy analysis

XPS analysis was used to verify the presence of N-substituents in the GQDs structure. The general survey showed characteristic peaks for carbon, oxygen and nitrogen at binding energies of 285 eV (C 1s), 533 eV (O 1s) and 401 eV (N 1s), (Figure 4.12 A). The spectrum showed C 1s peaks at 284.9 eV, 285.9 eV, 286.7 eV, 288.2 eV and 289.2 eV (Figure 4.12B), which can be assigned to the contributions of C=C and C-C, C-N, C-O-C and C-OH, C=O and COOH, respectively. The deconvoluted N 1s spectra (Figure 4.12C) also showed peaks at 400.3 eV, 401.2 eV and 402.7 eV, which correspond to pyrrolic-N, graphitic-N, and pyridinic-O, respectively. These assignments are in accordance with results recently reported [193]. The peak at 398.8 eV, which corresponds to pyridinic-N is very small (area could not be calculated). In contrast, N 1s main peak corresponds to the graphitic bound to N at binding energy 401.2 eV which presented area corresponding to 41.19

% of the total while the pyrrolic bound to N and the pyridinic bound to O correspond to 29.02 % and 29.79 %, respectively. In summary, XPS results strongly suggest nitrogen functionalization (organic in nature) of GQDs at the edges and surface.

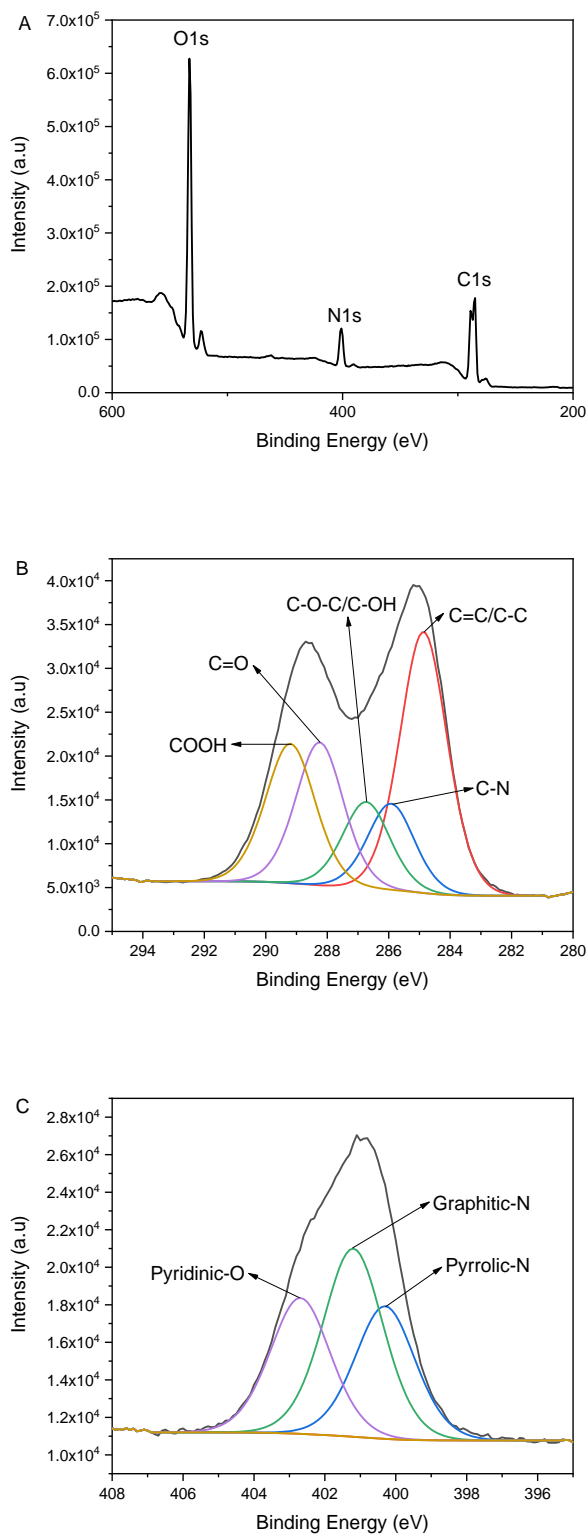


Figure 4.12 - (A) XPS general survey scan of N-GQDs-Ag, (B) deconvoluted C 1s peaks and (C) deconvoluted N 1s peaks.

4.2.6. Absorption spectroscopy in the infrared region analysis

Vibrational spectrum obtained for the dry sample of N-GQDs-Ag (Figure 4.13) indicated the presence of oxygen and amino functional groups on the N-GQDs-Ag. The wide band at 2650-3750 cm^{-1} refers to O-H and N-H stretching vibrations. Also, the bands in the region from 1030 to 1630 cm^{-1} suggest the presence of the stretching vibrations of C=C, C=N, COO-, COOH, C-OH, C-N, C-OH/C-C/-OH and C-H. In addition, amide-carbonyl stretching vibration (-NH-C=O-) was observed at 1652 cm^{-1} , indicating the formation of amide groups through the interaction with carboxylic groups. These results are in accordance with ones previously reported [194-196].

Through XPS and FTIR analyses it could not be identified covalent bonds between Ag and C or N, which indicates a possible ionic interaction for the Ag decorating the surface/edges of GQDs.

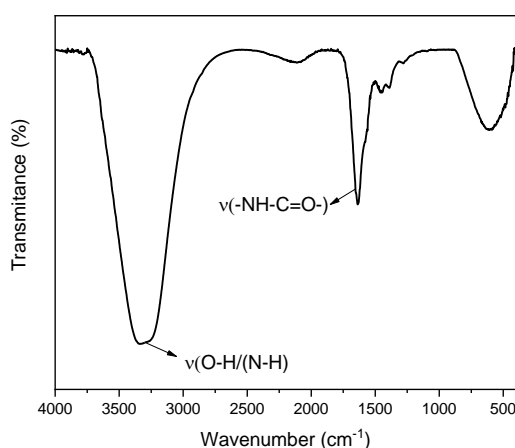


Figure 4.13 - FT-IR spectra of N-GQDs-Ag.

4.2.7. Optical properties

Optical properties of N-GQDs-Ag were studied using up to 1000 times dilution factor of the original N-GQDs-Ag dispersion. The extinction spectrum (Figure 4.14) showed a characteristic peak close to 200 nm, which is related to the π - π^* transition of aromatic C=C bonds probably influenced by the presence of N

functionalizing groups. The band centered at 335 nm corresponds to the first excitonic and possibly to the $n-\pi^*$ transitions of the C=N bonds.

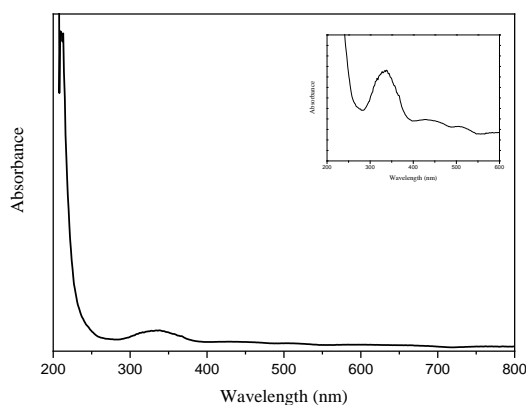


Figure 4.14 - Absorption spectrum of N-GQDs-Ag.

The dispersions of N-GQDs-Ag showed blue-violet emission with its maximum centralized at 441 nm under excitation at 349 nm (Figure 4.15). The quantum yield (ϕ) of N-GQDs-Ag was estimated in 25 % (at 25 °C) using quinine sulfate (347/448 nm) as a comparative standard. Calculations were made based on the information obtained from the calibration curves of integrated photoluminescence intensity against absorbance of the N-GQDs-Ag and quinine sulfate samples. The gradient (or slope) of both curves were calculated and applied in Equation 3.2 to obtain the Φ value of N-GQDs-Ag.

The photoluminescence of the N-GQDs-Ag was compared with the photoluminescence of nanoparticles not modified with silver (N-GQDs) and, although the photoluminescence of N-GQDs-Ag right after preparation is four times lower than the photoluminescence of N-GQDs, it is more stable than the photoluminescence of the nanoparticles not modified with silver, which decreases to half the initial intensity in about 20 days while the photoluminescence of nanoparticles modified with silver takes around 60 days to decrease to half the initial intensity.

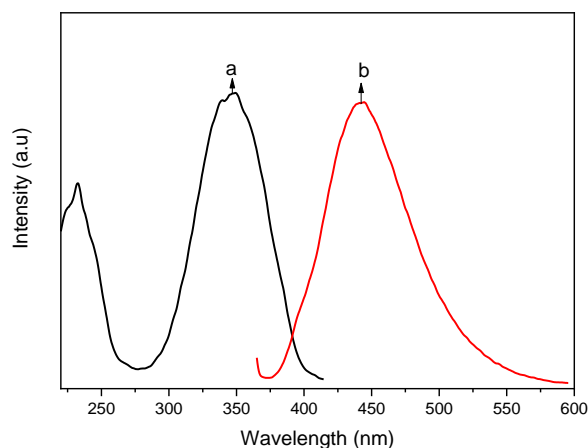


Figure 4.15 - N-GQDs-Ag (a) excitation and (b) emission spectra.

4.3. Characterization of LASOC 460

The characterization of LASOC 460 was previously reported [197] and the structural and optical properties of the molecule were shown. The structure of LASOC 460 molecule is shown in Figure 4.16. In this work, the optical properties of the LASOC 460 molecule were obtained in probe conditions through absorption and photoluminescent spectroscopy.

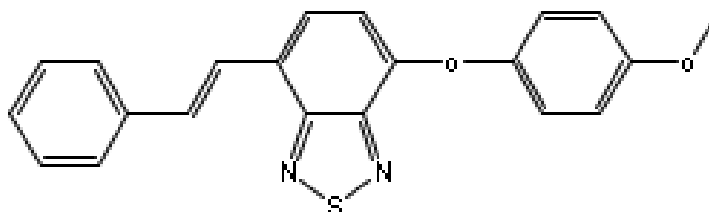


Figure 4.16 – Structure of 4-(4-methoxyphenoxy)-7-styrylbenzo[c][1,2,5]thiadiazole (LASOC 460).

4.3.1. Optical properties

The optical properties of LASOC 460 in the probe conditions were studied using 5.0×10^{-6} mol L⁻¹ solutions prepared in absolute ethanol (non-aggregated form) and in ethanol/water ratio of 15/85 % v/v (aggregated form). The excitation

spectra of both non-aggregated and aggregated forms were obtained with their maximums centralized at 420 nm. However, the emission spectrum of the non-aggregated form was obtained with its maximum at 585 nm (yellow emission) while the emission spectrum of the aggregated form was obtained with its maximum at 565 nm (blue-shift of 20 nm with green-yellow emission). It was also observed that the intensity of the aggregated form is three times higher than the intensity of the non-aggregated form (Figure 4.17 A and B).

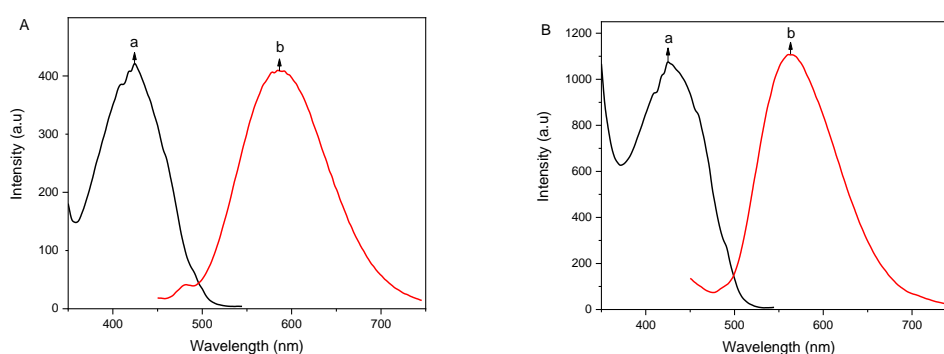


Figure 4.17 – (A) LASOC 460 (a) excitation and (b) emission spectra in the non-aggregated form and (B) LASOC 460 (a) excitation and (b) emission spectra in the aggregated form.

The absorption spectra of LASOC 460 (Figure 4.18) for both non-aggregated and aggregated forms were obtained in the spectral range of 200 to 800 nm. The spectrum of the non-aggregated form showed a peak around 420 nm, while the spectra of the aggregated form showed a peak around 430 nm (red shift) and both peaks correspond to π - π^* transitions. For the non-aggregated form, another peak close to 300 nm was observed, while for the aggregated form this peak was observed around 310 nm (red shift). These peaks are related to the benzothiadiazole ring.

The molar absorption coefficient (ϵ) was calculated for both non-aggregated and aggregated forms and the calculated values were $4.160 \times 10^4 \text{ L mol}^{-1} \text{ cm}^{-1}$ and $4.016 \times 10^4 \text{ L mol}^{-1} \text{ cm}^{-1}$, respectively.

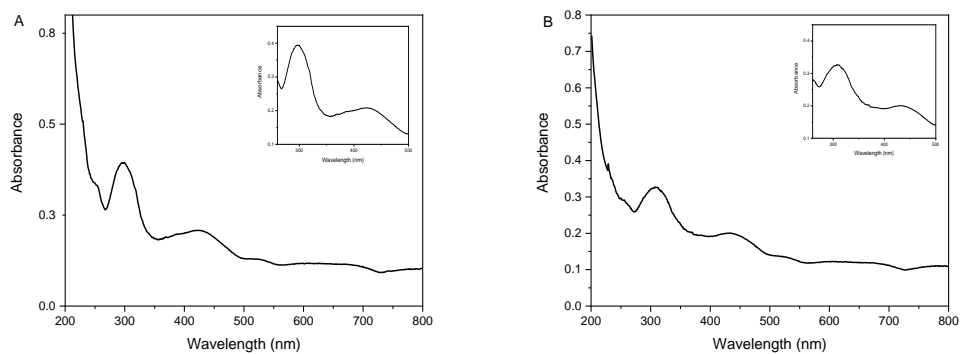


Figure 4.18 - Absorption spectrum of LASOC 460 in (A) non-aggregated form and (B) aggregated form.

5

Use of selective quenching of a photoluminescent probe based on a Eu(III) β -diketonate complex for determination of methylmercury in produced water after liquid-liquid extraction

Material published as “*Use of selective quenching of a photoluminescent probe based on a Eu(III) β -diketonate complex for determination of methylmercury in produced water after liquid-liquid extraction*” Juliana da S. Padilha, Marcelo F.M.F. Azevedo, Jarol R. Miranda-Andrades, Anna De Falco, Jiang Kai, Ricardo Q. Aucelio, *Talanta*, 244 (2022) 123406, DOI: 10.1016/j.talanta.2022.123406 (See attachment A1).

5.1.

Analytical method using Eu(III) to determine methylmercury

In this chapter, a method to determine CH_3Hg^+ in PW is presented. A simple synthetic route was used to obtain the *tetrakis* europium β -diketonate complex used as sensor for CH_3Hg^+ . Analytical responses towards CH_3Hg^+ along with a liquid-liquid extraction allowed selectivity, reducing matrix interferences from PW sample.

A wide variety of methods based on lanthanide probes have been previously reported for the determination of mercurial species. However, in terms of real applicability, most of these probes reported in the literature have limitations, such as restricted conditions for sensing, complicated and/or time-consuming synthetic routes for the probes, instability and slow response towards the analyte. In this way, the method presented in this chapter is an attempt to circumvent these limitations.

5.2. Results and discussion

5.2.1. Preliminary studies for the choice of the lanthanide complex

In the preliminary studies, the available lanthanide complexes were evaluated in terms of stability. In order to do this, photoluminescence from the solutions of these different complexes were measured before and after being exposed to either UV radiation or visible light, inside a photochemical reactor, for a time interval of 15 min. From the obtained data it was possible to observe that the solutions of all complexes presented very low photostability under UV irradiation, what is a typical behavior of lanthanide complexes [198] showing that UV radiation induces their photodegradation. In contrast, under visible light, the complexes [Eu(tta)₃Phen], [Eu(DBM)₃(TPPO)₂], [Eu(tta)₄](Et₃NH⁺) and [Tb(sal)₃(H₂O)_x] had their original photoluminescence reduced along the experiment (some of them more affected from others) showing that these complexes are photosensitive at different levels and should be manipulated protected from ambient light. The complexes [Tm(DBM)₃Phen] and [Tb(acac)₃Phen] did not present satisfactory photoluminescence after light exposure and they were discarded as a possible photoluminescent probes.

For the final choice of the complex to be used as a probe, points such as intense photoluminescence and resistance to photo-degradation were considered along with structural characteristics of the complex aiming the possibility of it interacting with the analyte. Taking into account all these points, the complex [Eu(tta)₄](Et₃NH⁺) was the one that stood out the most and was chosen to be used in this work.

5.2.2. Solubility test of [Eu(tta)₄](Et₃NH⁺)

Results from solubility tests showed that the [Eu(tta)₄](Et₃NH⁺) complex is very soluble in acetone and tetrahydrofuran, that is, the compound readily solubilizes when in contact with these solvents. It also presented good solubility in methanol and chloroform, meaning that the compound solubilizes after a few seconds of contact with the solvents by stirring. The complex is insoluble in cold

ethanol and only solubilizes after heating of the solvent. Also, the complex is insoluble in hexane, not solubilizing in this solvent under any conditions.

Taking into consideration the results of the solubility test and the properties of the solvents used, acetone was chosen to prepare the working solutions, since it is a polar solvent that can be used mixed with water, allowing compatibility with aqueous samples.

5.2.3.

Stability test of $[\text{Eu}(\text{tta})_4](\text{Et}_3\text{NH}^+)$ in solution

One of the most important steps in the development of a photoluminescent probe is the evaluation of the photoluminescent emission stability of the material being proposed to be used as a probe. From the preliminary tests we learned that this complex is photodegraded when exposed to UV radiation and that it loses part of its photoluminescence when exposed to visible light. To evaluate the photoluminescence decay rate, the work solution of the complex $[\text{Eu}(\text{tta})_4](\text{Et}_3\text{NH}^+)$ has undergone a monitoring of its photoluminescent emission signal in the transition ${}^5\text{D}_0 \rightarrow {}^7\text{F}_2$ (616 nm) over time being exposed only to ambient light. It was also monitored when the solution was protected from light. Then, the work solution has also undergone another type of monitoring of its photoluminescent emission signal in the transition ${}^5\text{D}_0 \rightarrow {}^7\text{F}_2$ under UV irradiation which consisted of recording the emission intensity of the solution in the spectrofluorometer for a continuous period of time where in the end a graph intensity *vs.* time was obtained.

The photoluminescent intensity of the complex solution was monitored in the transition ${}^5\text{D}_0 \rightarrow {}^7\text{F}_2$ (616 nm), during a period of 180 min in which the probe solution was placed in a glass vial and exposed to ambient light. During this period, it was observed a photoluminescence decrease of around 10 % (Figure 5.1A), indicating that the complex is photosensitive, requiring protection from ambient light during preparation and storage of probe solutions. In contrast, control tests made with probe solution stored in the dark produced no significant photoluminescence variation (Figure 5.1B). shows that the variation is negligible and can be attributed to instrumental error. In the study to evaluate the exposure to UV (in this case at the excitation wavelength of 343 nm), it was used the kinetic mode of the photoluminescence spectrophotometer with continuously measuring

photoluminescence during 6 min. It was observed a small systematic variation of intensity (of less than 0.5 % or 3 arbitrary units of signal per minute) indicating enough stability to perform photoluminescence measurements and scanning that usually take less than 2 min to perform (Figure 5.1C).

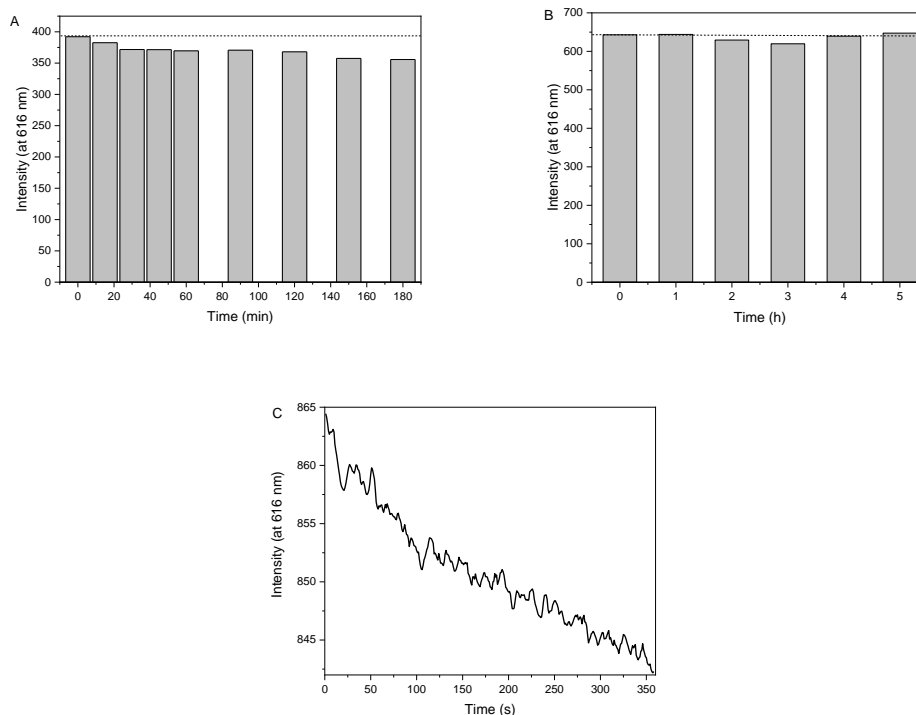


Figure 5.1 – $[\text{Eu}(\text{tta})_4](\text{Et}_3\text{NH}^+)$ emission intensity variation (A) under exposure to ambient light, (B) protected from light and (C) under exposure to UV radiation.

5.2.4.

Stability test of $[\text{Eu}(\text{tta})_4](\text{Et}_3\text{NH}^+)$ in solid substrate

Photoluminescence stability of the complex $[\text{Eu}(\text{tta})_4](\text{Et}_3\text{NH}^+)$ has been also tested on a cellulose substrate in the form of filter paper at room temperature. If the complex was stable in this type of substrate, this matrix could be used for tests with analyte, minimizing restrictions related to solvent system.

Photoluminescence emission bands of $[\text{Eu}(\text{tta})_4](\text{Et}_3\text{NH}^+)$ are shown in Figure 5.2 using the phosphorescence mode of the instrument in order to establish a delay time to minimize background influence of the cellulose paper substrate still measuring the lifetime longer luminescence characteristic of europium complexes. The measurements were made in a time span of 60 min and it was possible to verify that photoluminescence of the complex decreases, losing approximately 40 % of its

intensity over the period of the experiment, which suggests that the complex is not stable in this type of solid matrix. Another possible explanation for this phenomenon is the influence of molecular oxygen present in the air, that may affect triplet state that eventually is involved in the photo-physical process, that is, affecting energy transfer between triplet and singlet states. This explanation can be quite plausible since oxygen is a known deactivator of excited triplet state.

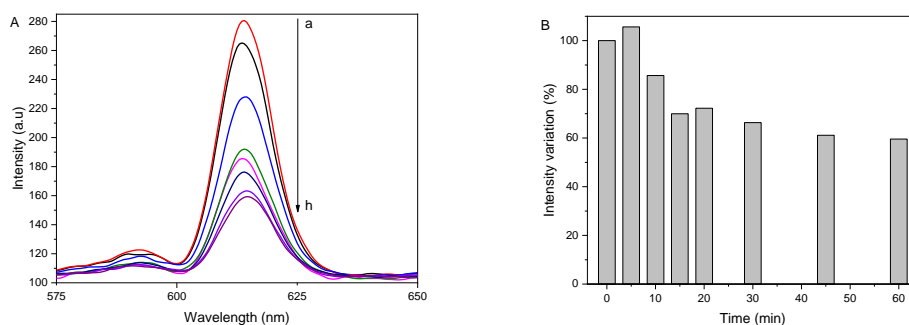


Figure 5.2 – (A) Photoluminescence emission spectra of [Eu(tta)₄](Et₃NH⁺) on filter paper substrate over a) 0, b) 5, c) 10, d) 15, e) 20, f) 30, g) 45 and h) 60 min and (B) variation of intensity over time (peak height).

5.2.5. Influence of atmospheric oxygen (O₂) on the solid complex placed in substrate

The molecular oxygen present in the air is an important factor with regard to the longer lifetime luminescence processes, as it may be responsible for the partial or even total quenching of photoluminescence. For this reason, a more complete study was conducted to verify whether the instability of the photoluminescence of the complex [Eu(tta)₄](Et₃NH⁺) is related to the effect of molecular oxygen present in the air.

The emission spectra of [Eu(tta)₄](Et₃NH⁺) placed on filter paper substrate, using a quartz window protection to shield the complex from the air, is shown in Figure 5.3A. It was possible to verify that when the solid complex was protected the photoluminescence quenching (compared to the one measured at the beginning of the experiment) was less effective (approximately 13 % reduction as seen in Figure 5.3B) in the same time period of the test where there was no protection (5.2). It is also observed that the quartz window acts as an optical filter as the initial

photoluminescence measured from the solid complex is approximately half the intensity observed in the test where there is no protection of the quartz window.

Studies have already shown that the interaction of molecular oxygen with molecules in the triplet state causes the deactivation of the excited molecule to the fundamental state ($T_1 \rightarrow S_0$) [199-201]. The deactivation of the excited molecule is accompanied by the transition of oxygen from its natural triplet state to an excited singlet state [202]. One of the models followed to describe this type of interaction proposes the charger transfer, by contact, between oxygen and the compound [203-204].

The Stern-Volmer equation [203] is also useful to show that, as the lifetime of the luminophore is longer, the influence of oxygen is more significant than when compared to short lived fluorescence processes (Equation 5.1), where I and I_0 are photoluminescence in the presence and absence of a concentration analyte $[Q]$, respectively. In addition, the decrease in luminescence is directly proportional to the increase in oxygen concentration.

$$I/I_0 = K_{SV} [Q] \quad (\text{Eq. 5.1})$$

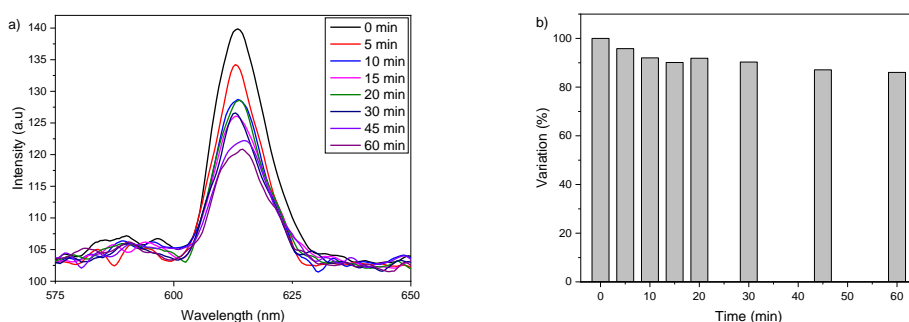


Figure 5.3 – (A) Photoluminescence emission spectra of $[\text{Eu}(\text{tta})_4](\text{Et}_3\text{NH}^+)$ on filter paper substrate protected with a quartz window over a) 0, b) 5, c) 10, d) 15, e) 20, f) 30, g) 45 and h) 60 min. and (B) variation of the emission over time (peak height).

5.2.6. Choice of analyte

After the complex $[\text{Eu}(\text{tta})_4](\text{Et}_3\text{NH}^+)$ was characterized and its stability in solution was determined, it was possible to choose the analyte to be used in this

work. As the complex was more stable in solution (solvation probably shielding influence of dissolved oxygen) it was decided to use the sensor in solution.

Taking into consideration mainly the chemical structure of the complex $[\text{Eu}(\text{tta})_4](\text{Et}_3\text{NH}^+)$, mercurial species were chosen to be used as the analyte. As Eu^{3+} ion is bonded to 4 tta^- ligands that are bulky, it is completely shielded from the influence of the external environment around it, which hinders any sensitizing by chemical species that does not interact with the complex in a specific process. As the lateral chain of the tta^- ligand presents a sulfur atom that does not show any steric hindrance in the complex structure, it is readily available to interact with mercury as these two elements have high affinity. This strong ionic interaction between mercury and sulfur can be explained by Pearson's theory of hard and soft acids and bases (HSAB) which says that hard acids prefer to combine with hard bases and soft acids prefer to combine with soft bases [205]. Thus, sulfur is characterized as a soft base and mercury is characterized as a soft acid, which makes them have great attraction to each other.

It is believed that by interacting mercury (in Hg^{2+} or CH_3Hg^+ forms) with the complex $[\text{Eu}(\text{tta})_4](\text{Et}_3\text{NH}^+)$, mercury will bind to the sulfur atom and thereby interrupt the ligand-metal intramolecular energy transfer (Antenna Effect) causing the complex to lose its energy and, therefore, its photoluminescence.

5.2.7.

Choice of acetone/water ratio

In terms of the solvent system used for the analytical probe, it is important to ensure total solubilization of the complex, intense photoluminescence and proper medium compatible with aqueous samples, allowing probe-analyte interaction to occur more effectively. Acetone was chosen to dissolve the complex (due to the high solubility, miscibility with water and availability) and the proportion of water (20 %, 30 % and 50 %) to be mixed with the acetone, to form the probe solution, was tested in terms of intensity and stability of photoluminescence over 72 h. It was possible to verify that the photoluminescence of the $[\text{Eu}(\text{tta})_4](\text{Et}_3\text{NH}^+)$ solution is not stable when water comprised 50 % of the solution with about 17 % of signal decreasing over 72 h. One possible explanation is the fact that larger proportions of water, surrounding the complex, may be interfering in its coordination sphere,

where the exchange of ligands occurs by the effect of concentration. Although the Eu^{3+} is shielded from the external environment by four chelate rings of the tta^- ligands, its concentration in the solution is low when compared to the amount of water molecules, so that the exchange of tta^- ligands by H_2O ligands is forced over time. As the proportion of water was reduced to 30 % or 20 % the photoluminescence decreasing was minimized by less than 1 % over 72 h. A greater amount of acetone molecules probably ensured a better solvation of water molecules hindering the interaction of water with the complex. The acetone/water proportion chosen was 70/30 % v/v.

5.2.8. Study of pH influence

The effect of the concentration of H^+ in the solution that comprises the analytical probe tends to affect the intensity of photoluminescence because of the reactions involving $[\text{Eu}(\text{tta})_4](\text{Et}_3\text{NH}^+)$. This factor, evaluated as the nominal pH measured from the acetone/water 70/30 % v/v probe solution after addition of either NaOH (0.01 mol L^{-1}) or HNO_3 (0.01 mol L^{-1}), was evaluated in the pH range of 4.0 – 9.0. Results show that the photoluminescence is the strongest at the original pH of the probe solution (pH 6.8) without any addition of acid or hydroxide (Figure 5.4). When the medium is more acidic, the coordination is broken, liberating free Eu^{3+} as ligands are re-protonated becoming no longer available to bind the metal ion. When concentration of OH^- becomes relevant, these ions tend to compete with the ligands, promoting the formation of europium hydroxide rather than the formation of the europium complex. It is important to point out that when pH is restored back to 6.8, after acidification or alkalization, the original photoluminescence of probe solution is restored, indicating the dynamic acid-base equilibrium involved.

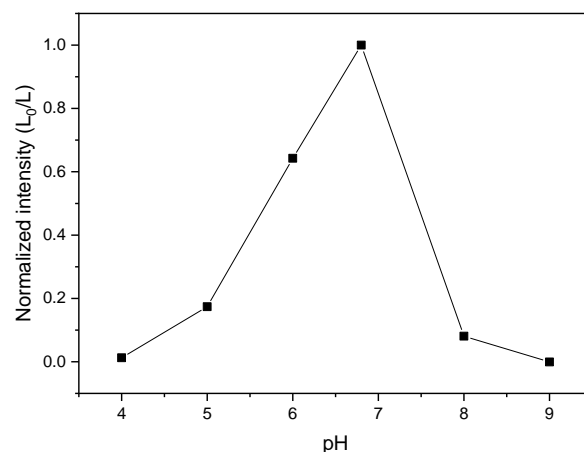


Figure 5.4 - $[\text{Eu}(\text{tta})_4](\text{Et}_3\text{NH}^+)$ photoluminescent intensity changes at different pHs.

5.2.9. Tests of temperature influence

The effect of the temperature of the probe solution on the measured photoluminescence was evaluated by placing the stoppered cuvette in a Peltier thermostatic system at fixed temperatures between 20 and 30 °C (with temperature variation of 2 °C). It was found that the measured photoluminescence from the $[\text{Eu}(\text{tta})_4](\text{Et}_3\text{NH}^+)$ tends to be stronger at lower temperatures (Figure 5.5A), decreasing as the temperature is increased (decreasing of about 30 % in this temperature interval), following a linear relation ($R^2 = 0.99$) (Figure 5.5B). It was also observed that when lower temperatures are restored, the photoluminescence is also restored back to original values.

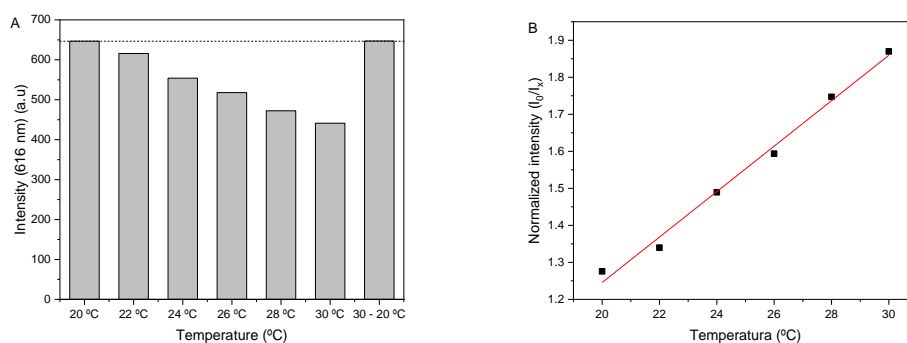


Figure 5.5 – (A) $[\text{Eu}(\text{tta})_4](\text{Et}_3\text{NH}^+)$ photoluminescent intensity changes at different temperatures and (B) linear relationship between photoluminescent intensity and temperature.

5.2.10. Probe sensitivity towards mercurial species

As the experimental conditions of the analytical probe were established, the effects of the presence of mercurial species (organic and inorganic) in the photoluminescence intensity of the $[\text{Eu}(\text{tta})_4](\text{Et}_3\text{NH}^+)$ probe were evaluated by monitoring the characteristic Eu^{3+} emission at 616 nm and using increasing concentrations of mercurial species. The test with mercurial species aimed to evaluate the relative selectivity taking into consideration both Hg^{2+} and CH_3Hg^+ . Inorganic mercury is pH-sensitive and, in solution, it is only stable at high concentrations of H^+ , otherwise the formation of hydroxide is favored. Since the best pH for the use of the probe is its original (pH = 6.8 as seen in the chosen conditions for the probe in Table 5.1), it is expected that the probe shows selectivity towards organic mercury in the form of methylmercury instead of inorganic mercury.

Table 5.1 - Experimental conditions for mercury determination.

Experimental parameter	Optimized value
Probe	$[\text{Eu}(\text{tta})_4](\text{Et}_3\text{NH}^+)$
Probe concentration	$5.0 \times 10^{-6} \text{ mol L}^{-1}$
pH	6.8 (original pH of solution)
Time for probe stabilization	1 h
Temperature	25 °C
Probe volume	4.5 mL
Final volume	5 mL

5.2.10.1. Tests with inorganic mercury

The emission spectra of the analytical curve constructed by adding increasing concentrations of Hg^{2+} in the working probe dispersion is shown in Figure 5.6A. It was observed that Hg^{2+} caused suppression on $[\text{Eu}(\text{tta})_4](\text{Et}_3\text{NH}^+)$ photoluminescence intensity, resulting in signals variation from 92 % of the original probe signal at the lowest Hg^{2+} concentration ($40 \mu\text{g L}^{-1}$) to 77 % of the original probe signal at the highest concentration of Hg^{2+} ($200 \mu\text{g L}^{-1}$). This mild suppression imposed by Hg^{2+} may be related to the effect of the pH of the medium

that hinders the action of mercury ions as a significant fraction of it (at pH 6.8) is readily hydroxylated. For this reason, an additional study was made by monitoring the photoluminescence over time (up to 48 h) after addition of Hg^{2+} at different concentrations (Figure 5.6B). It was observed that at lower concentrations of Hg^{2+} (40 and 80 $\mu\text{g L}^{-1}$), there was partial recovery of emission intensities over time until they reach their stability (3 h). At the midpoint of the curve ($[\text{Hg}^{2+}] = 120 \mu\text{g L}^{-1}$), the photoluminescence intensity of the probe, after suppression caused by Hg^{2+} , remained constant throughout the time interval in which it was monitored. At higher concentrations of Hg^{2+} (160 and 200 $\mu\text{g L}^{-1}$), over time the suppression of the probe signal continues to occur until it reaches stability (3 h). In any case, results indicate the effect that formation of mercury (II) hydroxylated complexes as well as the precipitation of HgCl_2 affects analytical response, making measured results unreliable. The variations that occur due to the photoluminescence quenching of the probe caused by Hg^{2+} may be what explains the low linear correlation of data in the analytical curve that presented $R^2 = 0.923$ (Figure 5.6C).

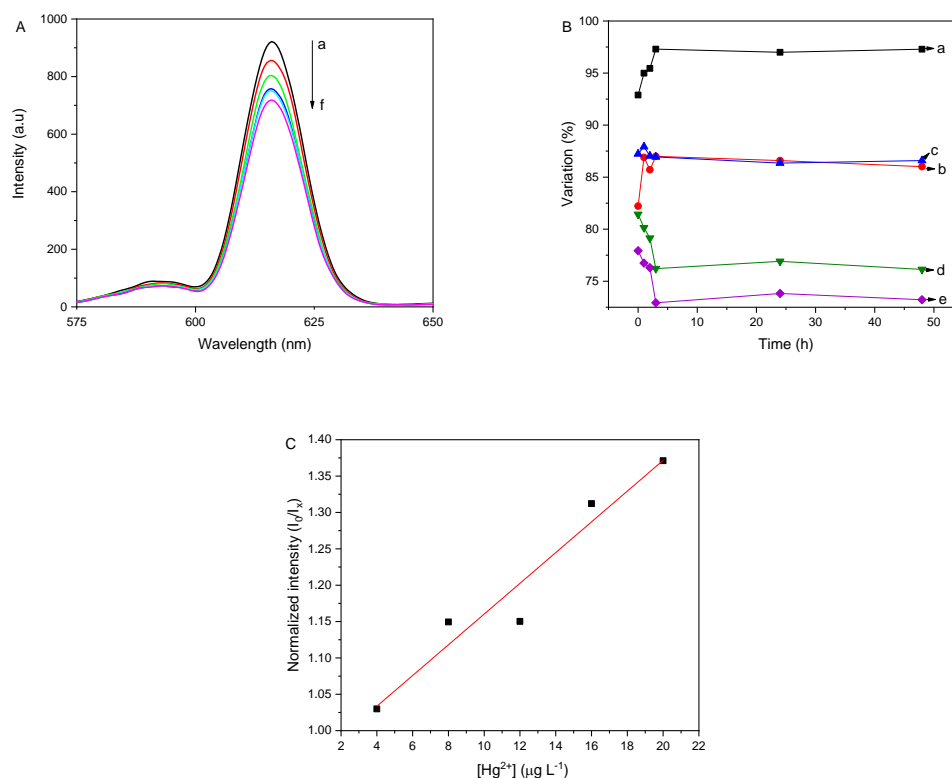


Figure 5.6 – (A) Emission spectra for the photoluminescence responses of $[\text{Eu}(\text{tta})_4](\text{Et}_3\text{NH}^+)$ for concentrations of Hg^{2+} at a) 0, b) 40, c) 80, d) 120, e) 160 and f) 200 $\mu\text{g L}^{-1}$, (B) variation of emission intensities from 0 to 48 h for concentrations of Hg^{2+} at a) 40 b) 80, c) 120, d) 160 and e) 200 $\mu\text{g L}^{-1}$ and (C) Relationship between normalized photoluminescent intensity and Hg^{2+} concentration.

5.2.10.2. Tests with organic mercury

The effect imposed by the increasing concentrations of organic mercury, in the form of CH_3Hg^+ , upon the photoluminescence measured from the Eu^{3+} complex probe was studied and the results are shown in the set of spectra in Figure 5.7A. Increasing concentrations of CH_3Hg^+ varying from 40 to $200 \mu\text{g L}^{-1}$ were added to $[\text{Eu}(\text{tta})_4](\text{Et}_3\text{NH}^+)$ solutions and it was observed that when the concentration of CH_3Hg^+ is increased, the photoluminescence quenching becomes more effective. The analytical curve using normalized data (I_0/I) is shown in Figure 5.7B, indicating a better relation between the photoluminescence intensity and concentration of CH_3Hg^+ ($R^2 = 0.967$) than the one found between Eu^{3+} and Hg^{2+} ($R^2 = 0.923$).

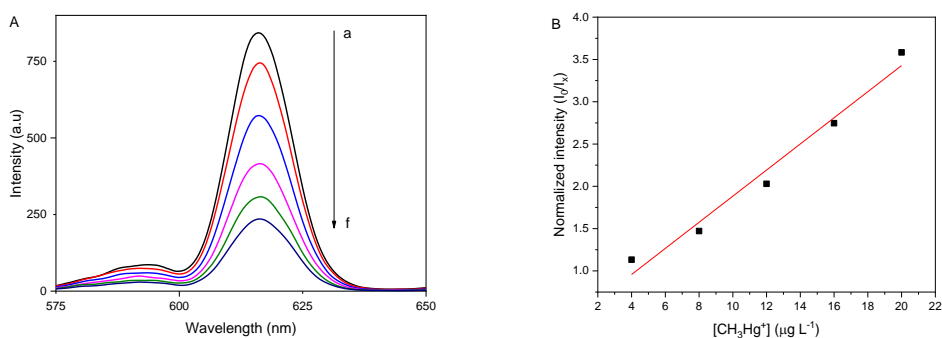


Figure 5.7 – (A) emission spectra with the photoluminescence responses of $[\text{Eu}(\text{tta})_4](\text{Et}_3\text{NH}^+)$ for concentrations of CH_3Hg^+ at a) 0, b) 40, c) 80, d) 120, e) 160 and f) $200 \mu\text{g L}^{-1}$ and B) graph of the linear relationship between normalized photoluminescence and CH_3Hg^+ concentration.

The results showed in Figure 5.7 indicated that the probe has a good response towards the presence of CH_3Hg^+ in the medium, but there is still margin for better results. For this reason, the experiments with CH_3Hg^+ were repeated using smaller concentrations of this ion in the probe working solution to find its limit of detection. The effect imposed by CH_3Hg^+ on the photoluminescence response of the probe was normalized as I_0/I (where I_0 is the original photoluminescence of the probe and I is the photoluminescence measured, at 616 nm, in the presence of CH_3Hg^+) and plotted in function of the concentration of CH_3Hg^+ . Results suggest that the tendency to increase suppression of the probe photoluminescent emission signal with the increase in the CH_3Hg^+ concentration is maintained (Figure 5.8A). The normalized analytical curve with the residual plot is shown in Figure 5.8B) and

presented linear behavior ($R^2 = 0.984$) within the tested concentration range (from 0.2 to 2.0 $\mu\text{g L}^{-1}$). The analytical curve equation was $L_0/L = 0.10319 \pm 0,00534 [\text{CH}_3\text{Hg}^+] + 0.99246 \pm 0,00426$. When using other models, such as polynomial or exponential, a better fitting is obtained ($R^2 = 0.996$) but it was chosen to use the linear model because of its simplicity. The instrumental limit of detection (instrumental LOD) was calculated as 0.059 $\mu\text{g L}^{-1}$ and the instrumental limit of quantification (instrumental LOQ), where a clear change in photoluminescence is observed, was 0.20 $\mu\text{g L}^{-1}$. Instrumental LOD and LOQ were calculated as the concentration of CH_3Hg^+ required to reduce the original luminescence intensity of the probe, respectively by $3 \times s_b$ and $10 \times s_b$, where s_b is the standard deviation of ten consecutive luminescence steady state (at 616 nm) measurements of the original probe. The LOD value is compatible with limit established by Brazilian CONAMA resolution 357/2005 [206] for total mercury content in waters (0.2 $\mu\text{g L}^{-1}$). However, if pre-concentration is applied (as discussed in the following sections) an improvement factor of 50 times is achieved making the LOQ of the method, in fact, 4 ng L^{-1} (considering correction due to the efficiency of extraction). Precision was evaluated as the coefficient of variation of the measured signals. Instrumental precision was obtained by performing ten measurements from a single probe solution containing a fixed concentration of CH_3Hg^+ . For CH_3Hg^+ concentrations of 0.3 $\mu\text{g L}^{-1}$ and 1.2 $\mu\text{g L}^{-1}$, results were 0.5 % and 0.8 %, respectively. Intermediate precision was obtained from two sets of ten independent probe solutions, where each set contained one different concentration of CH_3Hg^+ . For CH_3Hg^+ at 0.3 $\mu\text{g L}^{-1}$, intermediate precision was 1.3 % and for CH_3Hg^+ at 1.2 $\mu\text{g L}^{-1}$ intermediate precision was 1.5 %.

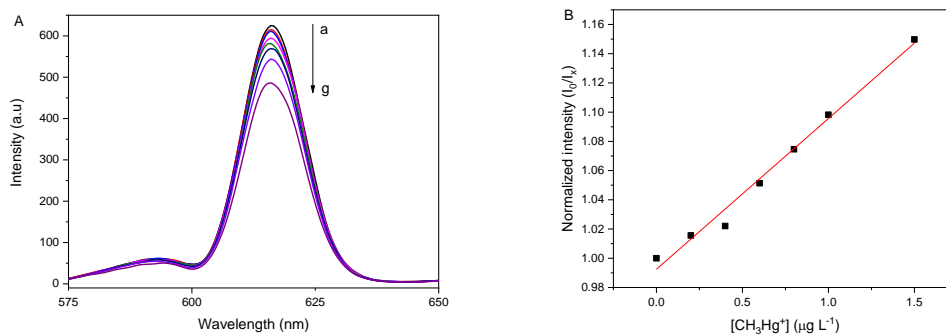


Figure 5.8 – (A) emission spectra with the photoluminescent responses of $[\text{Eu}(\text{tta})_4](\text{Et}_3\text{NH}^+)$ for concentrations of CH_3Hg^+ at a) 0, b) 0.2, c) 0.4, d) 0.6, e) 0.8, f) 1.0, g) 1.5 and h) 2.0 $\mu\text{g L}^{-1}$ and (B) graph of the linear relationship between normalized photoluminescent intensity and CH_3Hg^+ concentration.

5.2.11. Tests of different metal ions influence

The designed $[\text{Eu}(\text{tta})_4](\text{Et}_3\text{NH}^+)$ has four tta^- ligands shielding the Eu^{3+} ion from external influence of other metal ions but still allowing mercurial species bind to the sulfur atom in outer shell of the complex structure. The evaluation of the influence of the presence of other metal ions (Fe^{3+} , Mn^{2+} , Ca^{2+} , Li^+ , Mg^{2+} , Al^{3+} , Sn^{2+} , K^+ , Cr^{3+} , Ni^{2+} , Cd^{2+} , Na^+ , Pb^{2+} , Zn^{2+} , Ba^{2+} , Cu^{2+} and Co^{2+}) nearby the probe, $[\text{Eu}(\text{tta})_4](\text{Et}_3\text{NH}^+)$, was made and compared to the effect imposed by CH_3Hg^+ and Hg^{2+} on the measured photoluminescence. The concentration of the tested ions was fixed at 200 $\mu\text{g L}^{-1}$. Results (summarized in Figure 5.9A) indicated that all of the tested ions promoted a certain degree of photoluminescence quenching to about 60 to 80 % of the original photoluminescence. As a comparison, in the presence of Hg^{2+} and CH_3Hg^+ the photoluminescence measured was respectively decreased to about 55 % and 25 % of the original probe signal. When this test was performed at different concentrations, CH_3Hg^+ was still the one that caused the greatest photoluminescence quenching (Figure 5.9B). Values of about 15 % of the original probe signal for concentration were obtained for concentration of 1 mg L^{-1} and of about 91 % for concentration of 1 $\mu\text{g L}^{-1}$. It is important to point out that the degree of photoluminescence quenching does not follow the trend in changing the ionic strength (Figure 5.10) imposed for each of the salts tested (from $1 \times 10^{-5} \text{ mol L}^{-1}$ for CH_3Hg^+ to $9 \times 10^{-5} \text{ mol L}^{-1}$ for AlCl_3), indicating that photoluminescence was not necessarily affected by changes in ionic strength of the medium after addition

of the interferent in the form of salt solution. In this way, since there was not a trend in ionic strength for the photoluminescence quenching, we can also say that the anions used in this study (Cl^- , NO_3^- and SO_4^{2-}) have no considerable effect on the photoluminescence either.

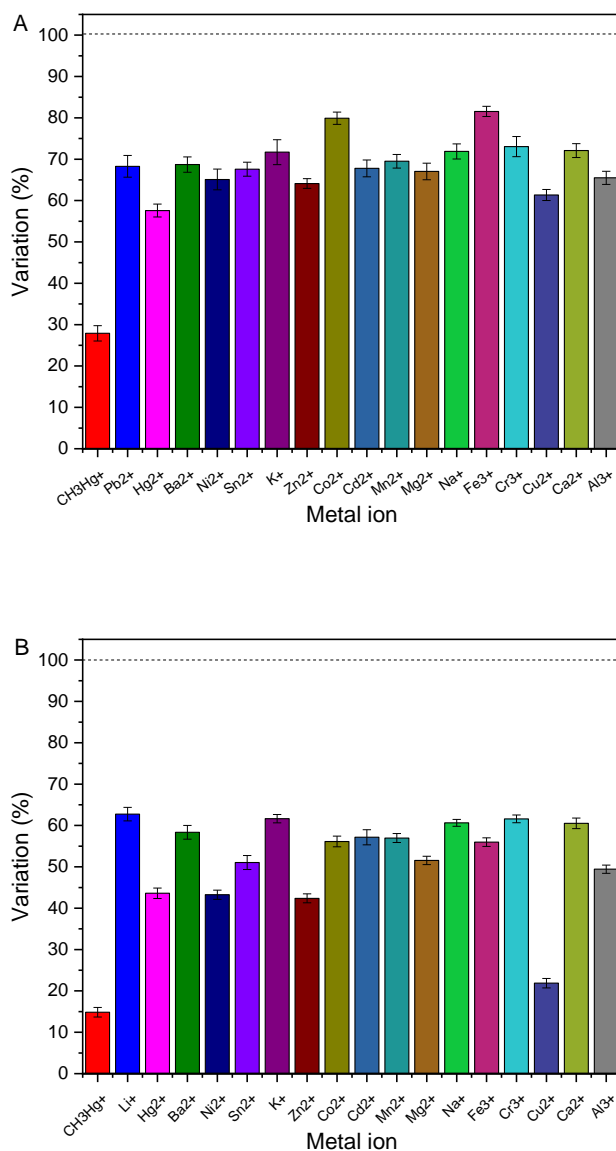


Figure 5.9 - Column graph of photoluminescent variation in the presence of different metal ions at A) 200 µg L⁻¹ and B) 1 mg L⁻¹; error bars are the standard deviation of three replicates.

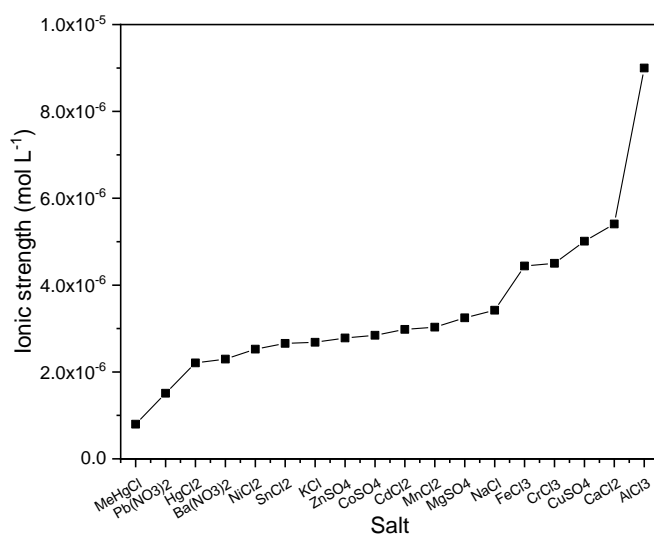


Figure 5.10 - Ionic strength of the different salts in the probe solution.

5.2.12.

Application in pre-concentrated CH_3Hg^+ in water and in PW samples

The probe was tested in the determination of CH_3Hg^+ in water and in PW samples. In order to guarantee high selectivity towards CH_3Hg^+ , a simple liquid-liquid extraction procedure was performed using dichloromethane as the extraction solvent. As CH_3Hg^+ tends to have favorable partition towards organic solvents, the extraction is an additional factor to increase selectivity related to other metal ions. It is important to point out that organic interferences should be considered when using the method in real samples, not simulated ones. Extraction efficiency was evaluated based on 9 extractions made with solutions containing CH_3Hg^+ at 15, 30 and 45 ng L^{-1} (3 extractions for each concentration). Recoveries of CH_3Hg^+ in ultrapure water (control sample) was $92.9 \pm 1.2 \%$ while in PW samples the extraction efficiency was $78.6 \pm 1.8 \%$. Residual concentrations of Hg^{2+} in the aqueous solution, after the extraction procedure of the PW samples, was about 20 ng L^{-1} (measured by CV-AAS) indicating that most of the also added inorganic mercury remained in the aqueous phase with the other fraction probably lost due to reduction to Hg^0 under the experimental conditions and ambient light. Extraction procedure allowed a pre-concentration of 50 times. The analysis using the proposed photoluminescent probe enabled the recovered results shown in Table 5.2 (corrected by the extraction

efficiency factor), confirming the efficiency of the extraction process in removing interfering substances and allowing the detection of CH_3Hg^+ at low concentrations due to the pre-concentration of analyte.

The CH_3Hg^+ in PW samples were also determined by the CV-AAS method using UV photo-degradation of CH_3Hg^+ to obtain total mercury and indirectly calculate original CH_3Hg^+ concentration. The recovery results, also shown in Table 5.2, were statistically equal to the ones obtained using the proposed method by employing a two-tail Student's t-test (95 % confidence limit at $n_1 = n_2 = 5$).

5.2.13. Interaction of CH_3Hg^+ with probe

As CH_3Hg^+ has a strong affinity to sulfur, of the thiophene groups, it affects spin-orbital coupling (the so-called heavy atom effect) favoring energy transfer of the excited complex population to the triplet state, from where non-radiative deactivation is favored in liquid solution. In contrast, Yang, Yook and Tae [207] reported a fluorescent change on a chemodosimeter associated with a mercury-promoted desulfurization reaction thanks to such a strong thiophilic affinity to mercury. A desulfurization process might occur when CH_3Hg^+ reacts with the complex, removing S atoms from tta^- ligands, thus opening the ligand molecular cycle. This process could affect the efficiency of the ligand to act as an antenna (reduction in the efficiency of ligand-metal energy transfer) resulting in the decreasing of the measured photoluminescence.

Table 5.2 - Analysis results (CH_3Hg^+ recoveries) from fortified control water and PW samples using the proposed method (photoluminescent probe) and CV-AAS after extraction and pre-concentration.

CH_3Hg^+ (ng L^{-1})	Recovery of CH_3Hg^+ in control water ($\text{ng L}^{-1} \pm \text{RSD}$) by photoluminescent probe	Recovery of CH_3Hg^+ in control water ($\text{ng L}^{-1} \pm \text{RSD}$) by CV-AAS	Recovery of CH_3Hg^+ in PW ($\text{ng L}^{-1} \pm \text{RSD}$) by photoluminescent probe	Recovery of CH_3Hg^+ in PW ($\text{ng L}^{-1} \pm \text{RSD}$) by CV-AAS	Student $t_{\text{experimental}}$ value for control water samples	Student $t_{\text{experimental}}$ value for PW samples
15	13.8 ± 0.02 (91.9 %)	14.8 ± 0.02 (99.0 %)	14.5 ± 0.02 (96.7 %)	14.8 ± 0.01 (91.8 %)	1.604	0.1080
30	25.8 ± 0.1 (86.1 %)	30.1 ± 0.1 (100.5 %)	25.7 ± 0.01 (85.7 %)	28.0 ± 0.04 (93.3 %)	1.770	1.840
45	47.4 ± 0.2 (105.2 %)	43.1 ± 0.4 (95.7 %)	42.2 ± 0.03 (93.9 %)	43.3 ± 0.06 (96.1 %)	0.6191	0.5331

$t_{\text{critical}} = 2.776$

5.3. Partial conclusions

An Eu(III) β -diketonate complex was synthesized through a new and simple synthetic route and used as an analytical probe for mercurial species (in this case CH_3Hg^+) as mercury effectively interact with sulfur of the tta^- ligand surrounding the lanthanide ion, thus quenching the characteristic $^5\text{D}_0 \rightarrow ^7\text{F}_2$ Eu(III) transition (at 616 nm). Besides the selective interaction with tta^- , the pH of the probe is kept near neutrality in order to disfavor the stability of other metal ions in the medium, favoring selectivity towards CH_3Hg^+ . The use of a simple liquid-liquid extraction, besides improving selectivity, allowed 50 times pre-concentration, enabling detection of CH_3Hg^+ concentrations down to the ng L^{-1} range. Analytical results obtained using PW samples were found to agree with the ones obtained by CV-AAS (after UV photo-derivatizations to obtain the CH_3Hg^+ concentration through the difference between total and inorganic mercury content).

6

Photoluminometric determination of formaldehyde in milk using microextraction on a single-drop of aqueous dispersion of silver-modified nitrogen doped graphene quantum dots

Manuscript submitted for publication in *Analytica Chimica Acta* as “*Silver-modified nitrogen doped graphene quantum dots sensor for formaldehyde in milk using headspace microextraction on a single-drop of aqueous dispersion*” Juliana da S. Padilha, Marlin J. Pedrozo-Penafiel, Anna De Falco, Dunieskys R. G. Larrudé, Marcelo E. H. Maia da Costa, Ricardo Q. Aucelio.

6.1.

Analytical method to determine formaldehyde in milk

In this chapter, a method to determine formaldehyde in milk is presented. An aqueous dispersion of amino-functionalized silver-modified GQDs was produced and its photoluminescence was found to be sensitive as it interacts with formaldehyde. These results lead to the development of a method, which relied on sampling of formaldehyde vapor using a drop of the nanomaterial dispersion hung onto the headspace above the milk sample. After interaction, the drop (probe) was diluted in an aqueous system to measure photoluminescence.

Current methods reported in the literature for the determination of formaldehyde based on the use of GQDs are based on the addition of the whole sample into the aqueous GQDs dispersion, thus they are limited to simple samples (in general simple aqueous matrices), also requiring long periods of equilibrium time to allow effective interaction between the analyte and these GQDs. Aiming high selectivity and virtually no sample preparation, the method presented in this chapter is a simpler option to detect formaldehyde contamination in milk.

6.2. Results and discussion

6.2.1. Preliminary results concerning the production of GQDs and their interaction with formaldehyde

Nitrogen doped GQDs (N-GQDs) were prepared through pyrolysis of citric acid and urea followed by hydro-exfoliation in ultrapure water. These N-GQDs were tested as photoluminescent probes for formaldehyde detection by adding formaline solution micro-volume aliquot (at different concentrations from 12 to 385 g L⁻¹) directly into the working probe dispersion. Results showed that no matter the concentration used, formaldehyde interacted with N-GQDs but required some time to achieve equilibrium and reach final stable quenched photoluminescence (Figure 6.1).

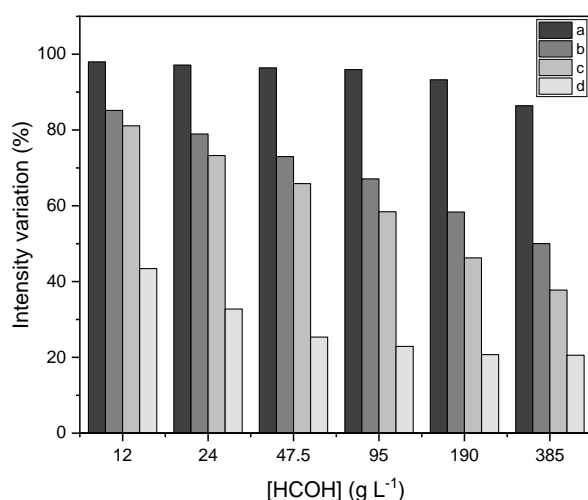


Figure 6.1 – Photoluminescent quenching of N-GQDs probe in the presence of formaldehyde solution at different concentrations over (a) 0, (b) 1, (c) 3 and (d) 24 h.

A further test was made with formaldehyde vapor where a drop of N-GQDs dispersion and a drop of formaldehyde were placed, apart from each other by 2 cm, in Petri dish. After sealing the Petri dish, it was placed in an oven (set at 37 °C) for 15 min. Then, the N-GQDs dispersion drop was collected and dispersed in water for photoluminescent measurements and results showed quenching of the N-GQDs photoluminescence, suggesting that the N-GQDs were able to interact with formaldehyde vapor (Figure 6.2A). The test with formaldehyde vapor was repeated

using the micro-extraction of formaldehyde vapor on a single drop hung over the aqueous sample headspace vial, simulating a HS-SDME procedure. Formaline solutions at 1.5; 3.0 and 6.0 g L⁻¹ were tested and results indicated photoluminescence quenching only for concentration of 6.0 g L⁻¹ (Figure 6.2B). Even though the results for the tests concerning N-GQDs with formaldehyde were promising, response was observed only at high concentrations of formaldehyde. When it comes to the stability tests of the N-GQDs dispersion, photoluminescence was only stable for a few days and therefore new attempts to prepare GQDs were made.

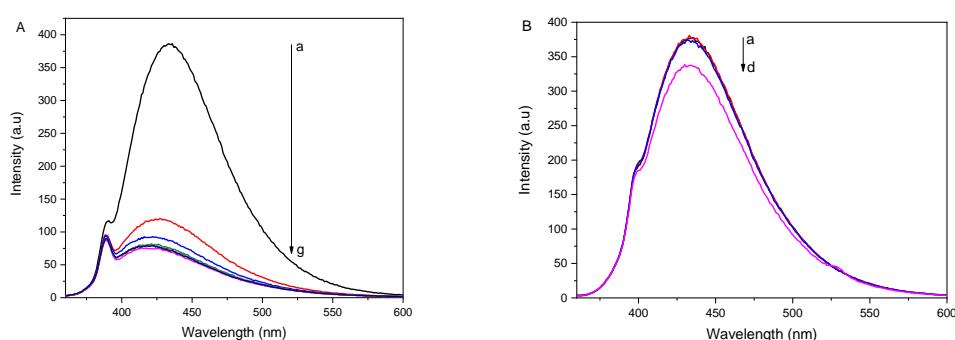


Figure 6.2 – Photoluminescent quenching of N-GQDs probe in the presence of formaldehyde vapor when tests were made (A) in a sealed Petri dish with concentrations at (a) 0, (b) 12, (c) 24, (d) 47.5, (e) 95, (f) 190 and (g) 385 g L⁻¹; (B) using the HS-SDME with concentrations at (a) 0, (b) 1.5, (c) 3.0 and (d) 6.0 g L⁻¹.

The N-GQDs prepared by the direct hydro-exfoliation of the molten precursors either in Tollen's reagent solution (Ag modification) or in Benedict's reagent solution (Cu modification) had their photoluminescence intensities (measured in aqueous dispersion) monitored over time and results showed that they were also stable for only a few days, when their photoluminescence significantly decreases. The effect arising from the interaction with formaldehyde, added as formalin solution, were evaluated and quenching of photoluminescence measured from the nanoparticle dispersions, were observed only at high concentrations of formaldehyde (above 1.5 g L⁻¹). The N-GQDs modified with silver were relatively more sensitive towards formaldehyde than the ones modified with copper. Therefore, further studies were made with N-GQDs modified with Ag prepared by refluxing the mixture of precursors in solution with Tollen's reagent whose

photoluminescence were found to be more stable, intense and more sensitive towards formaldehyde.

6.2.2. Factors influencing photoluminescence

A study of experimental parameters was carried out in order to obtain a stable and intense signal from the N-GQDs-Ag aqueous dispersion that allowed a reliable analytical response.

6.2.2.1. Study of stability in function of time

The stability of the N-GQDs-Ag photoluminescence was studied as a function of time, by monitoring the steady emission intensity measured from the dispersion, placed on a cuvette, every 5 min over a 60 min time interval. Within this time interval, luminescence remained stable where only a small arbitrary variation of about 2 % was observed.

6.2.2.2. Study of temperature influence

The influence of temperature on the photoluminescence, measured from the N-GQDs-Ag dispersion, was studied and a linear and inversely proportional relationship ($R^2 = 0.990$) was found within the tested interval (20 °C – 40 °C) with a decrease of approximately 35 % of signal intensity as the temperature reached 40 °C, probably due to non-radiative energy losses by vibration of the more loose substituent groups at the nanomaterial surface. As the temperature was reversed back to 20 °C, the measured photoluminescence was re-established to their original intensity (Figure 6.3) with no band spectral shifting observed.

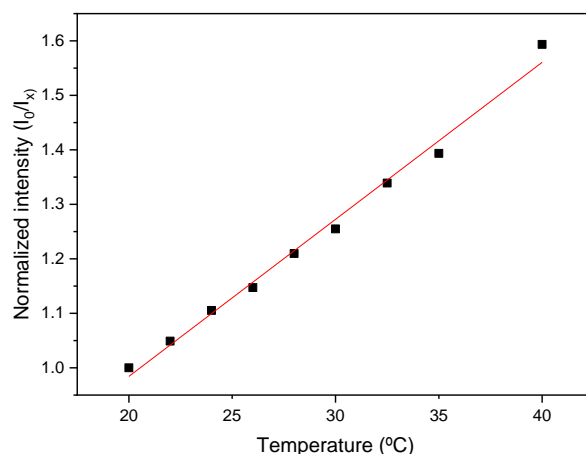


Figure 6.3 - N-GQDs-Ag emission intensity changes at different temperatures.

6.2.2.3. Study of pH influence

The effect of pH was evaluated taking as a reference the photoluminescence intensity measured at pH 6.7 (the original N-GQDs-Ag after 1000 times dilution with water). The pH of the dispersion was varied between 3.0 and 10.0 using aliquots of either HNO₃ or NaOH (at 1.0×10^{-2} mol L⁻¹). It was observed that the greater the acidity of the N-GQDs-Ag dispersion, the greater the suppression of photoluminescence (larger normalized I_0/I values) within the pH range between 3.0 and 4.0 (Figure 6.4). However, within the pH range between 6.0 and 9.0, photoluminescence intensity remained constant and no spectral shifting was observed. These results are in agreement with the results from the ζ -potential study, showing that at lower values of pH (3-5) the N atoms are protonated due to the larger concentration of H⁺ ions present in the medium, which prevents the transfer of lone pair of electrons to the graphene core structure, causing the decreasing of excitonic recombination and, therefore, luminescence intensity of N-GQDs-Ag. In contrast, at higher pH values (between 6 and 10), due to the lack of H⁺ ions in the medium, luminescent intensity of N-GQDs-Ag remained stable because there is no competition for the lone pair of electrons from N atoms. It is interesting that even at high pH values no oxidation of Ag (with formation of AgOH and ultimately of Ag₂O) was observed as silver is stabilized by the interaction with N-GQDs. Results suggest that as an analytical probe, the N-GQDs-Ag dispersion could be used

without any care upon pH adjustment as the photoluminescence was found to be a robust parameter within pH 5.0 and 10.0.

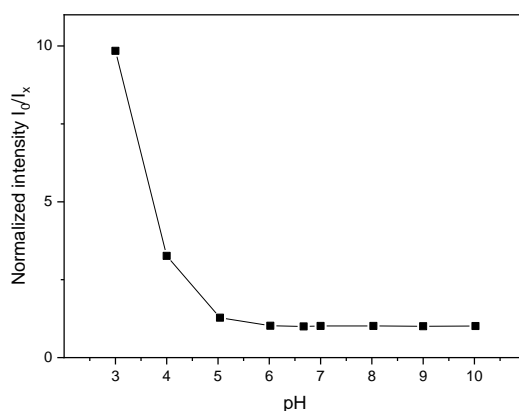


Figure 6.4 - N-GQDs-Ag emission intensity changes at different pH.

6.2.2.4. Study of UV radiation influence

The continuous exposition to the excitation radiation (at 349 nm) was also evaluated as these might affect N-GQDs-Ag photoluminescence stability. In this study, the kinetic mode of the photoluminescence spectrophotometer was used to continuously measure photoluminescence during 6 min. It was observed a small systematic decreasing of intensity under 2.5 % or 3.8 arbitrary units min^{-1} , indicating enough stability to perform photoluminescence measurements as scanning that takes less than 1 min to perform.

6.2.3. N-GQDs photoluminescence quenching induced by formaldehyde

After the experimental conditions of the analytical probe were determined (Table 6.1), it was possible to evaluate the effects of formaldehyde in the photoluminescent intensity of the N-GQDs-Ag probe. Investigation showed that their interaction produces photoluminescence quenching and this effect was studied to establish a quantitative relationship with formaldehyde using the Stern-Volmer like model, where the photoluminescence of the probe in the presence of formaldehyde (I) was normalized with the probe signal in the absence of formaldehyde (I_0), with increase in the analyte concentration.

Table 6.1 - Experimental conditions for formaldehyde determination.

Experimental parameter	Optimized value
Type of GQDs	N-GQDs-Ag
pH	6.7 (original pH of dispersion)
Temperature	25 °C
Volume of dispersion for drop	5 μ L
Final volume after dilution	3 mL

6.2.3.1.

Preliminary studies of the interaction between formaldehyde and N-GQDs-Ag

In the preliminary studies, an aliquot of formaldehyde solution was mixed with the luminescent N-GQDs-Ag working dispersion (in order to get a final analyte concentration of $1.5 \times 10^{-4} \text{ g L}^{-1}$) and quenching of photoluminescence was observed and monitored over time (1 – 30 min). Photoluminescent intensity kept decreasing over the monitored time (Figure 6.5A) and further investigation showed that signal decreasing was noticed even after 4 h of the mixing. The test was repeated for different final concentrations of formaldehyde (from 1.5×10^{-3} to 1.5 g L^{-1}) and the higher the concentration of formaldehyde added to the medium, the faster was the photoluminescence quenching since there were more formaldehyde molecules available to interact with the nanoparticles in dispersion. While concentrations of $1.5 \times 10^{-3} \text{ g L}^{-1}$ and $1.5 \times 10^{-2} \text{ g L}^{-1}$ led to about 50 % of the original dispersion signal (before addition of formaldehyde) after 4 h, higher analyte concentrations resulted in a final photoluminescence intensity of about 40 % (for $1.5 \times 10^{-1} \text{ g L}^{-1}$) and 20 % (for 1.5 g L^{-1}) of the original dispersion signal after 3 h, when stabilization was observed.

The test was repeated by probing formaldehyde as vapor in the headspace of a sample vial, using a hanging drop (5 μ L) of N-GQDs-Ag dispersion. The goal of the experiment was to concentrate formaldehyde in a micro-volume of dispersion, aiming to achieve a high formaldehyde/nanoparticle ratio that would produce an effective interaction, also producing a fast photoluminescence quenching. Besides providing a concentration of the analyte, the use of a hanging drop is a way to probe the analyte in gas phase where most of other components (from sample matrix) would not impose interferences. In this sense, the approach used was a headspace

single drop microextraction (HS-SDME). By hanging a single drop over a 1.5 g L^{-1} formaldehyde aqueous solution, during periods of time between 1 and 30 min, before retrieving the drop into the syringe and immediately placing it into water to measure photoluminescence, an effective quenching (to about 35 % of the original dispersion signal) was observed no matter the time exposed to the headspace (Figure 6.5B). Similar immediate quenching, reaching a stable signal level, was also observed when the single drop was hung over more diluted formaldehyde solutions, with quenching varying from 45 % ($1.5 \times 10^{-1} \text{ g L}^{-1}$) and 98 % ($1.5 \times 10^{-3} \text{ g L}^{-1}$) of the original signal.

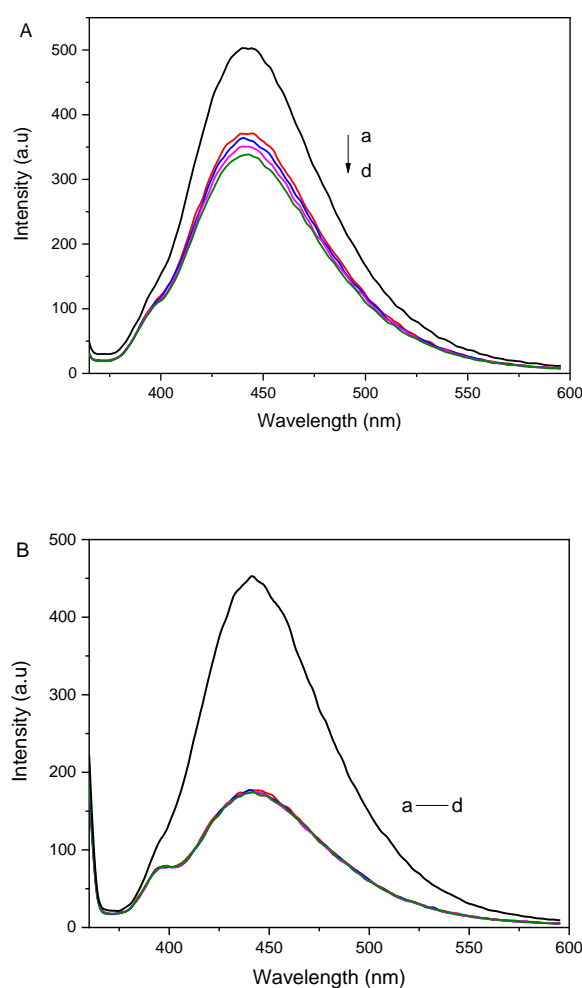


Figure 6.5 - N-GQDs-Ag emission intensity changes at different times after contact with: (A) formaldehyde solution at concentration of $1.5 \times 10^{-4} \text{ g L}^{-1}$ after (a) 1 minute, (b) 10 minutes, (c) 20 minutes and (d) 30 minutes and (B) formaldehyde vapor; (B) formaldehyde vapor from a 1.5 g L^{-1} solution after (a) 1 minute, (b) 10 minutes, (c) 20 minutes and (d) 30 minutes.

6.2.3.2.

Effect of temperature upon the interaction of N-GQDs-Ag and formaldehyde

In order to understand the mechanism between N-GQDs-Ag and formaldehyde, a study was performed at different temperatures (from 25 °C to 32.5 °C) with increasing concentrations of analyte. Normalized signal variation, I_0/I , was used to present the body of results (where I_0 is the dispersion fluorescence measured in absence of formaldehyde and I was fluorescence measured after interaction with the analyte). First, formaldehyde was added as solution into the aqueous dispersion to be measured at a fixed temperature (2 min after mixing). Besides the obvious inverse relationship between quenching of signal intensity and concentration of formaldehyde, the higher the temperature the stronger the quenching (higher I_0/I value) for a specific concentration of analyte (Figure 6.6A). In addition, a positive deviation of linearity was found due to the more effective quenching at higher concentrations of formaldehyde. This type of polynomial shape indicated a mixing of dynamic and static processes working together to produce overall quenching.

The experiment was also made using HS-SDME by keeping the temperature of the sample at different temperatures (25 to 40 °C) while the drop was exposed to the sample headspace for 5 min. After retrieving the drop into the syringe, it was then diluted with water to perform fluorescence measurement at 25 °C. It was observed that as the headspace temperature increased, the fluorescence quenching improved (higher I_0/I values) reflecting the increasing of formaldehyde concentration in sample headspace (Figure 6.6B). As observed before, when sampling of vapor was used, a linear relationship was found between normalized signal quenching and concentration of formaldehyde in sample, showing the importance of controlling temperature during sampling as well as during fluorescence measurements.

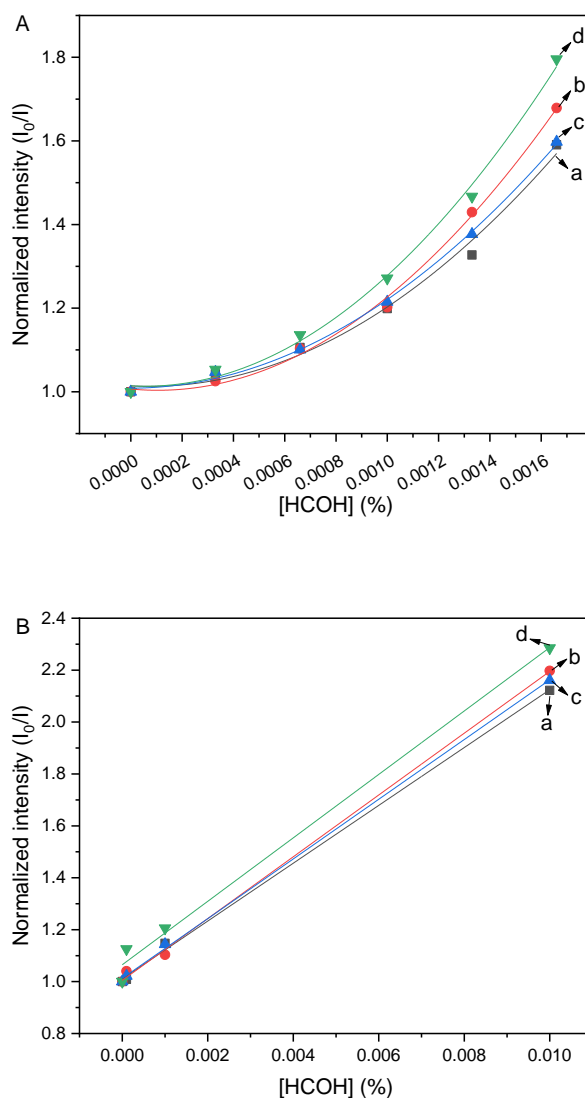


Figure 6.6 - Effects of temperature in N-GQDs-Ag photoluminescence intensity in the presence of formaldehyde at different concentrations in (A) solution at (a) 25, (b) 27.5, (c) 30 and (d) 32.5 °C; and (B) vapor at (a) 25, (b) 30, (c) 35 and (d) 40 °C.

6.2.3.3.

Analytical sensing of formaldehyde using N-GQDs-Ag dispersion as probe

The analytical response of the N-GQDs-Ag probe towards formaldehyde, using the HS-SDME approach, was evaluated using aqueous standards (1 mL) of increasing concentrations of formaldehyde (1.0×10^{-2} to 1.0×10^{-1} g L⁻¹). The sequence of photoluminescence spectra and the normalized analytical curve (Stern-Volmer curve), covering the tested concentration range, are shown in Figure 6.7, along with the residual plot, in detail, that shows a random distribution of residues

that indicate linear behavior and homoscedasticity of data. The response presented a determination coefficient (R^2) of 0.986, which is very adequate considering the two orders of magnitude of concentration. The model equation was $I_0/I = (125.50 \pm 7.40) [\text{HCOH}] + (1.00 \pm 0.04)$. From this response pattern, the instrumental limit of detection (instrumental LOD) value was $5.5 \times 10^{-3} \text{ g L}^{-1}$, calculated based on the concentration of formaldehyde required to produce a decreasing of the original photoluminescence of the probe (drop not exposed to formaldehyde) equivalent to three times (LOD).

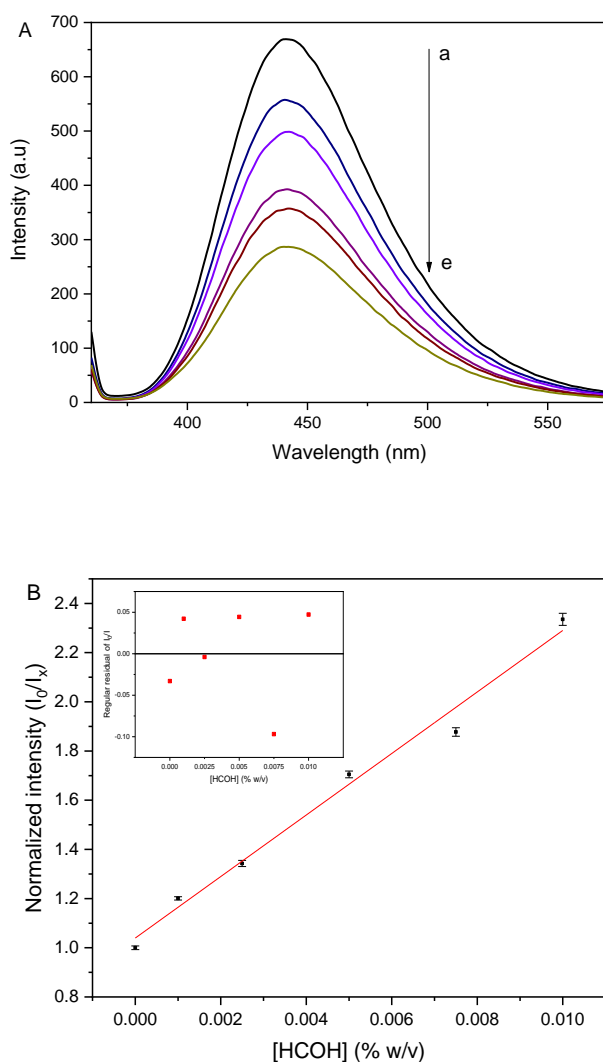


Figure 6.7 - (A) N-GQDs-Ag response towards increasing concentrations of formaldehyde vapor: (a) 0, (b) 1.0×10^{-2} , (c) 2.5×10^{-2} , (d) 5.0×10^{-2} , (e) 7.5×10^{-2} and (f) $1.0 \times 10^{-1} \text{ g L}^{-1}$. (B) Linear relationship between normalized photoluminescent intensity and formaldehyde concentration.

Reproducibility was estimated after sampling formaldehyde in the drop and diluting it in water then performing ten consecutive photoluminescence measurements. The test was made using vapor sampling from formaldehyde solutions at concentrations of $1.0 \times 10^{-2} \text{ g L}^{-1}$ and $1.0 \times 10^{-1} \text{ g L}^{-1}$ and results were 0.56 % and 1.81 % in terms of standard deviation of the signal measured. Intermediate precision was obtained by performing vapor sampling in three sets of ten independent formaldehyde solutions (each set containing one different concentration of formaldehyde) and then measuring photoluminescence after dilution of the dispersion drop in water. The precision was the standard deviation of the normalized signal ratio ($s_{I_0/I}$), considering the propagation of standard deviations s_{I_0} and s_I , which are respectively the ones from the measured set before and after contact with formaldehyde: $s_{I_0/I} = I_0/I \times [(s_{I_0}/I_0)^2 + (s_I/I)^2]^{1/2}$. For concentrations of formaldehyde generated from aqueous solutions at concentrations of $1.0 \times 10^{-2} \text{ g L}^{-1}$ and $1.0 \times 10^{-1} \text{ g L}^{-1}$ reproducibility were 0.65 % and 1.92 %.

6.2.3.4. Interference of hydrogen peroxide

H_2O_2 is known to be used as a preservative in milk because it activates the lactoperoxidase enzyme system. By preventing the proliferation of microorganisms, the quality of raw milk is improved [208-210]. In some countries this practice is permitted but not in Brazil [189]. Due to the fast deterioration of H_2O_2 , which makes its detection challenging, sometimes it is used as an adulterant in raw milk.

As hydrogen peroxide is another common adulterant in milk, the effect of the presence of H_2O_2 in the sample was evaluated as it may decompose, increasing the concentration of formic acid in sample headspace [66] First, milk samples were fortified with H_2O_2 (at concentrations of $2.0 \times 10^{-2} \text{ g L}^{-1}$, $2.0 \times 10^{-1} \text{ g L}^{-1}$ and $2.0 \times 10^1 \text{ g L}^{-1}$) before using in the HS-SDME procedure. It was observed no interference as the probe signal was not affected. In a second experiment, the test was repeated in the presence of formaldehyde (at 1.0×10^{-2} and $1.0 \times 10^{-1} \text{ g L}^{-1}$) and no interference was observed when concentration of H_2O_2 was $2.0 \times 10^{-2} \text{ g L}^{-1}$, even at lower concentration of formaldehyde, not affecting the signal measured after diluting the N-GQDs-Ag probe in water. However, when higher concentrations of

H_2O_2 ($2.0 \times 10^{-1} \text{ g L}^{-1}$ and 2.0 g L^{-1}) were present, there was an interaction with formaldehyde in solution, decreasing analyte concentration as vapor, reflecting in the interaction with the N-GQDs-Ag probe (quenching less effective than the one expected in absence of H_2O_2). In this case, the probe can still be used to indicate that milk is adulterated with formaldehyde (qualitative indication).

6.2.3.5.

Application of the method in milk samples

The method was tested by determining formaldehyde in different types of milk samples (whole, semi-skimmed and skimmed). Depending on the type of milk, the only sample treatment was a simple dilution with water (2-fold for whole milk, 1-fold for semi-skimmed milk while no dilution was required for skimmed milk). As formaldehyde was not detected in preliminary measurements, samples were fortified by adding micro-volumes of a previously titrated formalin solution, in order to achieve final concentrations of $1.0 \times 10^{-3} \text{ g L}^{-1}$, $1.0 \times 10^{-2} \text{ g L}^{-1}$ and $1.0 \times 10^{-1} \text{ g L}^{-1}$.

For the application of the proposed method, aliquots of 1.00 mL of samples were placed inside the glass vial where the syringe needle was inserted, through the rubber septum, in order to perform the HS-SDME procedure with the hanging N-GQDs-Ag dispersion drop. Quantification was made by interpolation of the experimental results into the analytical curve previously constructed using formaldehyde standards, prepared by diluting, in water, proper aliquots of a titrated formalin solution. Standards were also submitted to the HS-SDME procedure before re-dissolution in the N-GQDs-Ag probe dispersion for photoluminescence measurement and results are shown in Table 6.2.

Based on the recovered results (percent recoveries within 93 and 110 %) the method was found to be efficient in determining formaldehyde content at $1 \times 10^{-2} \text{ g L}^{-1}$ and at $1 \times 10^{-3} \text{ g L}^{-1}$. In contrast, recovered levels for samples containing $1 \times 10^{-1} \text{ g L}^{-1}$ of formaldehyde were affected, leading to percent recoveries between 59 % and 75 % depending on the type of milk. There are three possible reasons that can be influencing this behavior, perhaps in association. First, as recoveries were relatively better (about 75 %) for samples with less fat (skimmed milk), the volatilization of formaldehyde may be hindered, not leading to a proportional

quantity in the form of vapor in headspace of sample vial. Another possibility is that the interaction between vapor and the hanging dispersion drop is being affected when higher concentrations of formaldehyde are present in the sample vial headspace. Finally, the lower recoveries may be caused during the photoluminescence measurement after dilution of the drop with water due to the instability of photoluminescence of quantum dots when higher concentrations of formaldehyde are present. It is important to point out that when samples with formaldehyde concentration at $1.0 \times 10^{-1} \text{ g L}^{-1}$ are 10 times diluted (final concentration of $1.0 \times 10^{-2} \text{ g L}^{-1}$) before HS-SDME procedure, recoveries are similar to the ones obtained for original formaldehyde concentration of $1.0 \times 10^{-2} \text{ g L}^{-1}$, indicating elimination of the interference caused in samples with formaldehyde concentration of $1.0 \times 10^{-1} \text{ g L}^{-1}$.

6.2.3.6. Comparative colorimetric method

The efficiency of the proposed photoluminescent method was compared with the chromotropic acid colorimetric method [143] that is adopted in the Brazilian legislation [142]. This legislation rejects any sample in which solutions, after distillation, produces color change. As expected, the sample blank solution (from non-fortified samples) produced the light brown color characteristic of the chromophore reagent. For the analyte fortified samples, the higher the formaldehyde concentration, the deeper the purple color of the distilled solution that indicated presence of increasing concentrations of formaldehyde (Figure 6.8). In comparison with the proposed photoluminescence-based method, it is appropriate suitable to say that the lower the formaldehyde concentration the smaller is the decreasing in luminescence from N-GQDs-Ag, while the higher the formaldehyde concentration the stronger is the photoluminescence suppression observed.



Figure 6.8 - Color variation of chromotropic acid solution after contact with the distilled solutions of milk samples fortified with formaldehyde at concentrations of (a) 0, (b) 1.0×10^{-3} , (c) 1.0×10^{-2} , (d) 1.0×10^{-1} and (e) 1.0 g L^{-1} .

6.2.3.7. Comparative chromatographic method

In order to compare the performance of the method, the formaldehyde content was determined in whole milk samples using the HPLC method based on the absorption photometric measurement after liquid-liquid extraction and chemical derivatization of formaldehyde with DNPH solution. Formaldehyde fortification was made at three levels in authentic replicates (1.0×10^{-3} , 1.0×10^{-2} and $1.0 \times 10^{-1} \text{ g L}^{-1}$). The obtained model equation was $Y = (32331.90 \pm 2115.32) [\text{HCOH}] + (9.41 \pm 11.88)$ with a good linear response ($R^2 = 0.987$). For the sample fortified at $1.0 \times 10^{-3} \text{ g L}^{-1}$, the analytical signal could not be detected and formaldehyde was not quantified. The obtained result, for the samples fortified at $1.0 \times 10^{-2} \text{ g L}^{-1}$, was $(9.9 \pm 0.2) \times 10^{-3} \text{ g L}^{-1}$ (99 % recovery) while $(1.1 \pm 0.03) \times 10^{-1} \text{ g L}^{-1}$ (110 % recovery) was achieved for the sample fortified at $1.0 \times 10^{-1} \text{ g L}^{-1}$.

Taking into consideration the results obtained for the whole milk samples, the proposed method and the chromatographic method were statistically compared (two-tail Student's t-test, with 95 % confidence limit at $n = 3$) in terms of quantitative performance, considering the sample fortified at $1.0 \times 10^{-2} \text{ g L}^{-1}$ with $t_{\text{calculated}} = 3.415$ and $t_{\text{critical}} = 2.776$. Statistical comparison for the other fortification levels could not be made as the HPLC method failed in quantifying formaldehyde at $1.0 \times 10^{-3} \text{ g L}^{-1}$ and the recovery of the proposed method was affected when determining samples with analyte content at $1.0 \times 10^{-1} \text{ g L}^{-1}$. After testing formaldehyde at $1.0 \times 10^{-1} \text{ g L}^{-1}$ with a 10-fold dilution, it was possible to make the statistical comparison with the chromatographic method with $t_{\text{calculated}} = 3.705$.

Table 6.2 - Recovery results for formaldehyde in different types of milk using the N-GQDs-Ag photoluminescent probe.

Concentration of formaldehyde (g L ⁻¹)	Whole powder milk (g L ⁻¹ ± RSD)	Whole milk (g L ⁻¹ ± RSD)	Whole 0 % lactose milk (g L ⁻¹ ± RSD)	Semi-skimmed milk (g L ⁻¹ ± RSD)	Skimmed milk (g L ⁻¹ ± RSD)
1.0 × 10 ⁻³	1.0 × 10 ⁻³ ± 3.3 × 10 ⁻⁵ (100.0 %)	1.1 × 10 ⁻³ ± 7.8 × 10 ⁻⁵ (110.0 %)	9.3 × 10 ⁻⁴ ± 3.1 × 10 ⁻⁵ (93.0 %)	9.7 × 10 ⁻⁴ ± 2.2 × 10 ⁻⁴ (97.0 %)	9.4 × 10 ⁻⁴ ± 1.2 × 10 ⁻⁴ (94.0 %)
1.0 × 10 ⁻²	1.1 × 10 ⁻² ± 6.0 × 10 ⁻⁵ (106.0 %)	9.9 × 10 ⁻³ ± 1.1 × 10 ⁻⁴ (99.0 %)	1.1 × 10 ⁻² ± 1.1 × 10 ⁻⁴ (105.0 %)	1.1 × 10 ⁻² ± 1.3 × 10 ⁻⁴ (106.0 %)	9.7 × 10 ⁻³ ± 6.1 × 10 ⁻⁵ (97.0 %)
1.0 × 10 ⁻¹	7.0 × 10 ⁻² ± 7.5 × 10 ⁻⁵ (70.0 %)	5.9 × 10 ⁻² ± 7.8 × 10 ⁻⁵ (59.0 %)	6.2 × 10 ⁻² ± 7.2 × 10 ⁻⁵ (62.0 %)	6.5 × 10 ⁻² ± 3.0 × 10 ⁻⁴ (65.0 %)	7.5 × 10 ⁻² ± 2.8 × 10 ⁻⁴ (75.0 %)
1.0 × 10 ⁻¹ (10× diluted)	9.6 × 10 ⁻³ ± 7.9 × 10 ⁻⁵ (96.0 %)	9.9 × 10 ⁻³ ± 8.4 × 10 ⁻⁵ (99.0 %)	9.9 × 10 ⁻³ ± 6.8 × 10 ⁻⁵ (99.0 %)	1.1 × 10 ⁻² ± 8.6 × 10 ⁻⁵ (105.0 %)	1.1 × 10 ⁻² ± 2.2 × 10 ⁻⁴ (106.0 %)

n = 3

6.3. Partial conclusion

Nitrogen-doped graphene quantum dots modified with silver (N-GQDs-Ag) were prepared by a hydrothermal refluxing route. Coordination of GQDs with amino groups in their surface and edges was indicated by XPS and FT-IR. Photoluminescent quenching of N-GQDs-Ag of both static and dynamic nature was achieved in the presence of formaldehyde and the nanoparticle dispersion was used as a photoluminescent analytical probe for the determination of formaldehyde vapor using the HS-SDME technique. The method was successfully applied in monitoring formaldehyde at low concentrations in commercial milk samples fortified with the analyte, where the milk samples did not need any previous treatment besides dilution when necessary. When compared with a HPLC method [163] that uses liquid-liquid extraction and derivatization of the analyte, the presented method showed better sensibility to formaldehyde at lower concentrations with LOD calculated to be $5.5 \times 10^{-3} \text{ g L}^{-1}$. The presented method showed to be a simpler way of monitoring formaldehyde, since it does not require any difficult and time-consuming sample preparation, sometimes with toxic chromophores, and can be used as an alternative to the methods based on chromatography or other methods described in the literature, especially the official method used in the Brazilian legislation [142], which is only qualitative. In this way, the presented method can benefit the society by helping to provide safer food for consumers.

7

Preliminary evaluation of $[\text{Eu}(\text{tta})_4](\text{Et}_3\text{NH}^+)$, N-GQDs-Ag and LASOC 460 as probes for temperature sensing

7.1.

Analytical method for temperature sensing

Photoluminescence from compounds and nanomaterials are usually sensitive to variations in temperature, often causing decrease of radiative efficiency. The extent of such effect is dependent upon the structure of the compounds and nanomaterials, the nature of the medium in which they are dispersed (viscosity of liquid medium, rigidity of a solid matrix for instance) and also due to the presence of concomitant species in the same environment. Based on all the information provided about the characteristics of the two different proposed luminophores in this dissertation, $[\text{Eu}(\text{tta})_4](\text{Et}_3\text{NH}^+)$ and N-GQDs-Ag, a preliminary study concerning their photoluminescence temperature-dependency was performed and compared to the behavior observed for an organic dye (the benzothiadiazole derivative coded LASOC 460, which displays aggregation-induced enhanced emission) recently synthesized at the LaSOQF-PUC-Rio, whose photoluminescence characteristics (not included temperature-dependency) has been recently reported [197].

Temperature sensing was studied in aqueous solutions, as well as after luminophores were immobilized into a polymer matrix (PCL, PMMA or PVA), within 25 °C and 40 °C, which is a temperature range ideal for *in vivo* or *in vitro* studies involving living cells. Results suggested that N-GQDs-Ag presented a better behavior in terms of sensitivity and reversibility of response. In this sense, a further toxicity study was performed, using *S. cerevisiae* cells, aiming future applications in biological studies.

A literature survey indicates that the use of luminophores as temperature sensors is still recent and the reports are not vast. Most of these luminophores (especially organic dyes) present inherent toxicity also requiring complex routes of synthesis usually based on the use of expensive precursors. The goal of this chapter

is to expand the number of luminophore candidates to be used as probes for temperature that circumvent limitations inherent of some of the ones reported in the literature.

7.2.

Evaluation of the $[\text{Eu}(\text{tta})_4](\text{Et}_3\text{NH}^+)$ complex as a temperature probe

The photoluminescence dependency of the $[\text{Eu}(\text{tta})_4](\text{Et}_3\text{NH}^+)$ complex was preliminary evaluated in solution, in Chapter 5, when studying characteristic of the complex in order to choose analytical probing conditions. Photoluminescence of the $[\text{Eu}(\text{tta})_4](\text{Et}_3\text{NH}^+)$ complex solution at the concentration of $5.0 \times 10^{-6} \text{ mol L}^{-1}$ (prepared in acetone/water 70/30 % v/v) was monitored in the electric dipole transition $^5\text{D}_0 \rightarrow ^7\text{F}_2$ of Eu^{3+} ions (616 nm). It was found that $[\text{Eu}(\text{tta})_4](\text{Et}_3\text{NH}^+)$ complex luminescence was sensitive within temperature interval between 20 °C and 30 °C with sensitivity of $3.2 \% \text{ } ^\circ\text{C}^{-1}$ or variation of signal of $-20 \text{ a.u. } ^\circ\text{C}^{-1}$ (Figure 7.1A). The linear relationship ($R^2 = 0.998$) can be found in Figure 7.1B. Within this temperature range, the complex was stable and the original photoluminescence was restored back when temperature was reversed back from 30 °C to 20 °C (Figure 5.5) in seven cycles of temperature variation. Due to the high proportions of acetone in the solvent system (highly volatile solvent), studies involving higher temperatures were avoided but attempts at 40 °C showed that reversibility to original signals, at 20 °C, resulted in about only 90 % of recovery probably related to incomplete thermalization due to the slow heat dissipation during the cooling process.

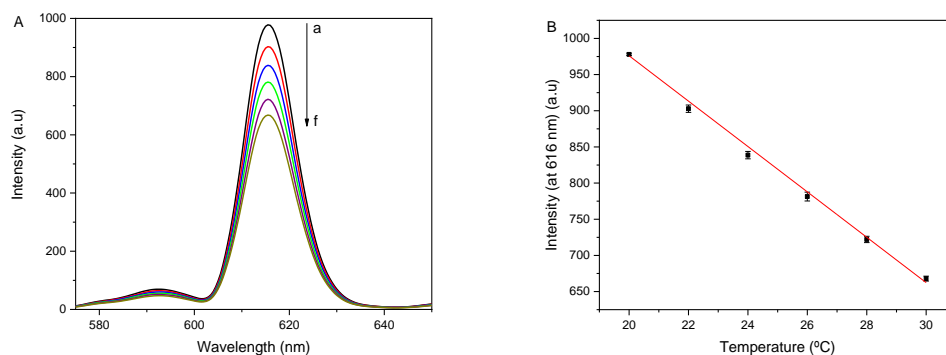


Figure 7.1 - (A) Fluorescence spectra of $[\text{Eu}(\text{tta})_4](\text{Et}_3\text{NH}^+)$ at the temperatures of (a) 20, (b) 22, (c) 24 and (d) 26, (e) 28 and (f) 30 °C. (B) Linear relationship between fluorescence intensity of $[\text{Eu}(\text{tta})_4](\text{Et}_3\text{NH}^+)$ and temperature.

It was previously reported [1] that the thermal quenching may be related to thermally activated non-radiative pathways, and regarding lanthanides, the partial loss of photoluminescence may be related to energy transfer, where the metal ion transfers part of the energy back to the ligand, in which a part decays non-radiatively [172].

The next step was to incorporate the $[\text{Eu}(\text{tta})_4](\text{Et}_3\text{NH}^+)$ complex into a polycaprolactone (PCL) matrix in order to evaluate the resultant film as a photoluminescent thermometer. PCL is a biocompatible, biodegradable polymer that is soluble in the same solvents as $[\text{Eu}(\text{tta})_4](\text{Et}_3\text{NH}^+)$. The image of this PCL-Eu(III) system under UV is shown in Figure 7.2.

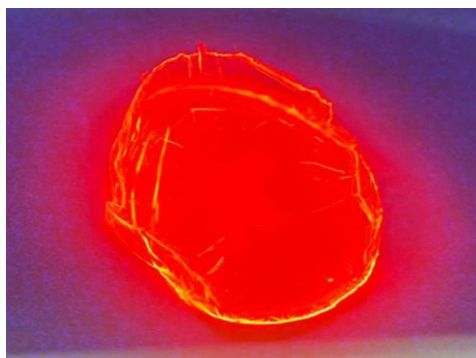


Figure 7.2 – Red emission of the PCL-Eu(III) system under UV.

The photoluminescent intensity variation of PCL-Eu(III) was also monitored at 616 nm using a rectangular piece of the produced PCL-Eu(III) film, with dimensions 3 cm vs 0.8 cm, which was immersed and fixed inside a quartz cuvette containing 3 mL of water (non-solvent for PCL) to help temperature homogenization, and photoluminescence measurements were made at the range from 25 °C to 40 °C, with 5 °C intervals. A similar behavior from tests in solution was observed, where a decrease (linear relationship with $R^2 = 0.996$) down to 48 % of the original photoluminescence intensity as temperature increased (Figure 7.3). The sensitivity of response was 3.5 % °C⁻¹ or -18 a.u. °C⁻¹.

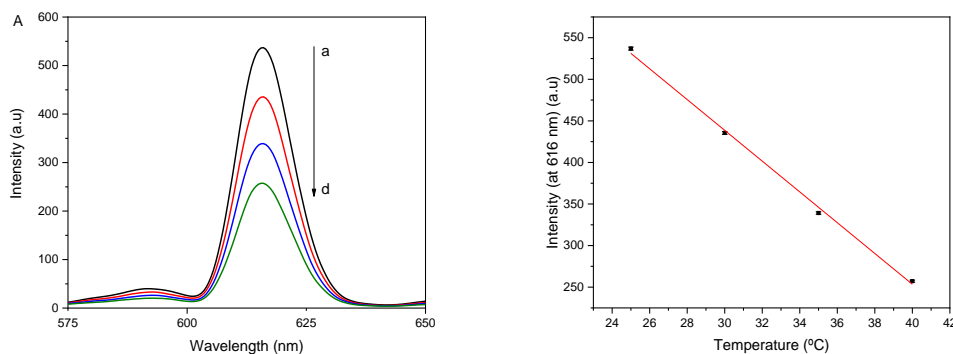


Figure 7.3 – (A) Fluorescence spectra of PCL-Eu(III) at the temperatures of (a) 25, (b) 30, (c) 35 and (d) 40 °C. (B) Linear relationship between fluorescence intensity of PCL-Eu(III) and temperature.

The effectiveness of the response reversibility of the probe (Figure 7.4A) was evaluated after three cycles of increasing and then decreasing the temperature within the range of 25 °C and 40 °C. It was found that right after the first cycle, photoluminescence did not return back to the original response of the film, due to a loss of about 25 % of fluorescence, decreasing sensitivity of the sensor from 18 a.u. °C⁻¹ to 11 a.u. °C⁻¹. This behavior confirmed the instability of the fluorophore at temperatures above 30 °C when working in solution. When the test was repeated within the 25 °C to 30 °C range in seven cycles (Figure 7.4B) the photoluminescence was completely restored along all cycles, showing the reusability of the doped film.

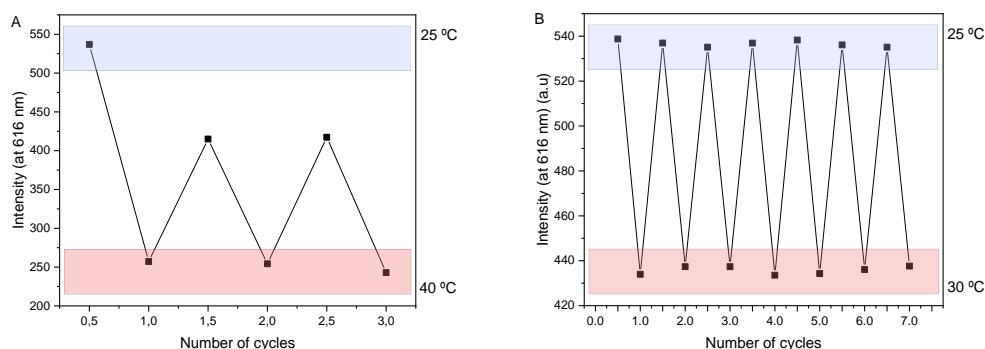


Figure 7.4 - Temperature optical sensing of PCL-EU(III) in (A) three cycles of temperature from 25 to 40 °C and (B) in seven cycles of temperature from 25 to 30 °C.

7.3. Evaluation of the organic dye LASOC 460 as a temperature probe

The fluorescent properties of LASOC 460 have been recently reported, showing that aggregation-induced enhanced emission (AIEE) occurs as the polarity of the solution increases, thus enhancing fluorescence by about 6 times, with a small hypsochromic shift in the maximum of the emission band [197]. The influence of temperature (from 20 °C to 40 °C range) affecting the fluorescence by the AIEE effect (measured at 420/565 nm) was also reported using a 5.0×10^{-6} mol L⁻¹ LASOC 460 solution in conditions that produced the aggregated form of the fluorophore (in ethanol/water 15/85 % v/v). It was found that the higher the temperature, the stronger the produced photoluminescence quenching as this phenomenon was related to molecular rotation. At higher temperatures, the molecule rotors are freer to rotate, promoting energy dissipation of excited state population by non-radiative processes.

Based on these results, a more detailed study was made, using a 5.0×10^{-6} mol L⁻¹ LASOC 460 in ethanol/water 15/85 % v/v (aggregated form), and the measured fluorescence, at 40 °C, was about 42 % of the one measured at 25 °C. A linear relationship ($R^2 = 0.996$) between the measured signal (peak height) and temperature was found with sensitivity of $-2,1 \text{ \% } ^\circ\text{C}^{-1}$ (or 19.5 a.u. $^\circ\text{C}^{-1}$). There was no significant spectral shift as temperature was varied and after heating, the reversing temperature back to 25 °C (one complete cycle of temperature variation) promoted a partial recovery of fluorescence (about only 60 % of the signal initially measured at 25°C), what indicated nanoaggregate instability and, consequently, loss of emission intensity. Therefore, no further temperature cycles were tested.

In order to evaluate the dye in the non-aggregated form, the solvent was switched to guarantee solubilization yet non-aggregation (less polar environment) also minimizing volatilization of solvent during experiment. In order to achieve this, tert-butyl alcohol was chosen to prepare the LASOC 460 solution at 5.0×10^{-6} mol L⁻¹. Under such conditions, the influence of temperature on the LASOC 460 fluorescence (from 25 °C to 40 °C) produced a completely different result compared to the one observed using the luminophore at the aggregated form. In this case, fluorescence of LASOC 460 linearly increased (about 8 %) with the increasing of temperature ($R^2 = 0.985$) along with a slightly blue-shift of 5 nm (from 575 nm to

570 nm) as seen in Figure 7.5. As temperature increased, solvation layer around the luminophore was decreased, making the solvent-luminophore interaction in the excited state weaker, which decreased non-radiative decays and favored emission enhancement and spectral blue shift. By varying temperature from 25 °C to 40 °C and back to 25 °C in seven cycles, it was observed that there was complete restoration of emission signal (at 25 °C) in all cycles of temperature variation, showing the stability and reusability of the luminophore.

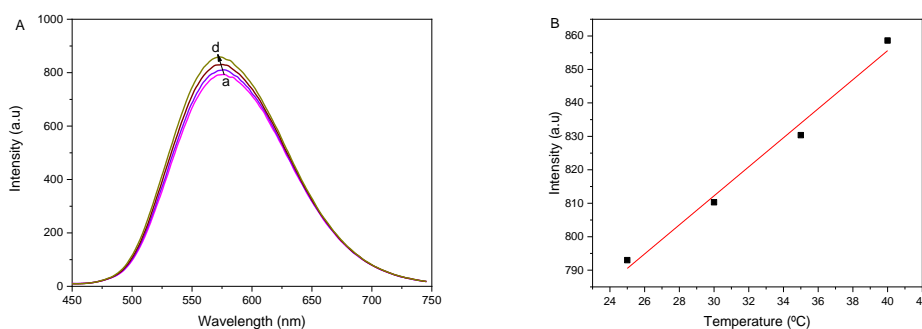


Figure 7.5 – (A) Fluorescence spectra of LASOC 460, in tert-butyl alcohol, at different temperatures: (a) 25, (b) 30, (c) 35 and (d) 40 °C. (B) Linear relationship between fluorescence intensity of LASOC 460 in function of temperature.

The incorporation of LASOC 460 in polymethyl methacrylate (PMMA) was made in order to evaluate the sensibility of the fluorophore in function of temperature. The green-yellow emission of the PMMA-LASOC 460 film under UV is shown in Figure 7.6.

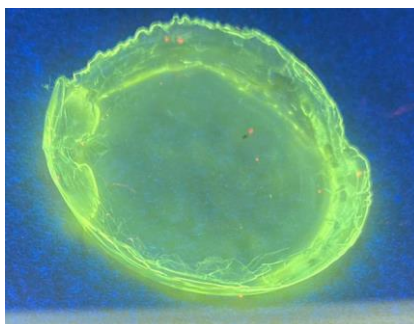


Figure 7.6 – Green-yellow emission of the PMMA-LASOC 460 system under UV.

The variation of fluorescence intensity, produced by the PMMA-LASOC 460 film, was monitored using the excitation at 420 nm. A piece (3 cm by 0.8 cm) of

the produced fluorophore film was placed inside a quartz cuvette containing 3 mL of water (non-solvent for PMMA). Fluorescence was measured within the temperature range from 25 to 40 °C (with 5 °C interval) and results (Figure 7.7) showed that in this temperature range, the expected fluorescence variation (in this case due to quenching) was not very effective (about only 5 %) with sensibility of $0.3 \% \text{ }^{\circ}\text{C}^{-1}$ ($-2.4 \text{ a.u. }^{\circ}\text{C}^{-1}$). Such a small fluorescence quenching indicates that the polymeric film made the dye structure more rigid, thus less prone for changing in molecular rotation of substituent groups. Contrary to what was expected, when temperature was increased to 50 °C, fluorescence increased probably due to PMMA becoming more flexible and allowing a certain degree of aggregation of the dye, which enhances photoluminescence intensity.

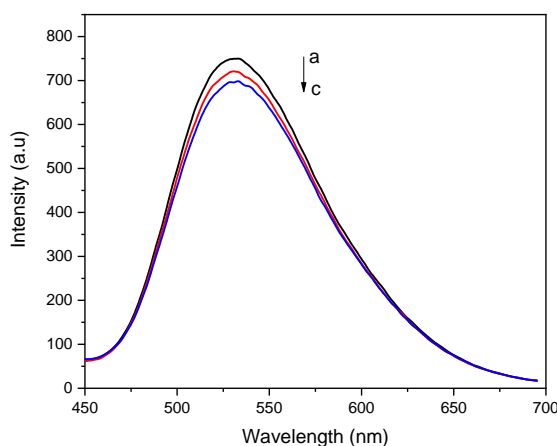


Figure 7.7 - Fluorescence spectra of PMMA-LASOC 460 at different temperatures: (a) 25, (b) 30, and (c) 40 °C.

As the film was submitted to seven consecutive temperature cycles (heating from 25 °C to 40 °C and then reversing back to 25 °C), the measured fluorescence was efficiently recovered (Figure 7.8) showing good stability and reusability of LASOC 460 in a PMMA film.

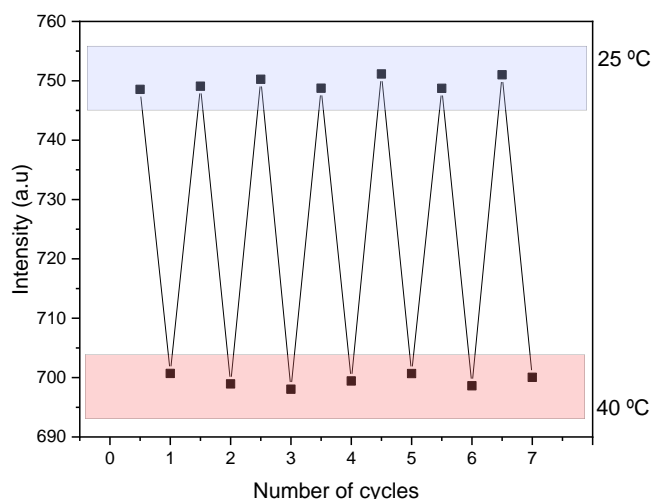


Figure 7.8 - Temperature sensing of PMMA-LASOC 460 in seven cycles of temperature from 25 °C to 40 °C.

7.4. Evaluation of the N-GQDs-Ag as a temperature probe

When evaluating the nature of quenching mechanism by formaldehyde, the photoluminescence of N-GQDs-Ag, measured from an aqueous dispersion (1000 times dilution of the original dispersion in water), was monitored at 349/441 nm at different temperatures within the range from 20 to 40 °C. Results, discussed in chapter 6, showed a linear and inversely proportional relationship ($R^2 = 0.990$) in the tested interval with a decrease of approximately 35 % of signal intensity as the temperature reached 40 °C, with no noticeable band spectral shifting. The signal variation was of $-15.6 \text{ a.u. } ^\circ\text{C}^{-1}$ ($1.9 \% \text{ } ^\circ\text{C}^{-1}$). In addition, as the temperature was reversed back to 20 °C, the measured photoluminescence was also recovered to its original intensity.

Further studies have shown that by varying temperature in this diluted N-GQDs-Ag aqueous dispersion from 25 to 50 °C (Figure 7.9A) then back to 25 °C, in seven cycles, it produced repeated restoration of original photoluminescence (the one measured initially at 25 °C) as seen in Figure 7.9B, suggesting that there was neither alteration in nanomaterial structure and surface attachments nor irreversible change in sizes due to association of nanomaterials.

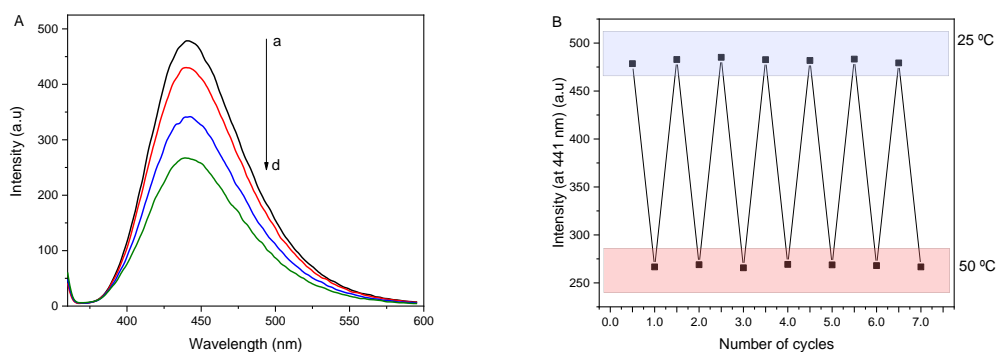


Figure 7.9 – (A) Photoluminescence spectra of N-GQDs-Ag aqueous dispersion at different temperatures: (a) 25, (b) 30, (c) 40 and (d) 50 °C. (B) Temperature sensing stability of N-GQDs-Ag aqueous dispersion in seven cycles of temperature switching at 25 to 50 °C.

Tests were also made after incorporation of N-GQDs-Ag in polyvinyl alcohol (PVA) in order to evaluate the PVA- N-GQDs-Ag film as a temperature probe. PVA was chosen because it is soluble in water and the N-GQDs-Ag dispersion was also prepared in water. The image of the blue emission observed from PVA-N-GQDs-Ag under UV is shown in Figure 7.10.



Figure 7.10 – Blue emission from the PVA-N-GQDs-Ag system under UV.

Variation in photoluminescence intensity measured from the PVA-N-GQDs-Ag film was monitored at 349/441 nm, after a piece of the film (3×0.8 cm) was placed into a cuvette containing 3 mL of 1-heptanol (solvent incompatible with PVA), with photoluminescence measured within the temperature range from 25 °C to 40 °C (with 5 °C intervals). Results showed a similar behavior from tests made in solution, where a decreasing that corresponds to 57 % of the original photoluminescence (measured at 25 °C) was observed as temperature was increased to 40 °C (Figure 7.11A). It is important to note that, different from the studies in

aqueous dispersion, a slight red-shift of 5 nm was observed as temperature was increased. At the initial temperature of 25 °C the maximum intensity was observed at 436 nm, while at the final temperature of 40 °C the maximum intensity was observed at 441 nm. Temperature variation may promote an additional thermal factor in excitation, favoring formation of excitonic centered at higher energy levels as temperature increased. This effect was not observed in solution as thermal energy may probably be readily absorbed by the fluid water solvation layer.

Overall result suggests that the probe can be used to evaluate temperature variation measuring magnitude of photoluminescence quenching but also, with less resolution, by measuring magnitude of spectral blue shift.

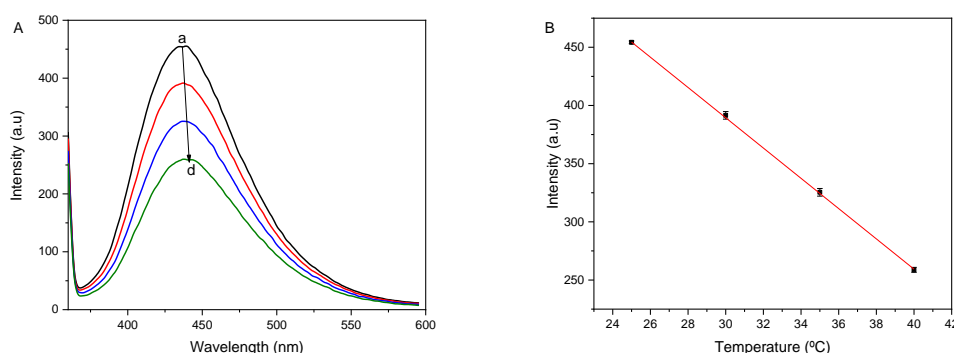


Figure 7.11 – (A) Photoluminescence spectra of PVA-N-GQDs-Ag at different temperatures of (a) 25, (b) 30, (c) 35 and (d) 40 °C. (B) Linear relationship between photoluminescent intensity of PVA-N-GQDs-Ag and temperature.

In terms of the magnitude of the signal quenching measured from the PVA-N-GQDs-Ag film, an inversely proportional linear relationship was found with the increasing of temperature ($R^2 = 0.999$) as seen in Figure 7.11B. Sensitivity of response was $-13 \text{ a.u. } ^\circ\text{C}^{-1}$ ($2.9 \% \text{ } ^\circ\text{C}^{-1}$). The reversibility of the response is shown in Figure 7.12, with results showing that after seven cycles of changing the temperature from 25°C to 40°C and then back to 25 °C, the measured photoluminescence was efficiently recovered. This behavior is similar to the one observed in tests with aqueous dispersion of N-GQDs-Ag, and shows the stability of the nanoparticles in different matrices in a larger temperature range.

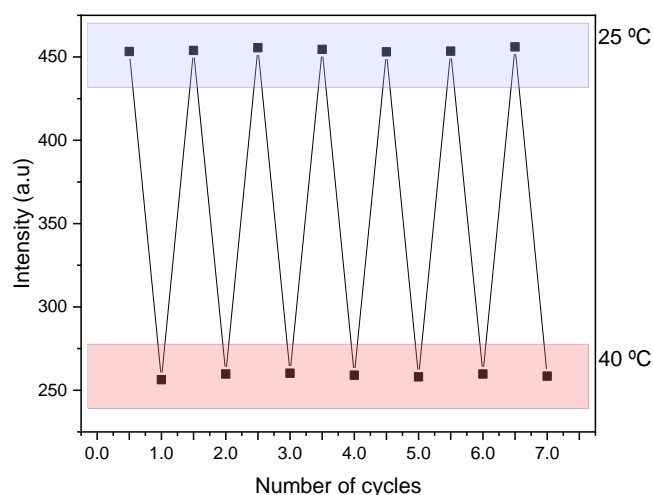


Figure 7.12 - Temperature sensing stability of PVA-N-GQDs-Ag in seven cycles of temperature switching within 25 °C to 40 °C range.

The overall results concerning the tested luminophores indicated that, among the three luminophores, the one based on the N-GQDs-Ag provided best performance as temperature probe, either as dispersion or as a part of a polymeric matrix, despite the fact that response sensitivity was not the highest. Predictable behavior with sensitivity of about 15 a.u °C⁻¹ is enough to provide discrimination between two consecutive units of temperature (as signal random variation of the probe is much lower than that) also providing total reversibility of photoluminescence as the nanomaterial does not degrade at the studied temperature range.

7.5. Toxicity tests of N-GQDs-Ag

If the use of the N-GQDs-Ag is aimed for cell probing, literature recent reported that N-GQDs (made by citric acid and glutathione) penetrate cells with minimum toxic effect [75]. Considering the potential use of N-GQDs-Ag as a nanothermometer for human cells, a study was conducted to evaluate the biocompatibility of N-GQDs-Ag by testing their toxicity in a culture of *S. cerevisiae*.

Different concentrations of the original N-GQDs-Ag dispersion (0.01 to 2 % v/v) were added to the YPD liquid medium containing *S. cerevisiae*, a species

of yeast being single-celled fungus microorganism. The cells were let to grow in an incubator for 24 h. After this period, their growth was assessed by absorption spectrophotometry (actually measuring the turbidity of the medium, at 570 nm, due to cells). Results for cells that grew in the presence of N-GQDs-Ag were compared with the ones made in an experiment with cells that did not grow in the presence of N-GQDs (Figure 7.13A). It was observed that concentrations of N-GQDs-Ag between 0.01 and 1 % v/v did not inhibit the growth of *S. cerevisiae* cells. When concentration of N-GQDs-Ag was 1 % v/v or higher, it was observed that *S. cerevisiae* cells did not grow. These results were comparable with the ones obtained for tests using N-GQDs instead of the ones decorated with silver, as seen in Figure 7.13 B. In the range from 0.01 and 1 % v/v, no relevant difference was detected between the two types of nanoparticles, showing that N-GQDs-Ag are not toxic in concentrations well above the ones to be used as temperature probes, therefore being biocompatible with *S. cerevisiae* cells.

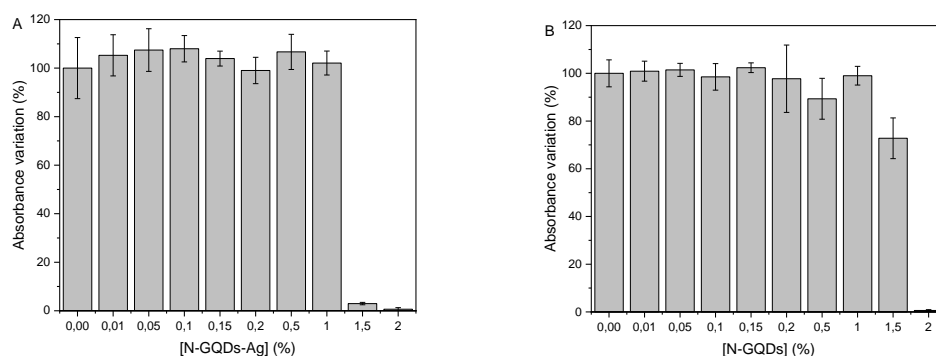


Figure 7.13 – Toxicity of (A) N-GQDs-Ag and (B) N-GQDs to *S. cerevisiae* cells.

7.6. Partial Conclusion

The $[\text{Eu}(\text{tta})_4](\text{Et}_3\text{NH}^+)$ complex, the benzothiazole organic dye (LASOC 460) and the N-GQDs-Ag have shown sensitivity towards changing of temperature in the medium when they were incorporated directly solubilized or dispersed with the tested medium or when inserted as an entity (in a polymeric matrix) inside the medium to be probed. The $[\text{Eu}(\text{tta})_4](\text{Et}_3\text{NH}^+)$ solution and PCL-Eu(III) only showed stability in a narrow temperature range. LASOC 460 was shown to be sensitive to temperature in different ways when molecularly dissolved and as

nanoaggregated. In the first case, the temperature increase led to a decrease in photoluminescent intensity, while in the second case it led to an increase in the photoluminescent intensity. In relation to N-GQDs-Ag, they were found to present the best performance as, besides predictable sensitivity to temperature, photoluminescence was readily restored as cycles of temperature were applied. The biocompatibility of the N-GQDs-Ag was proven, by testing their toxicity in *S. cerevisiae* cells culture, indicating it as a potential candidate to be used as nanothermometers for cells.

8 Conclusion

In analytical chemistry, the properties of photoluminescent materials are explored in order to improve existing analytical methods and/or to develop new methods for the analysis of various analytes in different matrices. In this work, the presented photoluminescent materials were used for the development of new analytical probes for the detection of different chemical species and for the sensing of temperature. The focus of this work was the use of a coordination compound containing Eu^{3+} ions for the determination of mercurial species and the use of graphene quantum dots doped with nitrogen and modified with silver for the determination of formaldehyde. Also, these two luminophores and an organic compound derived from the benzothiadiazole class were applied as temperature probes in different matrices and their performances were compared.

In the first part of this work, data from elemental analysis (CHNS), thermogravimetric analysis and infrared spectroscopy showed that the general chemical formula of the synthesized europium complex was $[\text{Eu}(\text{tta})_4](\text{Et}_3\text{NH}^+)$. Infrared spectroscopy data also showed the occurrence of covalent interaction between metal and ligand species. Regarding optical properties, the emission spectrum of the $[\text{Eu}(\text{tta})_4](\text{Et}_3\text{NH}^+)$ complex presented characteristic bands of intraconfigurational transitions from the Eu^{3+} ion ($^5\text{D}_0 \rightarrow ^7\text{F}_J$, $J = 0 - 4$), displaying monochromatic red color. Besides, the absence of phosphorescence bands belonging to the tta^- ligand indicated an efficient ligand-metal intramolecular energy transfer. After the complex characterization, the necessary conditions were adjusted for its efficient use as analytical probe for the determination of CH_3Hg^+ in PW after liquid-liquid extraction. In the presence of CH_3Hg^+ , the probe showed photoluminescent suppression. This effect probably occurs due to the interaction between mercury atoms and the sulfur atom present in the lateral chain of the tta^- ligand, causing interruption of the ligand-metal energy transfer and, consequently, the loss of the complex photoluminescence. Liquid-liquid extraction was used to guarantee selectivity towards CH_3Hg^+ . The presented method was statistically

compared with a method based in CV-AAS and it turned out to be a simpler option for those methods already described in the literature that often use expensive, laborious and time-consuming techniques.

In the second part of this work, data from XPS and FTIR confirmed the coordination of amino groups in the surface and edges of N-GQDs-Ag while data from DLS and STEM showed that their size is in the nanoscale. Their optical properties were also investigated and the N-GQDs-Ag presented their maximum emission at 441 nm, exhibiting blue color. After N-GQDs-Ag characterization, the necessary conditions were adjusted for their use as an efficient analytical probe for the determination of formaldehyde vapor in milk using the HS-SDME technique. Results showed that the interaction of N-GQDs-Ag with formaldehyde vapor in the headspace caused suppression of the nanoparticles photoluminescent emission, suggesting that formaldehyde could interact with the different groups in the surface and edges of N-GQDs-Ag modifying them. The proposed method was compared with a chromatographic method that uses liquid-liquid extraction and derivatization of the analyte and showed better sensibility to formaldehyde in lower concentrations, suggesting that the presented method is a simpler way to detect formaldehyde and can be used as a substitute to the methods that often use toxic chromophores and difficult techniques.

In the third part of this work, the $[\text{Eu}(\text{tta})_4](\text{Et}_3\text{NH}^+)$ complex, the N-GQDs-Ag and the benzothiadiazole derivative LASOC 460 were studied as photoluminescent probes for temperature. The LASOC 460 properties have been previously described in the literature and the investigation of its optical properties showed that it has maximum emission at 585 nm when the solvent is ethanol. These three luminophores were tested as thermometers in solution and in polymeric matrices. In solution, $[\text{Eu}(\text{tta})_4](\text{Et}_3\text{NH}^+)$ was tested in acetone/water 70/30 % v/v, LASOC 460 was tested in the aggregated form (ethanol/water 15/85 % v/v) and in the non-aggregated form (100% tert-butyl alcohol) and N-GQDs-Ag were tested in aqueous dispersion. In polymeric matrix, PCL-Eu(III), PMMA-LASOC 460 and PVA-N-GQDs-Ag films were formed and tested as photoluminescent thermometers. Results showed that all luminophores are responsive to temperature variation, with suppression of their photoluminescence, and in the case of LASOC 460 in tert-butyl alcohol it showed photoluminescence enhancement. When photoluminescence was studied in two or three cycles of temperature either in

solution or in the polymeric matrices, $[\text{Eu}(\text{tta})_4](\text{Et}_3\text{NH}^+)$ and PCL-Eu(III) showed stability in a narrow temperature range. For temperatures higher than 30 °C they lose photoluminescence due to slow dissipation of heat in the process of cooling. LASOC 460 showed decrease of photoluminescent intensity in the aggregated form and increase of photoluminescence intensity in the non-aggregated form. PMMA-LASOC 460 showed only a small photoluminescent variation due to less freedom of the molecule rotors. N-GQDs-Ag and PVA-N-GQDs-Ag showed the best stability in solution and in the polymeric matrix, where photoluminescent is reversed back to its original signal even after three cycles of temperature variation. Also, the aqueous matrix of N-GQDs-Ag allows them to be used in biological environments. Growth tests with *S. cerevisiae* cells showed that N-GQDs-Ag could be used in three orders of magnitude with the cells without inhibiting their growth, suggesting that they are not toxic to cells in the range from 0.1 to 1% v/v and, therefore, could be explored as luminescent nanothermometers for cells.

All methods proposed in this work are based on photoluminescence and presented results that showed that the photoluminescent materials used are very sensitive and selective for the analytes and parameters chosen. These results can also lead to future works where the mechanisms of interaction between probes and analytes can be further investigated and the developed methods can be adapted to the flow-injection analysis system. Also, results suggested that the cytotoxicity of the nanomaterials used in this work can be further evaluated and applied as nanothermometers for cells. Lastly, the luminescent probes for temperature can be evolved to optical sensors using optical fiber.

- [1] A. W. Czarnik, *Fluorescent Chemosensors of Ion and Molecule Recognition*. ACS Symp. Ser. 538. Washington DC: American Chemical Society, 1993.
- [2] A. W. Czarnik, *Chemical Communication in Water Using Fluorescent Chemosensors*, *Acc. Chem. Res.*, 27 (1994), 302-308, <http://doi.org/10.1021/ar00046a003>.
- [3] Y. Yang, J. Jiang, G. Shen, R. Yu, An optical sensor for mercury ion based on the fluorescence quenching of tetra(p-dimethylaminophenyl)porphyrin, *Anal. Chim. Acta*, 636 (2009) 83–88, <http://doi.org/10.1016/j.aca.2009.01.038>.
- [4] T. G. Cha, B. A. Baker, M. D. Sauffer, J. Salgado, D. Jaroch, J. L. Rickus, D. M. Porterfield, J. H. Choi, Optical nanosensor architecture for cell-signaling molecules using DNA aptamer-coated carbon nanotubes, *Acs Nano*, 5 (2011), 4236–4244, <https://doi.org/10.1021/nn201323h>.
- [5] B. Lamprecht, T. Abel, E. Kraker, E.; A. Haase, C. Konrad, M. Tscherner, S. Kostler, H. Ditlbacher, T. Mayr, Integrated fluorescence sensor based on ring-shaped organic photodiodes, *Physica status solidi (RRL) – Rapid Research Letters*, 4 (2010) 157–159, <http://doi.org/10.1002/pssr.201004096>.
- [6] F. Yan, T. Vo-Dinh, Surface-enhanced Raman scattering detection of chemical and biological agents using a portable Raman integrated tunable sensor, *Sensors and Actuators B-Chemical*, 121 (2007) 61–66, <https://doi.org/10.1016/j.snb.2006.09.032>.
- [7] Y. Zhang, C. Gu, A. M. Schwartzber, J. Z. Zhang, Surface-enhanced Raman scattering sensor based on D-shaped fiber, *Applied Physics Letters*, 87 (2005) 123105–3, <https://doi.org/10.1063/1.2051799>.
- [8] J. Homola, *Surface Plasmon Resonance Sensors for Detection of Chemical and Biological Species*. *Chemical Reviews*, 108 (2008) 462–493, <http://doi.org/10.1021/cr068107d>.
- [9] D. Dong, C. Zhao, Limitations and challenges of using Raman spectroscopy to detect the abiotic plant stress response, *Proc. Natl. Acad. Sci.*, 114 (2017) E5486–E5487, <https://doi.org/10.1073/pnas.1707408114>.
- [10] X. Michalet, F. F. Pinaud, L. A. Bentolila, J. M. Tsay, S. Doose, J. J. Li, G. Sundaresan, A. M. Wu, S. S. Gambhir, S. Weiss, Quantum dots for live cells, in vivo imaging, and diagnostics. *Science*, 307 (2005) 538–544, <http://doi.org/10.1126/science.1104274>.

- [11] M. Chalfie, Green Fluorescent Protein. *Photochemistry and Photobiology*, 62 (1995) 651–656, <http://doi.org/10.1111/j.1751-1097.1995.tb08712.x>.
- [12] R. B. Mujumdar, L. A. Ernst, S. R. Mujumdar, C. J. Lewis, A. S. Waggoner, Cyanine dye labeling reagentes: Sulfoindocyanine succinimidyl esters. *Bioconjugate Chemistry*, 4 (1993) 105–111, <http://doi.org/10.1021/bc00020a001>.
- [13] T. Xia, T. Song, G. Zhang, Y. Cui, Y. Yang, Z. Wang, G. Qian, A Terbium Metal–Organic Framework for Highly Selective and Sensitive Luminescence Sensing of Hg²⁺ Ions in Aqueous Solution, *Chem. Eur. J.*, 22 (2016) 18429–18434, <http://doi.org/10.1002/chem.201603531>.
- [14] A. S. Morris, R. Langari, *Measurement and instrumentation: theory and application*, 1st. ed. London: Elsevier (2012) 324 – 332.
- [15] IUPAC. *Compendium of Chemical Terminology*. 2 ed. A. D. McNaught, A. Wilkinson, (compiled). Oxford: Blackwell Scientific Publications, 1997, <https://doi.org/10.1351/goldbook>.
- [16] S. E. Braslavski, IUPAC. *Glossary of terms used in Photochemistry: IUPAC recommendations*, 2006. *Pure and Applied Chemistry*. 3 ed., 79 (2007), 293-465, <http://doi.org/10.1351/pac200779030293>.
- [17] D. L. Pavia, G. M. Lampman, G. S. Kriz, *Introdução à espectroscopia*. 1 ed. São Paulo: Cengage Learning, 2010.
- [18] A. J. W. G. Visser, O. J. Rolinski, *Basic Photophysics, Photobiological Sciences Online*, 2010, <http://edepot.wur.nl/193222>.
- [19] H. Bethe, *Termaufspaltung in Kristallen*, *Zeitschrift fur Physik*, 60 (1930) 218-233, <http://doi.org/10.1002/andp.19293950202>.
- [20] J. Becquerel, *Einleitung in eine Theorie der magneto-optischen Erscheinungen in Kristallen*, *Zeitschrift fur Physik*, 58 (1929) 205-216, <http://doi.org/10.1007/BF01339043>.
- [21] H. A. Kramers, *Proc. Acad. Sci. Amsterdam*, 32 (1930) 1176, 1930.
- [22] B. G. Wybourne, *Spectroscopic Properties of Rare Earths*. New York: Interscience Publishers, 1965.
- [23] T. S. Martins, P. C. Isolani, *Terras raras: aplicações industriais e biológicas*, *Química Nova*, 28 (2005) 111-117, <http://doi.org/10.1590/S0100-40422005000100020>.
- [24] G. W. Burdick, R. L. Summerscales, S. M. Crooks, M. F. Reid, F. S. Richardson, *Electric-dipole 4f_n–4f_n transition intensity parametrizations for lanthanides: multiple indistinguishable parameter sets and multiple local minima*, *Alloys Comp.* 303-304 (2000) 376-382, [http://doi.org/10.1016/S0925-8388\(00\)00644-7](http://doi.org/10.1016/S0925-8388(00)00644-7).
- [25] S. I. Weissman, *Intramolecular Energy Transfer – The Fluorescence of complexes of Europium*, *Journal of Chemical Physics*, 10 (1942), 214-217, <http://doi.org/10.1063/1.1723709>.
- [26] H. F. Brito, O. L. Malta, J. F. S. Menezes, *Luminescent properties of diketonates of trivalent europium with dimethyl sulfoxide*, *Journal of Alloys*

and Compounds, 303 (2000) 336-339, [https://doi.org/10.1016/S0925-8388\(00\)00604-6](https://doi.org/10.1016/S0925-8388(00)00604-6).

[27] K. Binnemans, Rare-earth beta-diketonates. In: K. A. Gschneidner Jr, J.-C.G. Bünzli, V.K. Pecharsky, (Eds.), Handbook on the Physics and Chemistry of Rare Earths, Elsevier, Amsterdam, 35 (2005) 111, [https://doi.org/10.1016/S0168-1273\(05\)35003-3](https://doi.org/10.1016/S0168-1273(05)35003-3).

[28] S. Lis, M. Elbanowski, B. Mąkowska, Z. Hnatejko, Energy transfer in solution of lanthanide complexes, Journal of Photochemistry and Photobiology A: Chemistry, 150 (2002) 233-247, [https://doi.org/10.1016/S1010-6030\(01\)00637-2](https://doi.org/10.1016/S1010-6030(01)00637-2).

[29] X. Zhang, N. Xu, Q. Ruan, D. Q. Lu, Y. H. Yang, R. Hu, A label-free and sensitive photoluminescence sensing platform based on long persistent luminescence nanoparticles for the determination of antibiotics and 2,4,6-trinitrophenol, RSC Adv., 8 (2018) 5714-5720, <http://doi.org/10.1039/c7ra12222e>.

[30] R. Viter, A. Tereshchenko, V. Smyntyna, J. Ogorodniichuk, N. Starodub, R. Yakimova, V. Khranovskyy, A. Ramanavicius, Toward development of optical biosensors based on photoluminescence of TiO₂ nanoparticles for the detection of Salmonella, Sensors and Actuators B, 252 (2017) 95–102, <http://doi.org/10.1016/j.snb.2017.05.139>.

[31] O. S. Wolfbeis, An overview of nanoparticles commonly used in fluorescent bioimaging, Chem. Soc. Rev., 44 (2015) 4743-4768, <http://doi.org/10.1039/c4cs00392f>.

[32] F. O. Silva, L. C. S. Viol, D. L. F. Ferreira, J. L. A. Alves, M. A. Schiavon, O estado da arte da síntese de semicondutores nanocristalinos coloidais, Quim. Nova, 33 (2010) 1933-1939, <http://doi.org/10.1590/S0100-40422010000900021>.

[33] A. I. Ekimov, A. L. Efros, A. A. Onushchenko, Quantum size effect in semiconductor microcrystals, Solid State Communications, 56 (1985) 921-924, [https://doi.org/10.1016/S0038-1098\(85\)80025-9](https://doi.org/10.1016/S0038-1098(85)80025-9).

[34] L. E. Brus, Electron-electron and electron-hole interactions in small semiconductor crystallites - the size dependence of the lowest excited electronic state, J. Chem. Phys., 80 (1984) 4403–4409, <http://doi.org/10.1063/1.447218>.

[35] W. R. Algar, K. Susumu, J. B. Delehanty, I. L. Medintz, Semiconductor quantum dots in bioanalysis: crossing the valley of death, Anal. Chem. 83 (2011) 8826–8837, <http://doi.org/10.1021/ac201331r>.

[36] P. Alivisatos, The use of nanocrystals in biological detection, Nat. Biotechnol., 22 (2004) 47–52, <http://doi.org/10.1038/nbt927>.

[37] A. P. Alivisatos, W. Gu, C. Larabell, Quantum dots as cellular probes, Annu. Rev. Biomed. Eng., 7 (2005) 55–76, <http://doi.org/10.1146/annurev.bioeng.7.060804.100432>.

[38] D. Bera, L. Qian, T. Tseng, P. H. Holloway, Quantum Dots and Their Multimodal Applications: A Review, Materials, 3 (2010) 2260-2345, <http://doi.org/10.3390/ma3042260>.

- [39] V.I. Klimov, Mechanisms for photogeneration and recombination of multiexcitons in semiconductor nanocrystals: Implications for lasing and solar energy conversion, *J. Phys. Chem. B*, 110 (2006) 16827–16845, <http://doi.org/10.1021/jp0615959>.
- [40] L. E. Brus, A simple-model for the ionization-potential, electron-affinity, and aqueous redox potentials of small semiconductor crystallites, *J. Chem. Phys.*, 79 (1983) 5566–5571, <https://doi.org/10.1063/1.445676>.
- [41] Y. Wang, N. Herron, Nanometer-sized semiconductor clusters—materials synthesis, quantum size effects, and photophysical properties, *J. Phys. Chem.*, 95 (1991) 525–532, <http://doi.org/10.1021/j100155a009>.
- [42] R. Liu, D. Wu, S. Liu, K. Koynov, W. Knoll, Q. Li, An aqueous route to multicolour photoluminescent carbon dots using silica spheres as carriers, *Angewandte Chemie International Edition*, 48 (2009) 4598, <http://doi.org/10.1002/anie.200900652>.
- [43] S. N. Baker, G. A. Baker, Luminescent carbon nanodots: emergent nanolights, *Angew. Chem. Int.*, 49 (2010) 6726–6744, <https://doi.org/10.1002/anie.200906623>.
- [44] Y.-P. Sun, B. Zhou, Y. Lin, W. Wang, K. A. S. Fernando, P. Pathak, M. J. Meziani, B. A. Harruff, X. Wang, H. Wang, P. G. Luo, H. Yang, M. E. Kose, B. Chen, L. M. Veca, S.-Y. Xie, Quantum-sized carbon dots for bright and colorful photoluminescence, *J. Am. Chem. Soc.*, 128 (2006) 7756–7757, <http://doi.org/10.1021/ja062677d>.
- [45] B. L. Silver, *Irreducible Tensor Methods: An Introduction for Chemists*. London: Academic Press, 1976.
- [46] E. U. Condon, H. Odabasi, *Atomic Structure*. Cambridge University Press, 1980.
- [47] P. A. Tanner, Some misconceptions concerning the electronic spectra of tri positive europium and cerium, *Chem. Soc. Rev.*, 42 (2013) 5090-5101, <http://doi.org/10.1039/C3CS60033E>.
- [48] X. Li, H. Chen, A. M. Kirillov, Y. Xie, C. Shan, B. Wang, C. Shia, Y. Tang, A paper-based lanthanide smart device for acid–base vapour detection, anti-counterfeiting and logic operations, *Inorg. Chem. Front.*, 3 (2016) 1014, <http://doi.org/10.1039/c6qj00164e>.
- [49] Y. Wang, H. Wang, M. Yang, J. Yuan, J. Wu, A visible-light-excited europium(III) complex-based luminescent probe for visualizing copper ions and hydrogen sulfide in living cells, *Optical Materials*, 75 (2018) 243-251, <http://doi.org/10.1016/j.optmat.2017.10.030>.
- [50] S.-Y. Huang, V. C. Pierre, A turn-on luminescent europium probe for cyanide detection in water, *Chem. Commun.*, 54 (2018) 9210, <http://doi.org/10.1039/c8cc05114c>.
- [51] V. Borse, M. Sadawana, R. Srivastava, CdTe Quantum Dots: Aqueous Phase Synthesis, Stability Studies and Protein Conjugation for Development of Biosensors, SPIE Photonics Europe, International Society for Optics and Photonics, 9884 (2016) 988423-1–988423-12, <http://doi.org/10.1117/12.2225262>.

- [52] Z. Ding, Z. Hao, B. Meng, Z. Xie, J. Liu, L. Dai, Few-layered graphene quantum dots as efficient hole-extraction layer for high-performance polymer solar cells, *Nanomater. Energy*, 15 (2015) 186–192, <https://doi.org/10.1016/j.nanoen.2015.04.019>.
- [53] Y. Dong, C. Chen, X. Zheng, L. Gao, Z. Cui, H. Yang, C. Guo, Y. Chi, C. M. Li, Onestep and high yield simultaneous preparation of single-and multi-layer graphene quantum dots from CX-72 carbon black, *J. Mater. Chem.*, 22 (2012) 8764–8766, <http://doi.org/10.1039/C2JM30658A>.
- [54] Y. Dong, J. Shao, C. Chen, H. Li, R. Wang, Y. Chi, X. Lin, G. Chen, Blue luminescent graphene quantum dots and graphene oxide prepared by tuning the carbonization degree of citric acid, *Carbon*, 50 (2012) 4738–4743, <https://doi.org/10.1016/j.carbon.2012.06.002>.
- [55] G. Eda, Y. Y. Lin, C. Mattevi, H. Yanaguchi, H. A. Chen, I. Chen, C. W. CHEN, M. Chhowalla, Blue photoluminescence from chemically derived graphene oxide, *Adv. Mater.*, 22 (2010) 505–509, <https://doi.org/10.1002/adma.200901996>.
- [56] S.-Y. Ju, W. P. Kopcha, F. Papadimitrakopoulos, Brightly fluorescent single-walled carbon nanotubes via an oxygen-excluding surfactant organization, *Science*, 323 (2009) 1319–1323, <http://doi.org/10.1126/science.1166265>.
- [57] F. Jiang, D. Chen, R. Li, Y. Wang, G. Zhang, S. Li, J. Zheng, N. Huang, Y. Gu, C. Wang, Eco-friendly synthesis of size-controllable amine-functionalized graphene quantum dots with antimycoplasma properties, *Nanoscale*, 5 (2013) 1137–1142, <http://doi.org/10.1039/C2NR33191H>.
- [58] R. Ghafouri, Exploring Pentagon-Heptagon Pair Defects in the Triangular Graphene Quantum Dots: A Computational Study, *Mater. Chem. Phys.*, 175 (2016) 223–232, <https://doi.org/10.1016/j.matchemphys.2016.03.025>.
- [59] P. Sudhagar, I. Herraiz-Cardona, H. Park, T. Song, S. H. Noh, S. Gimenez, I. M. Sero, F. Fabregat-Santiago, J. Bisquert, C. Terashima, U. Paik, Y. S. Kang, A. Fujishima, T. H. Han, Exploring Graphene Quantum Dots/TiO₂ Interface in Photoelectrochemical Reactions: Solar to Fuel Conversion, *Electrochim. Acta*, 187 (2016) 249–255, <https://doi.org/10.1016/j.electacta.2015.11.048>.
- [60] F. Liu, M. H. Jang, H. D. Ha, J. H. Kim, Y. H. Cho, T. S. Seo, Facile Synthetic Method for Pristine Graphene Quantum Dots and Graphene Oxide Quantum Dots: Origin of Blue and Green Luminescence, *Adv. Mater.*, 25 (2013) 3657–3662, <https://doi.org/10.1002/adma.201300233>.
- [61] H. Tetsuka, R. Asahi, A. Nagoya, K. Okamoto, I. Tajima, R. Ohta, A. Okamoto, A. Optically Tunable Amino-Functionalized Graphene Quantum Dots. *Adv. Mater.*, 24 (2012) 5333–5338, <https://doi.org/10.1002/adma.201201930>.
- [62] A. Ananthanarayanan, X. Wang, P. Routh, B. Sana, S. Lim, D.-H. Kim, K.-H. Lim, J. Li, P. Chen, Facile Synthesis of Graphene Quantum Dots from 3d Graphene and Their Application for Fe³⁺ Sensing, *Adv. Funct. Mater.*, 24 (2014) 3021–3026, <https://doi.org/10.1002/adfm.201303441>.

- [63] J. Peng, W. Gao, B. K. Gupta, Z. LIU, R. Romero-Aburto, L. Ge, L. Song, L. B. Alemany, X. Zhan, G. Gao, S. A. Vithayathil, B. A. Kaipparattu, A. A. Marti, T. Hayashi, J. J. Zhu, P. M. Ajayan, Graphene Quantum Dots Derived from Carbon Fibers, *Nano Lett.*, 12 (2012) 844–849, <http://doi.org/10.1021/nl2038979>.
- [64] A. Zhao, Z. Chen, C. Zhao, N. Gao, J. Ren, X. Qu, Recent advances in bioapplications of C-dots, *Carbon*, 85 (2015) 309–327, <https://doi.org/10.1016/j.carbon.2014.12.045>.
- [65] P. G. Luo, S. Sahu, S.-T. Yang, S. K. Sonkar, J. Wang, H. Wang, G. E. Lecroy, L. Cao, Y.-P. Sun, Carbon “quantum” dots for optical bioimaging, *J. Mater. Chem. B*, 1 (2013) 2116–2127, <http://doi.org/10.1039/C3TB00018D>.
- [66] Y. G. Adewuyi, S.-Y. Cho, R.-P. Tsay, G. R. Carmichael, Importance of formaldehyde in cloud chemistry, *Atmospheric Environment* (1967), 18 (1984) 2413–2420, [https://doi.org/10.1016/0004-6981\(84\)90011-8](https://doi.org/10.1016/0004-6981(84)90011-8).
- [67] H. Li, Z. Kang, Y. Liu, S.-T. Lee, Carbon nanodots: synthesis, properties and applications, *J. Mater. Chem.*, 22 (2012) 24230–24253, <http://doi.org/10.1039/C2JM34690G>.
- [68] L. Li, G. Wu, G. Yang, J. Peng, J. Zhao, J.-J. Zhu, Focusing on luminescent graphene quantum dots: current status and future perspectives, *Nanoscale*, 5 (2013) 4015–4039, <http://doi.org/10.1039/c3nr33849e>.
- [69] M. Masteri-Farahani, F. Askari, Design and photophysical insights on graphene quantum dots for use as nanosensor in differentiating methamphetamine and morphine in solution, *Spectrochim Acta A Mol Biomol Spectrosc.*, 206 (2018) 448–453, <http://doi.org/10.1016/j.saa.2018.08.044>.
- [70] O. J. Achadu, T. Nyokong, Fluorescence “turn-ON” nanosensor for cyanide ion using supramolecular hybrid of graphene quantum dots and cobalt pyrene-derivatized phthalocyanine, *Dyes and Pigments*, 160 (2019) 328–335, <https://doi.org/10.1016/j.dyepig.2018.08.038>.
- [71] C. Qu, D. Zhang, R. Yang, J. Hu, L. Qua, Nitrogen and sulfur co-doped graphene quantum dots for the highly sensitive and selective detection of mercury ion in living cells, *Spectrochimica Acta Part A: Molecular and Biomolecular Spectroscopy*, 206 (2019) 588–596, <https://doi.org/10.1016/j.saa.2018.07.097>.
- [72] C. A. T. Toloza, S. Khan, R. L. D. Silva, E. C. Romani, F. L. Freire Jr., R. Q. Aucélio, Different approaches for sensing captopril based on functionalized graphene quantum dots as photoluminescent probe, *Journal of Luminescence*, 179 (2016) 83–92, <https://doi.org/10.1016/j.jlumin.2016.06.055>.
- [73] C. A. T. Toloza, S. Khan, R. L. D. Silva, E. C. Romani, D. G. Larrude, S. R. W. Louro, F. L. Freire Jr., R. Q. Aucélio, Photoluminescence suppression effect caused by histamine on amino-functionalized graphene quantum dots with the mediation of Fe³⁺, Cu²⁺, Eu³⁺: Application in the analysis of spoiled tuna fish, *Microchemical Journal*, 133 (2017) 448–459, <http://doi.org/10.1016/j.microc.2017.04.013>.

- [74] C. A. T. Toloza, J. M. S. Almeida, S. Khan, Y. G. Santos, A. R. Silva, R. Q. Aucélio, Kanamycin detection at graphene quantum dot-decorated gold nanoparticles in organized medium after solid-phase extraction using an aminoglycoside imprinted polymer, *MethodsX*, 5 (2018) 1605–1612, <https://doi.org/10.1016/j.mex.2018.11.019>.
- [75] A. De Falco, E. Santa-Helena, C. A. T. Toloza, J. M. S. Almeida, D. G. Larrude, F. V. P. Meirelles, C. R. Gioda, R. Q. Aucelio, A. Gioda, Luminescence imaging and toxicity assessment of graphene quantum dots using *in vitro* models, *Fullerenes, Nanotubes and Carbon Nanostructures*, (2021), <http://doi.org/10.1080/1536383X.2021.1995367>.
- [76] M. Akhtaruzzaman, N. Kamata, J. Nishida, S. Ando, H. Tada, M. Tomura, Y. Yamashita, Synthesis, characterization and FET properties of novel dithiazolylbenzothiadiazole derivatives, *Chem. Commun.*, 0 (2005) 3183–3185, <http://doi.org/10.1039/B503814F>.
- [77] S. Kato, T. Matsumoto, T. Ishi, T. Thiemann, M. Shigeiwa, H. Gorohmaru, S. Maeda, Y. Yamashita, S. Mataka, Strongly red-fluorescent novel donor– π -bridge–acceptor– π -bridge–donor (D– π –A– π –D) type 2,1,3-benzothiadiazoles with enhanced two-photon absorption cross-sections, *Chem. Commun.*, 0 (2004) 2342–2343, <http://doi.org/10.1039/B410016F>.
- [78] A. V. Moro, P. C. Ferreira, P. Migowski, F. S. Rodembusch, J. Dupont, D. S. Ludtke, Synthesis and photophysical properties of fluorescent 2,1,3-benzothiadiazole-triazole-linked glycoconjugates: selective chemosensors for Ni(II), *Tetrahedron*, 69 (2013) 201–206, <https://doi.org/10.1016/j.tet.2012.10.043>.
- [79] M. Akhtaruzzaman, M. Tomura, J. Nishida, Y. Yamashita, Synthesis and Characterization of Novel Dipyridylbenzothiadiazole and Bisbenzothiadiazole Derivatives, *J. Org. Chem.*, 69 (2004) 2953–2958, <http://doi.org/10.1021/jo035800h>.
- [80] M. Akhtaruzzaman, M. Tomura, M. B. Zaman, J. Nishida, Y. Yamashita, Synthesis and Characterization of New Linear π -Conjugated Molecules Containing Bis(ethynylpyridine) Units with a Benzothiadiazole Spacer, *J. Org. Chem.*, 67 (2002) 7813–7818, <http://doi.org/10.1021/jo0202334>.
- [81] H. Sakurai, M. T. S. Ritonga, H. Shibatani, T. Hirao, Synthesis and characterization of p-phenylenediamine derivatives bearing an electron-acceptor unit, *J. Org. Chem.*, 70 (2005) 2754–2762, <http://doi.org/10.1021/jo048324j>
- [82] M. Velusamy, K. R. J. Thomas, J. T. Lin, Y. C. Hsu, K. C. Ho, Organic dyes incorporating low-band-gap chromophores for dye-sensitized solar cells, *Org. Lett.* 2005, 7 (2005) 1899–1902, <https://doi.org/10.1021/ol050417f>.
- [83] Y. Wu, W. Zhu, Organic sensitizers from D– π –A to D–A– π –A: effect of the internal electron-withdrawing units on molecular absorption, energy levels and photovoltaic performances, *Chem. Soc. Rev.*, 42 (2013) 2039–2058, <http://doi.org/10.1039/C2CS35346F>.
- [84] R. Rattanawan, V. Promarak, T. Sudyoadsuk, S. Namuangruk, N. Kungwan, S. Yuan, S. Jungsuttiwong. Theoretical design of coumarin

derivatives incorporating auxiliary acceptor with D- π -A- π -A configuration for dye-sensitized solar cell, *J. Photochem. Photobiol. A Chem.*, 322–323 (2016) 16–26, <https://doi.org/10.1016/j.jphotochem.2016.02.016>.

[85] E. Hosseinzadeh, N. L. Hadipour, G. Parsafar, Molecular engineering of bithiazole-based organic dyes with different electron-rich linkers toward highly efficient dye-sensitized solar cells, *J. Photochem. Photobiol. A Chem.*, 349 (2017) 171–182, <https://doi.org/10.1016/j.jphotochem.2017.09.001>.

[86] Y. Yu, C. Dong, An efficient colorimetric and fluorescent probe for the detection of fluoride ions based on a benzothiadiazole derivative, *Anal. Methods*, 7 (2015) 9604–9608, <https://doi.org/10.1039/C5AY02108A>.

[87] B. A. D. Neto, J. R. Corrêa, P. H. P. R. Carvalho, D. C. B. D. Santos, B. C. Guido, C. C. Gatto, H. C. B. de Oliveira, M. Fasciotti, M. N. Eberlin, E. N. da Silva, Selective and Efficient Mitochondria Staining with Designed 2,1,3-Benzothiadiazole Derivatives as Live Cell Fluorescence Imaging Probes, *J. Braz. Chem. Soc.*, 23 (2012) 770–781, <http://doi.org/10.1590/S0103-50532012000400024>.

[88] F. Ni, Z. Wu, Z. Zhu, T. Chen, K. Wu, C. Zhong, K. An, D. Wei, D. Ma, C. Yang, D. Ma, P. Y. Lu, A. Lien, M. R. Bryce, Teaching an old acceptor new tricks: rationally employing 2,1,3-benzothiadiazole as input to design a highly efficient red thermally activated delayed fluorescence emitter, *J. Mater. Chem. C*, 5 (2017) 1363–1368, <http://doi.org/10.1039/C7TC00025A>.

[89] E. Angioni, M. Chapran, K. Ivaniuk, N. Kostiv, V. Cherpak, P. Stakhira, A. Lazauskas, S. Tamulevicius, D. Volyniuk, N. J. Findlay, T. Tuttle, J. V. Grazulevicius, P. J. Skabara, A single emitting layer white OLED based on exciplex interface emission, *J. Mater. Chem. C*, 4 (2016) 3851–3856, <http://doi.org/10.1039/C6TC00750C>,

[90] B. A. Neto, P. H. Carvalho, J. R. Correa, Benzothiadiazole Derivatives as Fluorescence Imaging Probes: Beyond Classical Scaffolds, *Acc Chem Res.*, 48 (2015) 1560–1569, <http://doi.org/10.1021/ar500468p>.

[91] J. Wu, G. Lai, Z. Li, Y. Lu, T. Leng, Y. Shen, C. Wang, Novel 2,1,3-benzothiadiazole derivatives used as selective fluorescent and colorimetric sensors for fluoride ion, *Dyes and Pigments*, 124 (2016) 268–276, <https://doi.org/10.1016/j.dyepig.2015.09.021>.

[92] M. Alfonso, A. Espinosa, A. Tárraga, P. Molina, Multifunctional Benzothiadiazole-Based Small Molecules Displaying Solvatochromism and Sensing Properties toward Nitroarenes, Anions, and Cations, *Chemistry Open.*, 3 (2014) 242–9, <https://doi.org/10.1002/open.201402022>.

[93] Q. Zou, H. Tian, Chemodosimeters for mercury(II) and methylmercury(I) based on 2,1,3-benzothiadiazole, *Sensors and Actuators B*, 149 (2010) 20–27, <http://doi.org/10.1016/j.snb.2010.06.040>.

[94] R. M. da Fiuza, J. Padilha, L. Maqueira, R. Q. Aucélio, J. Limberger, Synthesis and application of a highly fluorescent styryl-benzothiadiazole derivative as a chemosensor for ethanol in hydroalcoholic solutions, *Spectrochimica Acta Part A: Molecular and Biomolecular Spectroscopy*, 271 (2022) 120913, <https://doi.org/10.1016/j.saa.2022.120913>.

- [95] Agency for Toxic Substances and Disease Registry. Toxicological Profile for Mercury. Agency for Toxic Substances and Disease Registry, US Department of Health and Human Services; 1999.
- [96] T. W. Clarkson, L. Magos, G. J. Myers, The toxicology of mercury--current exposures and clinical manifestations. *N Engl J Med.*, 349 (2003) 1731-1737, <http://doi.org/10.1056/NEJMra022471>.
- [97] R. C. C. M. Micaroni, M. I. M. S. Bueno, W. F. Jardim, Compostos de mercúrio. Revisão de métodos de determinação, tratamento e descarte, *Quím. Nova*, 23 (2000), 487-495, <http://doi.org/10.1590/S0100-40422000000400011>.
- [98] C.N. do M.A. CONAMA, Resolução nº 393, 8 de agosto de 2007, Ministério Do Meio Ambiente. (2007) 72–73.
- [99] T.I. Røe Utvik, Chemical characterization of produced water from four offshore oil production platforms in the North Sea, *Chemosphere*, 39 (1999) 2593–2606. [http://doi.org/10.1016/S0045-6535\(99\)00171-X](http://doi.org/10.1016/S0045-6535(99)00171-X).
- [100] R. Funston, R. Ganesh, L.Y.C. Leong, Evaluation of technical and economic feasibility of treating oilfield produced water to create a “new” water resource. In: *Produced Water*. Colorado Spring, Colorado, 2002.
- [101] R. C. Gupta, *Veterinary Toxicology: Basic and Clinical Principles*. 2 ed. Amsterdã: Academic Press/Elsevier (2012) 537-543.
- [102] M. C. Bisinoti, W. F. O Jardim, Comportamento do metilmercúrio (metilHg) no ambiente, *Quim. Nova*, 27 (2004) 593-600, <http://doi.org/10.1590/S0100-40422004000400014>.
- [103] M. Fuyuta, T. Fujimoto, S. Hirata, Embryotoxic effects of methylmercuric chloride administered to mice and rats during orangogenesis, *Teratology*, 18 (1978) 353-366, <http://doi.org/10.1002/tera.1420180310>.
- [104]. H. Tsuchiya, K. Mitani, K. Kodama, T. NAKATA, Placental transfer of heavy metals in normal pregnant Japanese women, *Arch Environ Health*, 39 (1984) 11-17, <https://doi.org/10.1080/00039896.1984.10545827>.
- [105] T. Labatzke, G. Schlemmer, Ultratrace determination of mercury in water following EN and EPA standards using atomic fluorescence spectrometry, *Anal Bioanal Chem*, 378 (2004) 1075–1082, <http://doi.org/10.1007/s00216-003-2416-x>.
- [106] J. R. Miranda-Andrades, S. Khan, M. J. Pedrozo-Penãfiel, K. C. B. Alexandre, R. M. Maciel, R. Escalfoni, M. L. B. Tristão, R. Q. Aucelio, Combination of ultrasonic extraction in a surfactant-rich medium and distillation for mercury speciation in offshore petroleum produced waters by gas chromatography cold vapor atomic fluorescence spectrometry, *Spectrochimica Acta Part B: Atomic Spectroscopy* 158 (2019) 105641, <http://doi.org/10.1016/j.sab.2019.105641>.
- [107] Y. Gao, S. D. Galan, A. D. Brauwere, W. Baeyens, M. Leermakers, Mercury speciation in hair by headspace injection-gas chromatography-atomic fluorescence spectrometry (methyl mercury) and

combustion-atomic absorption spectrometry (total Hg), *Talanta*, 82 (2010) 1919 – 1923, <http://doi.org/10.1016/j.talanta.2010.08.012>.

[108] V. F. Taylor, A. Carter, C. Davies, B. P. Jackson, Trace-Level Automated Mercury Speciation Analysis, *Anal Methods*. 3 (2011), 1143-1148 <http://doi.org/10.1039/C0AY00528B>.

[109] A. Sharif, M. Monperrus, E. Tessier, D. Amouroux, Determination of methyl mercury and inorganic mercury in natural waters at the pgL-1 level: Intercomparison between PT-GC-Pyr-AFS and GC-ICP-MS using Ethylation or Propylation derivatization, *E3S Web of Conferences* 1 (2013) 09001, <http://doi.org/10.1051/e3sconf/20130109001>.

[110] Jarol R. Miranda-Andrades, Sonia Letichevsky, Dunieskys R. González Larrudé, Ricardo Q. Aucelio, Photo-generation of mercury cold vapor mediated by graphene quantum dots/TiO₂ nanocomposite: On line time-resolved speciation at ultra-trace levels, *Analytica Chimica Acta* 1127 (2020) 256-268, <http://doi.org/10.1016/j.aca.2020.06.048>.

[111] M. Wang, W. Feng, J. Shi, F. Zhang, B. Wang, M. Zhu, B. Li, Y. Zhao, Z. Chai, Development of a mild mercaptoethanol extraction method for determination of mercury species in biological samples by HPLC-ICP-MS, *Talanta*, 71 (2007) 2034-2039, <http://doi.org/10.1016/j.talanta.2006.09.012>.

[112] R. K. Mahajan, I.; Kaur, T. S. Lobana, A Mercury(II) ion-selective electrode based on neutral salicylaldehyde thiosemicarbazone, *Talanta*, 59 (2003) 101-105, [https://doi.org/10.1016/S0039-9140\(02\)00473-3](https://doi.org/10.1016/S0039-9140(02)00473-3).

[113] L. Yang, Z. Mester, R. Sturgeon, Determination of methylmercury in fish tissues by isotope dilution SPME-GC-ICP-MS, *J. Anal. At. Spectrom.*, 18 (2003) 431–436, <http://doi.org/10.1039/b301299a>.

[114] L. N. Suvarapu, Y.-K. Seo, S.-O. Baek, Speciation and determination of mercury by various analytical techniques, *Rev. Anal. Chem.*, 32 (2013) 225–245, <https://doi.org/10.1515/revac-2013-0003>.

[115] H. Yang, R. Jian, J. Liao, J. Cui, P. Fang, Z. Zou, K. Huang, Recent development of non-chromatographic atomic spectrometry for speciation analysis of mercury, *Applied Spectroscopy Reviews*, 2021, ahead-of-print, 1-20. <https://doi.org/10.1080/05704928.2021.1893183>.

[116] J. R. Miranda-Andrades, S. Khan, C. A. T. Toloza, E. C. Romani, F. L. Freire Júnior, R. Q. Aucelio, Thiomersal photo-degradation with visible light mediated by graphene quantum dots: Indirect quantification using optical multipath mercury cold-vapor absorption spectrophotometry, *Spectrochimica Acta Part B: Atomic Spectroscopy*, 138 (2017) 81-89, <https://doi.org/10.1016/j.sab.2017.10.011>.

[117] J. R. Miranda-Andrades, S. Khan, C. A. T. Toloza, R. M. Maciel, R. Escalfoni, M. L. B. Tristão, R. Q. Aucelio, Speciation and ultra trace determination of mercury in produced waters from offshore drilling operations using portable instrumentation and matrix-matching calibration, *Microchemical Journal* 146 (2019) 1072-1082. <https://doi.org/10.1016/j.microc.2019.02.045>.

- [118] J. R. Miranda-Andrades, S. Letichevsky, D. R. G. Larrudé, R. Q. Aucelio, Photo-generation of mercury cold vapor mediated by graphene quantum dots/TiO₂ nanocomposite: On line time-resolved speciation at ultra-trace levels, *Analytica Chimica Acta* 1127 (2020) 256-268 <https://doi.org/10.1016/j.aca.2020.06.048>.
- [119] J. Mei, N. L. C. Leung, R. T. K. Kwok, J. W. Y. Lam, B. Z. Tang, Aggregation-induced emission: together we shine, united we soar!, *Chem. Rev.*, 115 (2015) 11718–11940, <https://doi.org/10.1021/acs.chemrev.5b00263>.
- [120] C. Han, C. Zheng, J. Wang, G. Cheng, Y. Lv, X. Hou, Photo-induced cold vapor generation with low molecular weight alcohol, aldehyde, or carboxylic acid for atomic fluorescence spectrometric determination of mercury, *Anal Bioanal. Chem* 388 (2007) 825–830, <https://doi.org/10.1007/s00216-006-1006-0>.
- [121] Y. Gao, W. Yang, C. Zheng, X. Hou, L. Wu, On-line preconcentration and in situ photochemical vapor generation in coiled reactor for speciation analysis of mercury and methylmercury by atomic fluorescence spectrometry, *J. Anal. At. Spectrom.*, 26 (2011) 126–132, <https://doi.org/10.1039/c0ja00137f>.
- [122] M. L. Aulsebrook, B. Graham, M. R. Grace, K. L. Tuck Lanthanide complexes for luminescence-based sensing of low molecular weight analytes, *Coordination Chemistry Reviews*, 375 (2018) 191-220, <https://doi.org/10.1016/j.ccr.2017.11.018>.
- [123] T. Gorai, U. Maitra, Supramolecular Approach to Enzyme Sensing on Paper Discs Using Lanthanide Photoluminescence, *ACS Sensor*, 1 (2016) 934–940, <http://doi.org/10.1021/acssensors.6b00341>.
- [124] B. K. McMahon, R. Pal, D. Parker, A bright and responsive europium probe for determination of pH change within the endoplasmic reticulum of living cells, *Chem. Commun.*, 49 (2013) 5363-5365, <https://doi.org/10.1039/C3CC42308E>.
- [125] É. A. de Souza, C. B. Azevedo, L. A. Rocha, E. H. de Faria, P. S. Calefi, K. J. Ciuffi, E. J. Nassar, J. V. L. Silva, M. Oliveira, I. I. Maia, Ultraviolet sensors using a luminescent europium (III) complex on acrylonitrile butadiene styrene Polymer, *Journal of Materials Research*, 27 (2012), 2088–2095, <https://doi.org/jmr.2012.129>.
- [126] P. P. Ortega, L. S. R. Rocha, J. A. Cortés, M. A. Ramirez, C. Buono, M. A. Ponce, A. Z. Simões, Towards carbon monoxide sensors based on europium doped cerium dioxide, *Appl. Surf. Sci.*, 464 (2019), pp. 692-699, <https://doi.org/10.1016/j.apsusc.2018.09.142>.
- [127] B. Liu, Y. Huang, X. Zhu, Y. Hao, Y. Ding, W. Wei, Q. Wang, P. Qu, M. Xu, Smart lanthanide coordination polymer fluorescence probe for mercury(II) determination, *Analytica Chimica Acta*, 912 (2016) 139-145, <http://doi.org/10.1016/j.aca.2016.01.044>.
- [128] H. Tan, Y. Zhang, Y. Chen, Detection of mercury ions (Hg²⁺) in urine using a terbium chelate fluorescent probe, *Sensors and Actuators B*, 156 (2011) 120–125, <http://doi.org/10.1016/j.snb.2011.03.081>.

- [129] G. Cui, Z. Ye, R. Zhang, G. Wang, J. Yuan, Design and Synthesis of a Terbium(III) Complex-Based Luminescence Probe for Time-Gated Luminescence Detection of Mercury(II) Ions, *Journal of fluorescence*, 22 (2011) 261-267, <http://doi.org/10.1007/s10895-011-0956-6>.
- [130] Hongliang Tan, Qian Li, Chanjiao Ma, Yonghai Song, Fugang Xu, Shouhui Chen, Li Wang. Lanthanide based dual-emission fluorescent probe for detection of mercury (II) in milk, *Biosensors and Bioelectronics*, 63 (2015) 566-571, <https://doi.org/10.1016/j.bios.2014.08.015>.
- [131] M. Yang, C. Zhou, Y. Chen, J. Li, C. Zeng, S. Zhong. Highly sensitive and selective sensing of CH_3Hg^+ via oscillation effect in Eu-cluster, *Sensors and Actuators B*, 248 (2017) 589–596, <http://doi.org/10.1016/j.snb.2017.03.131>.
- [132] F. Zhao, X.-Z. Wang, S.-T. He, P.-Z. Ma, W. Zhang, Y.-C. Ma, S.-J. Zhao, J. Sun. Highly sensitive bifunctional sensor of a dinuclear terbium complex, *Sensors and Actuators B: Chemical* 270 (2018) 452-458, <https://doi.org/10.1016/j.snb.2018.05.073>.
- [133] Y. Liu, M. Chen, T. Cao, Y. Sun, C. Li, Q. Liu, T. Yang, L. Yao, W. Feng, F. Li. A Cyanine-Modified Nanosystem for in Vivo Upconversion Luminescence Bioimaging of Methylmercury, *J. Am. Chem. Soc.*, 135 (2013) 9869–9876, <https://doi.org/10.1021/ja403798m>.
- [134] H. Wang, X. Wang, M. Liang, G. Chen, R.-M Kong, L. Xia, F. Qu. A Boric Acid-Functionalized Lanthanide Metal–Organic Framework as a Fluorescence “Turn-on” Probe for Selective Monitoring of Hg^{2+} and CH_3Hg^+ , *Anal. Chem.*, 92 (2020) 3366–3372, <https://doi.org/10.1021/acs.analchem.9b05410>.
- [135] Agency for Toxic Substances and Disease Registry. Toxicological Profile for Formaldehyde. Agency for Toxic Substances and Disease Registry, US Department of Health and Human Services, 1999.
- [136] M. Naya, J. Nakanish, Risk assessment of formaldehyde for the general population in Japan, *Regul. Toxicol. Pharmacol.*, 43 (2005) 232–248, <http://doi.org/10.1016/j.yrtph.2005.08.002>.
- [137] R. Dales, M. Raizenne, Residential exposure to volatile organic compounds and asthma, *J. Asthma.*, 41 (2004) 259–270, <http://doi.org/10.1081/JAS-120026082>.
- [138] J. H. E. Arts, M. A. J. Rennen, C. De-Heer, Inhaled formaldehyde: Evaluation of sensory irritation in relation to carcinogenicity, *Regul. Toxicol. Pharm.*, 44 (2006) 144–160, <http://doi.org/10.1016/j.yrtph.2005.11.006>.
- [139] A. Casset, C. Marchand, A. Purohit, S. Le-Calve, B. Uring-Lambert, C. Donnay, Inhaled formaldehyde exposure: Effect on bronchial response to mite allergen in sensitized asthma patients, *Allergy.*, 61 (2006) 1344–1350, <http://doi.org/10.1111/j.1398-9995.2006.01174.x>.
- [140] C. F. Nascimento, M. A. S. Brasil, S. P. F. Costa, P. C. A. G. Pinto, M. L. M. F. S. Saraiva, F. R. P. Rocha, Exploitation of pulsed flows for on-line dispersive liquid–liquid microextraction: spectrophotometric determination

of formaldehyde in milk, *Talanta*, 144 (2015) 1189–1194, <http://doi.org/10.1016/j.talanta.2015.07.076>.

[141] X. Xu, R. Su, X. Zhao, Z. Liu, D. Li, X. Li, H. Zhang, Z. Wang, Determination of formaldehyde in beverages using microwave-assisted derivatization and ionic liquid-based dispersive liquid–liquid microextraction followed by high-performance liquid chromatography, *Talanta*, 85 (2011) 2632–2638, <https://doi.org/10.1016/j.talanta.2011.08.037>.

[142] Brasil. Ministério da Agricultura, Pecuária e Abastecimento. Manual de métodos oficiais para análise de alimentos de origem animal / Ministério da Agricultura, Pecuária e Abastecimento. Secretaria de Defesa Agropecuária. – 2. ed. – Brasília: MAPA, 2019.

[143] AOAC International. Official Methods of Analysis of AOAC International, Official Method 931.08. 21 ed. Rockville: 2019.

[144] F. B. de F. Rezende, A. M. de S. S. Cheibub, A. D. P. Netto, F. F. de C. Marques, Determination of formaldehyde in bovine milk using a high sensitivity HPLC-UV method, *Microchemical Journal*, 134 (2017) 383–389, <https://doi.org/10.1016/j.microc.2017.07.003>.

[145] M. S. Hossain, M. S. Islam, S. Bhadra, A. S. S. Rouf, Investigation of Formaldehyde Content in Dairy Products Available in Bangladesh by a Validated High Performance Liquid Chromatographic Method, *Dhaka Univ. J. Pharm. Sci.*, 15 (2016) 187-194, <https://doi.org/10.3329/dujps.v15i2.30936>.

[146] A. S. Sebaei, A. M. Gomaa, A. A. El-Zwahry, E. A. Emara, Determination of Formaldehyde by HPLC with Stable Pre-column Derivatization in Egyptian Dairy Products, *Int. J. Anal. Chem.*, 2018 (2018) 2757941, <https://doi.org/10.1155/2018/2757941>.

[147] H.-S. Jeong, H. Chung, S.-H. Song, C.-I. Kim, J.-G. Lee, Y.-S. Kim, Validation and determination of the contents of acetaldehyde and formaldehyde in foods, *Toxicol. Res.*, 31 (2015) 273-278, <https://doi.org/10.5487%2FTR.2015.31.3.273>.

[148] J. F. Cerdán, M. Peris-Tortajada, R. Puchades, Automation of the determination of hydrogen peroxide, dichromate, formaldehyde and bicarbonate in milk by flow injection analysis, *Fresenius J. Anal. Chem.*, 344 (1992) 123-127, <https://doi.org/10.1007/BF00325127>.

[149] F. Xin, Y. Tian, J. Jing, X. Zhang, A two-photon fluorescent probe for imaging of endogenous formaldehyde in HeLa cells and quantitative detection of basal formaldehyde in milk samples, *Anal. Methods*, 11 (2019) 2969, <https://doi.org/10.1039/C9AY00553F>.

[150] L. Bueno, W. R. De Araujo, M. O. Salles, M. Y. Kussuda, T. R. L. C. Paixão, Voltammetric Electronic Tongue for Discrimination of Milk Adulterated with Urea, Formaldehyde and Melamine, *Chemosensors*, 2 (2014) 251-266, <https://doi.org/10.3390/chemosensors2040251>.

[151] H. Xi, X. Chen, Y. Cao, J. Xu, C. Ye, D. Deng, J. Zhang, G. Huang, Electrochemical determination of formaldehyde via reduced AuNPs@PPy

composites modified electrode, *Microchemical Journal*, 156 (2020) 104846, <https://doi.org/10.1016/j.microc.2020.104846>.

[152] C.S. Gondim, R. G. Junqueira, S. V. C. de Souza, I. Ruisánchez, M. P. Callao, Detection of several common adulterants in raw milk by MID-infrared spectroscopy and one-class and multi-class multivariate strategies, *Food Chemistry*, 230 (2017) 68–75, <https://doi.org/10.1016/j.foodchem.2017.03.022>.

[153] T. B. Coitinho, L. D. Cassoli, P. H. R. Cerqueira, H. K. da Silva, J. B. Coitinho, P. F. Machado, Adulteration identification in raw milk using Fourier transform infrared spectroscopy, *J. Food Sci. Technol.*, 54 (2017) 2394–2402, <https://doi.org/10.1007/s13197-017-2680-y>.

[154] M. I. Alkhalif, M. E. S. Mirghani, Detection of formaldehyde in cheese using FTIR spectroscopy, *International Food Research Journal*, 24 (2017) S496-S500.

[155] F. Mabood, J. Hussain, Al Nabhani MOO, S. A. Gilani, S. Farooq, Z. Naureen, F. Jabeen, M. Ahmed, Z. Hussain, A. Al-Harrasi, Detection and Quantification of Formalin Adulteration in Cow Milk Using Near Infrared Spectroscopy Combined with Multivariate Analysis, *J. Adv. Dairy. Res.*, 5 (2017) 167, <https://doi.org/10.4172/2329-888X.1000167>.

[156] P. T. Coimbra, C. F. Bathazar, J. T. Guimarães, N. M. Coutinho, T. C. Pimentel, R. P. C. Neto, E. A. Esmerino, M. Q. Freitas, M. C. Silva, M. I. B. Tavares, A. G. Cruz, Detection of formaldehyde in raw milk by time domain nuclear magnetic resonance and chemometrics, *Food Control*, 110 (2020) 107006, <https://doi.org/10.1016/j.foodcont.2019.107006>.

[157] G. Durante, W. Becari, F. A. S. Lima, H. E. M. Peres, Electrical Impedance Sensor for Real-Time Detection of Bovine Milk Adulteration, *Sensors Journal*, 16 (2016) 861-865, <https://doi.org/10.1109/JSEN.2015.2494624>.

[158] C. Martínez-Aquino, A. M. Costero, S. Gil, P. Gaviña, A New Environmentally-Friendly Colorimetric Probe for Formaldehyde Gas Detection under Real Conditions, *Molecules*, 23 (2018) 2646, <https://doi.org/10.3390/molecules23102646>.

[159] P. Li, D. Zhang, Y. Zhang, W. Lu, W. Wang, T. Chen, Ultrafast and Efficient Detection of Formaldehyde in Aqueous Solutions Using Chitosan-based Fluorescent Polymers. *ACS Sens.*, 3 (2018) 2394–2401, <https://doi.org/10.1021/acssensors.8b00835>.

[160] H. Ding, G. Yuan, L. Peng, L. Zhou, Q. Lin, TP-FRET-Based Fluorescent Sensor for Ratiometric Detection of Formaldehyde in Real Food Samples, Living Cells, Tissues, and Zebrafish, *J. Agric. Food Chem.*, 68 (2020) 3670–3677, <https://doi.org/10.1021/acs.jafc.9b08114>.

[161] M. I. S. Veríssimo, J. A. F. Gamelas, A. J. S. Fernandes, D. V. Evtuguin, M. T. S. R. Gomes, A new formaldehyde optical sensor: Detecting milk adulteration, *Food Chemistry*, 318 (2020) 126461, <https://doi.org/10.1016/j.foodchem.2020.126461>.

- [162] Y. Zhang, X. Su, Q. J. Ma, Novel Formaldehyde Sensor based on Hydrogen Peroxide/Melamine Modulated Photoluminescence of Nitrogen-doped Graphene Quantum Dots, *Wuhan Univ. Technol.-Mat. Sci. Edit.*, 32 (2017) 1481, <https://doi.org/10.1007/s11595-017-1772-x>.
- [163] H.-J. Li, X. Sun, F. Xue, N. Ou, B.-W. Sun, D.-J. Qian, M. Chen, D. Wang, J. Yang, X. Wang, Redox Induced Fluorescence On–Off Switching Based on Nitrogen Enriched Graphene Quantum Dots for Formaldehyde Detection and Bioimaging, *ACS Sustainable Chemistry & Engineering*, 6 (2018) 1708-1716, <https://doi.org/10.1021/acssuschemeng.7b02941>.
- [164] Y. Zhang, J. Qi, M. Li, D. Gao, C. Xing, Fluorescence Probe Based on Graphene Quantum Dots for Selective, Sensitive and Visualized Detection of Formaldehyde in Food, *Sustainability*, 13 (2021) 5273, <https://doi.org/10.3390/su13095273>.
- [165] Oxidation of Aldehydes and Ketones, <https://chem.libretexts.org/@go/page/3919> (accessed Feb 26, 2022).
- [166] X.-D. Wang, O. S. Wolfbeis, R. J. Meier, Luminescent probes and sensors for temperature, *Chem. Soc. Rev.*, 42 (2013) 7834-7869, <https://doi.org/10.1039/C3CS60102A>.
- [167] P. R. N. Childs, J. R. Greenwood, C. A. Long, Review of temperature measurement, *Review of Scientific Instruments*, 71 (2000) 2959, <http://doi.org/10.1063/1.1305516>.
- [168] M. McSherry, C. Fitzpatrick, E. Lewis, Review of luminescent based fibre optic temperature sensors, *Sensor Review*, 25 (2005) 56-62, <https://doi.org/10.1108/02602280510577852>.
- [169] M. N. Getz, O. Nilsen, P.-A. Hansen, sensors for optical thermometry based on luminescence from layered YVO₄: Ln³⁺ (Ln = Nd, Sm, Eu, Dy, Ho, Er, Tm, Yb) thin films made by atomic layer deposition, *Sci. Rep.*, 9 (2019) 10247, <https://doi.org/10.1038/s41598-019-46694-8>.
- [170] M. Runowski, P. Wozny, N. Stopikowska, I. R. Martín, V. Lavín, S. Lis, Luminescent Nanothermometer Operating at Very High Temperature-Sensing up to 1000 K with Upconverting Nanoparticles (Yb³⁺/Tm₃₊), *ACS Appl. Mater. Interfaces*, 12 (2020) 43933–43941, <https://doi.org/10.1021/acscami.0c13011>.
- [171] L. B. Guimarães, A. M. P. Botas, M. C. F. C. Felinto, R. A. S. Ferreira, L. D. Carlos, O. L. Malta, H. F. Brito, Highly sensitive and precise optical temperature sensors based on new luminescent Tb³⁺/Eu³⁺ tetrakis complexes with imidazolic counterions, *Mater. Adv.*, 1 (2020) 1988, <https://doi.org/10.1039/d0ma00201a>.
- [172] C. J. Salas-Juárez, R.E. Navarro, A. Pérez-Rodríguez, U. Orozco-Valencia, R. Aceves, Visual temperature sensor and luminescent thermometer based on the complex Tb/Eu–TPTZ incorporated in transparent PMMA film, *Sensors and Actuators A: Physical*, 315 (2020) 112293, <https://doi.org/10.1016/j.sna.2020.112293>.
- [173] C. H. Park, H. Yang, J. Lee, H.-H. Cho, D. Kim, D. C. Lee, B. J. Kim, Multicolor Emitting Block Copolymer-Integrated Graphene Quantum Dots

for Colorimetric, Simultaneous Sensing of Temperature, pH, and Metal Ions, *Chem. Mater.*, 27 (2015) 5288–5294, <https://doi.org/10.1021/acs.chemmater.5b01545>.

[174] M. K. Kumawat, M. Thakur, R. B. Gurung, R. Srivastava, Graphene Quantum Dots from *Mangifera indica*: Application in Near Infrared Bioimaging and Intracellular Nanothermometry, *ACS Sustainable Chem. Eng.*, 5 (2017) 1382–1391, <https://doi.org/10.1021/acssuschemeng.6b01893>.

[175] D. K. Nguyen, T. Y. Kim, Graphene quantum dots produced by exfoliation of intercalated graphite nanoparticles and their application for temperature sensors, *Applied Surface Science*, 427 (2018) 1152–1157, <https://doi.org/10.1016/j.apsusc.2017.09.020>.

[176] T. Gao, X. Wang, J. Zhao, P. Jiang, F.-L. Jiang, Y. Liu, Bridge between Temperature and Light: Bottom-Up Synthetic Route to Structure-Defined Graphene Quantum Dots as a Temperature Probe In Vitro and in Cells, *ACS Appl. Mater. Interfaces*, 12 (2020) 22002–22011, <https://doi.org/10.1021/acsami.0c02500>.

[177] B.H. Lee, R.L. McKinney, M.T. Hasan, A.V. Naumov, Graphene Quantum Dots as Intracellular Imaging-Based Temperature Sensors, *Materials*, 14 (2021) 616, <https://doi.org/10.3390/ma14030616>.

[178] S. Uchiyama, K. Kimura, C. Gota, K. Okabe, K. Kawamoto, N. Inada, T. Yoshihara, S. Tobita, Environment-Sensitive Fluorophores with Benzothiadiazole and Benzoselenadiazole Structures as Candidate Components of a Fluorescent Polymeric Thermometer, *Chem. Eur. J.*, 18 (2012) 9552 – 9563, <https://doi.org/10.1002/chem.201200597>.

[179] M. Echeverri, C. Ruiz, S. Gamez-Valenzuela, M. Alonso-Navarro, E. Gutierrez-Puebla, J. L. Serrano, M. C. R. Delgado, B. Gomez-Lor, Stimuli-Responsive Benzothiadiazole Derivative as a Dopant for Rewritable Polymer Blends, *ACS Appl. Mater. Interfaces*, 12 (2020) 10929–10937, <https://doi.org/10.1021/acsami.9b21209>.

[180] D. Zhao, D. Yue, K. Jiang, Y. Cui, Q. Zhang, Y. Yang, G. Qian, Ratiometric dual-emitting MOF dye thermometers with a tunable operating range and sensitivity, *J. Mater. Chem. C*, 5 (2017) 1607, <https://doi.org/10.1039/C6TC05203G>.

[181] M. A. Guedes, Comportamento fotoluminescente dos ânions complexos tetrakis(-dicetonatos) de Íons terras raras - Eu^{3+} , Gd^{3+} , Tb^{3+} e Tm^{3+} [tese]. São Paulo, Instituto de Química, 2007.

[182] K. Chiba, K. Yoshida, K. Tanabe, H. Haraguchi. Determination of Alkylmercury in Seawater at the Nanogram per Liter Level by Gas Chromatography/Atmospheric Pressure Helium Microwave-Induced Plasma Emission Spectrometry, *Anal. Chem.* (1983) 450–453. <https://doi.org/10.1021/ac00254a010>.

[183] C. A. T. Toloza, Spectroanalytical methods using graphene quantum dots as photoluminescent probes for the determination of analytes of biological and pharmacological interest. Rio de Janeiro, 2018. 158p. Tese

de doutorado – Departamento de Química, Pontifícia Universidade Católica do Rio de Janeiro.

[184] C. Würth, M. Grabolle, J. Pauli, M. Spieli, U. Resch-Genger, Relative and absolute determination of fluorescence quantum yields of transparent samples, *Nat Protoc.*, 8 (2013) 1535–1550, <https://doi.org/10.1038/nprot.2013.087>.

[185] S. Dhimi, A. J. De Mello, G. Rumbles, S. M. Bishop, D. Phillips, A. Beeby, Phthalocyanine fluorescence at high concentration: dimers or reabsorption effect?, *Photochemistry & Photobiology*, 61 (1995) 341-346, <https://doi.org/10.1111/j.1751-1097.1995.tb08619.x>.

[186] W. H. Melhuish, Quantum efficiencies of fluorescence of organic substances: effect of solvent and concentration of the fluorescent solute, *J. Phys. Chem.*, 65 (1961) 229–235, <https://doi.org/10.1021/j100820a009>.

[187] I. Costas-Mora, V. Romero, F. Pena-Pereira, I. Lavilla, C. Bendicho, Quantum dot-based headspace single-drop microextraction technique for optical sensing of volatile species, *Anal. Chem.*, 83 (2011) 2388–2393, <https://doi.org/10.1021/ac103223e>.

[188] I. Costas-Mora, V. Romero, F. Pena-Pereira, I. Lavilla, C. Bendicho, Quantum dots confined in an organic drop as luminescent probes for detection of selenium by microfluorospectrometry after hydridation: study of the quenching mechanism and analytical performance, *Anal. Chem.*, 84 (2012) 4452–4459, <https://doi.org/10.1021/ac300221s>.

[189] INSTRUÇÃO NORMATIVA Nº 62, DE 29 DE DEZEMBRO DE 2011.

[190] N. M. Shavaleev, S. J. A. Pope, Z. R. Bell, S. Faulkner, M. D. Ward, Visible-light sensitisation of near-infrared luminescence from Yb(III), Nd(III) and Er(III) complexes of 3,6-bis(2-pyridyl)tetrazine, *Dalton Trans.*, (2003) 808–814, <https://doi.org/10.1039/B300294B>.

[191] A. Pramanik, S. Biswas, C. S. Tiwary, R. Sarkar, P. Kumbhakar, Colloidal N-doped graphene quantum dots with tailored luminescent downshifting and detection of UVA radiation with enhanced responsivity, *ACS Omega*, 3 (2018) 16260–16270, <https://doi.org/10.1021/acsomega.8b02473>.

[192] D. Tan, S. Zhou, Y. Shimotsuma, K. Miura, J. Qiu, Effect of UV irradiation on photoluminescence of carbon dots, *Opt. Mater. Express*, 4 (2014) 213-219, <https://doi.org/10.1364/OME.4.000213>.

[193] M. K. Rabchinskii, S. D. Saveliev, D. Y. Stolyarova, M. Brzhezinskaya, D. A. Kirilenko, M. V. Baidakova, S. A. Ryzhkov, V. V. Shnitov, V. V. Sysoev, P. N. Brunkov, Modulating nitrogen species via N-doping and post annealing of graphene derivatives: XPS and XAS examination, *Carbon*, 182 (2021) 593-604, <https://doi.org/10.1016/j.carbon.2021.06.057>.

[194] H. Tetsuka, A. Nagoya, T. Fukusumi, T. Matsui, Molecularly designed, nitrogen-functionalized graphene quantum dots for optoelectronic devices, *Adv. Mater.*, 28 (2016) 4632-4638, <https://doi.org/10.1002/adma.201600058>.

- [195] M. T. Hasan, R. Gonzales-Rodriguez, C. Ryan, K. Pota, K. Green, J. L. Coffey, A. V. Naumov, Nitrogen-doped graphene quantum dots: Optical properties modification and photovoltaic applications, *Nano Res.*, 12 (2019) 1041-1047, <https://doi.org/10.1007/s12274-019-2337-4>.
- [196] A. Amari, N. Elboughdiri, D. Ghernaout, R. H. Lajimi, A. M. Alshahrani, M. A. Tagoon, F. B. Rebah, Multifunctional crosslinked chitosan/nitrogen-doped graphene quantum dot for wastewater treatment, *Ain Shams Engineering Journal*, 12 (2021) 4007-4014, <https://doi.org/10.1016/j.asej.2021.02.024>.
- [197] R. M. Fiuza, C. Vesga-Hernández, J. Padilha, L. Maqueira, R. Q. Aucélio, J. Limberger, A styryl-benzothiadiazole derivative with aggregation-induced enhanced emission for latent fingerprint recognition, *Journal of Luminescence*, (2022) 118920, <https://doi.org/10.1016/j.jlumin.2022.118920>.
- [198] P. P. Lima, M. M. Nolasco, F. A. A. Paz, R. A. S. Ferreira, R. L. Longo, O. L. Malta, L. D. Carlos, Photo-Click Chemistry to Design Highly Efficient Lanthanide β -Diketonate Complexes Stable under UV Irradiation, *Chem. Mater.*, 25 (2013) 586–598, <https://doi.org/10.1021/cm303776x>.
- [199] D. W. Setser, D. W. Placzek, R. J. Cvetanović, B. S. Rabinovitch. Some Examples of the Use of Oxygen as a Diagnostic Test for the Triplet State in Chemical Reactions, *Canadian Journal of Chemistry*, 40 (1962) 2179-2184, <https://doi.org/10.1139/v62-336>.
- [200] O. L. J. Gijzeman, F. Kaufman, Oxygen quenching of aromatic triplet states in solution. Part 2, *J. Chem. Soc., Faraday Trans. 2*, 69 (1973) 721-726, <https://doi.org/10.1039/F29736900721>.
- [201] F. Wilkinson, D. J. McGarvey, A. F. Olea, Excited Triplet State Interactions with Molecular Oxygen: Influence of Charge Transfer on the Bimolecular Quenching Rate Constants and the Yields of Singlet Oxygen [$O^*(1.\Delta.g)$] for Substituted Naphthalenes in Various Solvents, *J. Phys. Chem.*, 98 (1994) 3762-3769, <https://doi.org/10.1021/j100065a035>.
- [202] J. F. Hung, W. Y. Quiong, Determination of Fluoroquinolones in Eggs Using In-Tube Solid-Phase Microextraction Coupled to High-Performance Liquid Chromatography, *Analytical Bioanalytical Chemistry*, 384 (2006) 1228–1235, <http://doi.org/10.1007/s00216-005-0270-8>.
- [203] T. Vo-Dinh, Room temperature phosphorescence for chemical analysis. *Chemical Analysis Series*, 68, New York: Wiley, 1984.
- [204] R. Hurtubise, *Phosphorimetry: Theory, Instrumentation, and Applications*. Nova Iorque: VCH Publishers, 1990.
- [205] R. G. Pearson, Hard and soft acids and bases, *Journal of the American Chemical Society*, 85 (1963) 3533-3539, <http://doi.org/10.1021/ja00905a001co>.
- [206] BRASIL. Ministério do Meio Ambiente. Resolução CONAMA nº 357, de 15 de junho de 2005.
- [207] Y.-K. Yang, K.-J. Yook, J. Tae, A rhodamine-based fluorescent and colorimetric chemodosimeter for the rapid detection of Hg^{2+} ions in aqueous

media, J. Am. Chem. Soc., 127 (2005) 16760-16761, <https://doi.org/10.1021/ja054855t>.

[208] N. L. Fish, P. J. Pinkston, T.J. Claydon, R. Mickelsen, Effect of Hydrogen Peroxide Treatment of Milk on Its Proteolysis by *Pseudomonas fluorescens* 1, 2, Journal of Dairy Science, 52 (1969) 619-624, [https://doi.org/10.3168/jds.S0022-0302\(69\)86617-8](https://doi.org/10.3168/jds.S0022-0302(69)86617-8).

[209] S. Arefin, M. A. H. Sarker, M. A. Islam, M. Harun-ur-Rashid, M. N. Islam, Use of Hydrogen Peroxide (H₂O₂) in raw cow's milk preservation, Journal of Advanced Veterinary and Animal Research, 4 (2018) 371–377, <https://doi.org/10.5455/javar.2017.d236>.

[210] B. K. Saha, M. Y. Ali, M. Chakraborty, Z. Islam, A. K. Hira, Study on the preservation of raw milk with hydrogen peroxide (H₂O₂) for rural dairy farmers, Pakistan Journal of Nutrition, 2 (2003) 36-42, <https://doi.org/10.3923/pjn.2003.36.42>.

10 Attachments

10.1. Published papers

Talanta 244 (2022) 123406



Use of selective quenching of a photoluminescent probe based on a Eu(III) β -diketonate complex for determination of methylmercury in produced water after liquid-liquid extraction



Juliana da S. Padilha, Marcelo F.M.F. Azevedo, Jarol R. Miranda-Andrades, Anna De Falco, Jiang Kai, Ricardo Q. Aucelio*

Department of Chemistry, Pontifical Catholic University of Rio de Janeiro (PUC-Rio), Rio de Janeiro, Brazil

Graphical abstract

